

# Prototype Developments and Performance Studies for the CBM-TRD

Dissertation  
zur Erlangung des Doktorgrades  
der Naturwissenschaften

vorgelegt beim Fachbereich Physik  
der Johann Wolfgang Goethe -Universität  
in Frankfurt am Main

von  
**Milad Tanha**  
aus Iran

Frankfurt 2017  
(D 30)

vom Fachbereich Physik der Johann Wolfgang Goethe - Universität  
als Dissertation angenommen.

**Dekan:**

Prof. Dr. Owe Philipsen

**Gutachter:**

Prof. Dr. Christoph Blume

PD Dr. Anton Andronic

**Datum der Disputation:**

14.07.2017



## Abstract

The fundamental structure of matter is the subject of the Standard Model of Elementary Particles. It is based on the assumption that everything in the universe is made of a few basic building blocks called elementary particles, governed by four fundamental forces. Quarks and leptons are the building blocks of matter. The four fundamental forces are the electromagnetic, strong, weak and gravitational force<sup>1</sup>. The strong force is responsible for binding the constituents of a nucleus, generating complex matter structures and phases at the subatomic level. The fundamental theory of the strong interaction is Quantum Chromodynamics (QCD), which describes the interactions between quarks and gluons that generate hadrons such as protons, neutrons and pions. At high temperatures and/or densities of nuclear matter, QCD predicts a phase transition from hadronic matter (confined quark matter) into a hot and dense Quark-Gluon Plasma (QGP) (deconfined quarks and gluons). The QCD phase diagram indicates phases of nuclear matter at very high-temperature conditions as in the early universe just after the big bang, as well as high matter density conditions, which can be found in very compact stars. Investigating the QCD phase diagram is the major goal of several heavy-ion experiments.

The Compressed Baryonic Matter (CBM) experiment as part of the Facility for Antiproton and Ion Research (FAIR) at the Helmholtz Centre for Heavy-Ion Research (German acronym: GSI) will explore the QCD phase diagram in the region of high baryon densities using high-energy nucleus-nucleus collisions.

The physics observables for the CBM experiment are including (but not limited to) hadrons, multi-strange hyperons, low-mass vector mesons ( $\omega$ ,  $\rho$ ,  $\phi$ ), open charm particles ( $D^0$ ,  $D^\pm$ ,  $\Lambda_c$ ) and charmonia ( $J/\psi$ ,  $\psi'$ ).

The study of intermediate mass dileptons (mass range between  $m(\phi)$  and  $m(J/\psi)$ ) and quarkonia ( $J/\psi$ ) cannot be performed in the CBM experiment without a transition radiation detector. The Transition Radiation Detector (TRD) in the CBM experiment is based on Multi-Wire Proportional Chambers (MWPC) including a radiator to produce transition radiation photons. The gas volume of the MWPC includes the drift region, the anode wire plane and the amplification

---

<sup>1</sup>The gravitational force is not included in the standard model of elementary particles.

region. The back panel contains the pad plane where the cluster charges can be detected by electronics.

To reach the goals of the CBM experiment, several different TRD prototypes have been developed at the Institut für Kernphysik in Frankfurt (IKF), and experimental results from laboratory test and test-beams at CERN, as well as simulation results, are discussed.

Results from the test-beam at the CERN-PS in 2014 showed that the small-size TRD prototype with a thin symmetrical amplification region ( $3.5+3.5$  mm), alternating anode-cathode wire plane (sense and field wires on a plane) and without drift region is fast enough in terms of signal collection time (signal collection times below  $0.1 \mu\text{s}$  were achieved) and might be an optional choice for the inner parts of the TRD layers at high-rate beam experiments, e.g. at the FAIR-SIS300 energy range.

Results from the test-beam at the CERN-SPS in 2015 showed that the full-size TRD prototype with an amplification region of  $4+4$  mm, alternating wire plane and without drift region is stable at moderate hit rates ( $\sim 10^3 \text{ Hz/cm}^2$ ).

Laboratory and test-beam experiments helped us to investigate the readout and electronics for the TRD and to understand the requirements and necessary criteria for the readout chain for the TRD.

According to the design parameters of the TRD (electron identification and pion suppression factor of 10-20 at 90% electron efficiency) and several years of experimental and simulation results, a design of the full-size TRD prototype for the CBM experiment at SIS100 was finalized and a prototype has been developed and tested at the CERN-SPS in 2016. The prototype has  $3.5+3.5$  mm amplification region, 5 mm drift region and includes a normal anode-cathode wire geometry.

This work explains the development of the different detector prototypes since 2012 until 2016. The characteristics of two TRD prototypes, as well as simulation results, with an emphasis on the setup of the front-end board (Self-triggered Pulse Amplification and Digitization asIC (SPADIC)) are discussed.

# Contents

<b>1</b>	<b>Introduction</b>	<b>5</b>
<b>2</b>	<b>Physics Motivation</b>	<b>7</b>
2.1	The Standard Model of Particle Physics . . . . .	7
2.2	Physics of the Compressed Baryonic Matter Experiment . . . . .	10
2.2.1	The Phase Diagram of QCD . . . . .	11
2.2.2	Observables of the CBM Experiment . . . . .	15
<b>3</b>	<b>Facility for Anti-proton and Ion Research</b>	<b>20</b>
<b>4</b>	<b>The Compressed Baryonic Matter Experiment</b>	<b>23</b>
4.1	Superconducting Dipole Magnet . . . . .	25
4.2	Detector Systems . . . . .	27
<b>5</b>	<b>Transition Radiation Detector</b>	<b>35</b>
5.1	Gamma- and X-ray Interaction in Matter . . . . .	35
	Photoelectric Effect . . . . .	36
	Compton Effect . . . . .	38

Pair Production . . . . .	39
Rayleigh (coherent) scattering . . . . .	40
Photo-nuclear Interaction . . . . .	40
5.2 Interaction of Charged Particles with Matter . . . . .	41
5.3 Multi-Wire Proportional Chamber . . . . .	45
5.3.1 Prototype Characteristics . . . . .	47
Gas Gain . . . . .	47
Energy Resolution . . . . .	48
Pad Response Function . . . . .	49
Track Position . . . . .	52
Cluster Reconstruction . . . . .	52
Position Resolution . . . . .	53
Particle Identification . . . . .	53
5.4 Principle of Operation of a TRD . . . . .	57
5.5 Choice of Gas for the TRD . . . . .	58
5.6 Radiator . . . . .	59
5.7 Readout Chamber Design . . . . .	61
<b>6 Prototype Design and Construction</b>	<b>71</b>
6.1 Prototype Development in Bucharest . . . . .	71
6.2 Prototype Development in Münster . . . . .	72
6.3 Prototype Development in Frankfurt . . . . .	73
6.3.1 Fast ROC design . . . . .	73

6.3.2	Fast Prototype with Alternating Wire Configuration . . . . .	75
	Laboratory Setup and Energy Resolution . . . . .	78
	Simulations for the Fast ROCs at IKF . . . . .	82
6.4	Pad Planes for the TRD at SIS100 . . . . .	89
<b>7</b>	<b>Readout Electronics</b>	<b>93</b>
7.1	SPADIC . . . . .	93
7.1.1	Data Flow Through the SPADIC Chip v.1.0 . . . . .	96
7.1.2	The Detection of Hit and Trigger Concept . . . . .	96
7.1.3	Structure, Configuration and Recorded Data . . . . .	100
7.1.4	Issues with the SPADIC v1.0 and Improvements in Newer Versions . . . . .	103
7.2	SysCore v3.1 . . . . .	107
7.3	FLIB . . . . .	109
<b>8</b>	<b>Test-Beam Campaigns</b>	<b>111</b>
8.1	The Test-Beam Campaign in 2014 . . . . .	111
8.2	The Test-Beam Campaign in 2015 . . . . .	116
<b>9</b>	<b>Performance Studies</b>	<b>120</b>
9.1	SPADIC Data Analysis . . . . .	120
9.2	Performance Studies with the Test-Beam at the CERN-PS in 2014 .	122
9.2.1	Pad Response Function . . . . .	122
9.3	Performance Studies with the Test-Beam at CERN-SPS in 2015 . .	127
9.3.1	Current Measurements . . . . .	127

<b>10 Further Developments</b>	<b>132</b>
<b>Summary</b>	<b>135</b>
<b>Apendix A</b>	<b>144</b>
<b>Apendix B</b>	<b>147</b>
<b>Bibliography</b>	<b>161</b>

# Chapter 1

## Introduction

The discovery of galactic red shifts and the analysis of the cosmic background radiation were the empirical evidences for the expansion of the universe and led to a cosmological model, which considers a singularity at the beginning of the universe, known as the Big Bang. The model accounts for the fact that the universe passed through a very high density and high-temperature state called Quark-Gluon Plasma (QGP), where the quarks and gluons are not confined in hadrons. This state is a property of Quantum Chromo Dynamics (QCD).

The study of the QCD phase diagram as a model for the states of the early universe helps us to answer some fundamental, fascinating and crucial questions such as: How did the universe evolve and why does it look the way it does today? How does matter behave across the wide range of temperatures and pressures found in the past and present universe? How does the strong force work, which binds the particles comprising atomic nuclei, and where do their masses come from? Where do the atomic elements come from?

Concerning this, high energy heavy-ion collision experiments at the CERN Super Proton Synchrotron (SPS) with a beam energy of 10 to 160 A GeV, the Large Hadron Collider (LHC), which collides Pb ions at  $\sqrt{s_{NN}} = 2.76$  TeV and  $\sqrt{s_{NN}} = 5.02$  TeV, and the Relativistic Heavy Ion Collider (RHIC) at Brookhaven National Laboratory with top center-of-mass energy of  $\sqrt{s_{NN}} = 200$  GeV are dedicated to probe the transition from hadronic matter to a hot and dense state of matter (QGP) at high temperatures and small baryon density. Among these laboratories, the Facility for Antiproton and Ion Research (FAIR) in Darmstadt, Germany, where various physics programs can be operated in parallel, is under construction. The Compressed Baryonic Matter (CBM) experiment is part of the

physics programs at the FAIR complex.

The CBM experiment, a fixed target experiment, is part of the FAIR complex where the different ion species will be accelerated to beam energies between 10 and 45A GeV to explore the QCD phase diagram in the region of highest net baryon densities. Among existing heavy-ion experiments, the CBM experiment has the highest rate collision, which will offer the opportunity to study nuclear collisions at unprecedented interaction rates. The rate capabilities of existing and planned heavy-ion experiments are presented in Fig. 1.1 as a function of center-of-mass energy. The location of the first-order phase transition from partonic to hadronic matter, the position of its critical end point, and the modifications of hadron properties in the dense medium as a signal of chiral symmetry restoration are of particular interest. To reach the aim of the CBM experiment, the development of novel detector systems, trigger and data-acquisition concepts, as well as innovative real-time reconstruction techniques are required [1].

A major part of the electron identification in CBM experiment will be performed by the Transition Radiation Detector (TRD), which is designed to discriminate between electron and pion tracks with a rejection factor greater than 10 for a 90% electron efficiency at the SIS100 applying four layers of TRDs. At the SIS300, pion suppression of about 100 at 90% electron efficiency is expected by applying ten layers of TRDs. In this work, the development, construction and characterization of the TRD with an emphasis on its readout electronics are discussed.

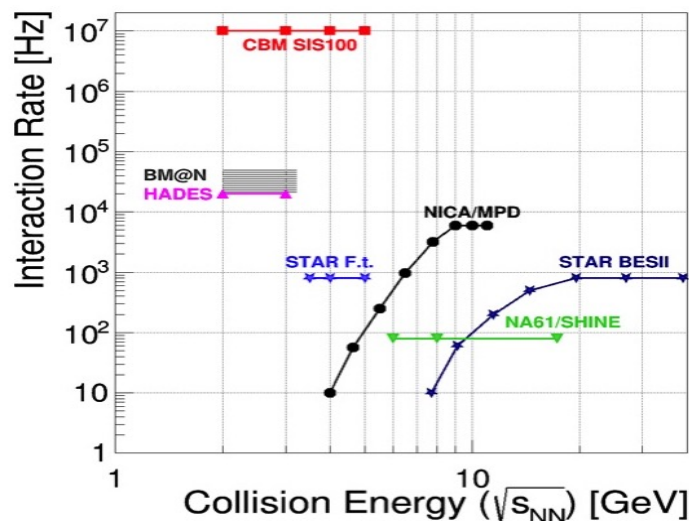


Figure 1.1: Interaction rates achieved by existing and planned heavy-ion experiments as a function of center-of-mass energy. STAR F.t. denotes the fixed-target operation of STAR [2].



# Chapter 2

## Physics Motivation

### 2.1 The Standard Model of Particle Physics

Quantum Mechanics explains the behavior of matter, light and their interactions with energies on the atomic and subatomic scale. Special relativity is a theory that describes the propagation of matter and light at high speed. As the young universe was very small right after the Big Bang and expanding very fast, we need an unified theory of small objects and special relativity to understand it. The combination of quantum mechanics and special relativity led to presently most powerful formulation of fundamental physics: Quantum Field Theory. The unification of the electromagnetic and the weak interaction in 1961 in the course of the development of quantum field theory was the first step to form a theory that describes the interactions between elementary building blocks (quarks and leptons) and the force carriers (bosons). The theory is called the standard model.

Everything in the universe is found to be made of a few basic building blocks called fundamental particles, governed by four fundamental forces (electromagnetic, strong, weak and gravity). Three of the fundamental forces result from the exchange of force-carrier particles known to be bosons. The interactions between those fundamental particles and three fundamental forces and the physical properties of the particles are the subject of the standard model of particle physics.

All matter consists of atoms, and atoms are made of electrons orbiting the nucleus. A nucleus itself consists of particles called protons and neutrons. According to the standard model of particle physics, we can classify particles into two main groups, bosons and fermions. Bosons are particles that obey the Bose-Einstein

statistic as they may occupy the same energy quantum-state, and they have an integer number of spin. Fermions have half integer number of spin and cannot exist in identical quantum-states. The wave function that describes a collection of fermions must be anti-symmetric, while the wave function for a collection of bosons is symmetric. Figures 2.1 and 2.2 show the building blocks of matter and particle classification in the standard model of particle physics.

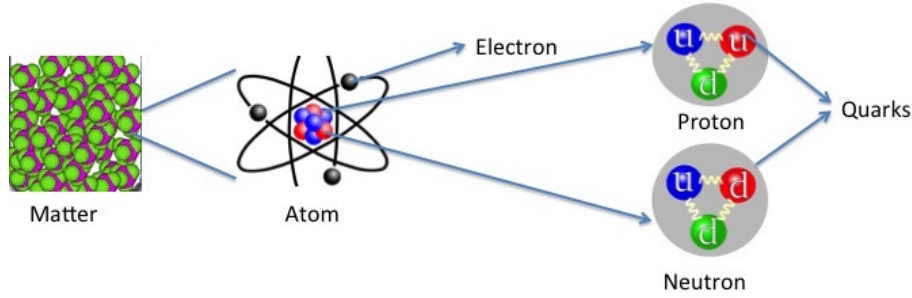


Figure 2.1: Matter constituents. Electrons are bound to the nucleus by the electromagnetic force, while nucleons (protons and neutrons) and quarks are bound together by the strong force.

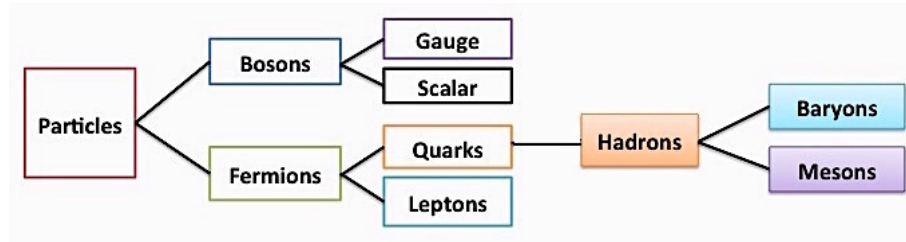


Figure 2.2: Particle classification in the standard model of particle physics.

The fermions itself are classified into two groups (quarks and leptons). Leptons are elementary particles, which do not interact via the strong force. Leptons are divided into two groups: Charged particles ( $e$ ,  $\mu$ ,  $\tau$ ) and uncharged particles ( $\nu_e$ ,  $\nu_\mu$ ,  $\nu_\tau$ ). Quarks are charged particles that interact via the strong force. Quarks combine together, with strong force carriers (gluons), to form hadrons. Three combined quarks (besides potential pentaquarks that are composed of four quarks and one antiquark) are called baryons, and a quark-antiquark pair is called a meson.

Bosons are categorized into two groups: Gauge and scalar. Gauge bosons are force carrier particles with the spin number one while scalar bosons have a spin number equal to zero. The Higgs boson is a scalar boson that is the quantum

excitation of the Higgs field, a fundamental field of crucial importance to particle physics as it is responsible for the mass of all particles. Theory first predicted its existence in the 1960s, and it was discovered at the LHC in 2012. Figure 2.3 depicts the table of elementary particles in the standard model of particle physics with some of their quantum properties.

mass →	$\approx 2.3 \text{ MeV}/c^2$	$\approx 1.275 \text{ GeV}/c^2$	$\approx 173.07 \text{ GeV}/c^2$	0	$\approx 126 \text{ GeV}/c^2$
charge →	$2/3$	$2/3$	$2/3$	0	0
spin →	$1/2$	$1/2$	$1/2$	1	0
	<b>u</b> up	<b>c</b> charm	<b>t</b> top	<b>g</b> gluon	<b>H</b> Higgs boson
<b>QUARKS</b>	$\approx 4.8 \text{ MeV}/c^2$	$\approx 95 \text{ MeV}/c^2$	$\approx 4.18 \text{ GeV}/c^2$	0	
	$-1/3$	$-1/3$	$-1/3$	0	
	$1/2$	$1/2$	$1/2$	1	
	<b>d</b> down	<b>s</b> strange	<b>b</b> bottom	<b><math>\gamma</math></b> photon	
	$0.511 \text{ MeV}/c^2$	$105.7 \text{ MeV}/c^2$	$1.777 \text{ GeV}/c^2$	$91.2 \text{ GeV}/c^2$	
	-1	-1	-1	0	
	$1/2$	$1/2$	$1/2$	1	
	<b>e</b> electron	<b><math>\mu</math></b> muon	<b><math>\tau</math></b> tau	<b>Z</b> Z boson	
<b>LEPTONS</b>	$< 2.2 \text{ eV}/c^2$	$< 0.17 \text{ MeV}/c^2$	$< 15.5 \text{ MeV}/c^2$	$80.4 \text{ GeV}/c^2$	
	0	0	0	$\pm 1$	
	$1/2$	$1/2$	$1/2$	1	
	<b><math>\nu_e</math></b> electron neutrino	<b><math>\nu_\mu</math></b> muon neutrino	<b><math>\nu_\tau</math></b> tau neutrino	<b>W</b> W boson	
					<b>GAUGE BOSONS</b>

Figure 2.3: Table of elementary particles in the standard model of particle physics with their mass, charge and spin properties [3].

## 2.2 Physics of the Compressed Baryonic Matter Experiment

Quantum Electro Dynamics (QED), as an important part of the standard model, is the relativistic quantum field theory of electro-dynamics that describe how light and matter interact. Another prominent part of the standard model is the theory of Quantum Chromo Dynamics, which is the theory of strong interaction (the binding force between nucleus constituents and quarks). The QCD has two properties: Confinement and asymptotic freedom. Confinement is the fact that the force between quarks increases as they are separated. According to this fact, when one tries to force the quarks apart, the energy in the gluon field becomes strong enough to create another quark anti-quark pair (see Fig. 2.4).

Asymptotic freedom means that when the distances between quarks are very short, the binding force between them decreases such that it asymptotically approaches zero for close distances at high momenta. QCD predicts that the strength of the force between quarks changes with distance in a particular calculable way that has been well confirmed in experiments studying high-energy collisions of elementary particles.

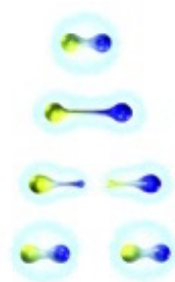


Figure 2.4: The QCD confinement: The separation of quark-antiquark pairs leads to two quark-antiquark pairs [4].

The way the quarks interact strongly with each other is determined by the color property of the quarks in QCD. Every quark carries one color and each anti quark carries one anti-color. The colors are blue, green, red, anti-blue, anti-green and anti-red. Quarks are allowed to interact with each other and form a stable hadron only if the combinations of their colors are colorless (white). Mesons are combinations of a color quark and an anti-color anti-quark that make the mesons colorless. Gluons themselves also carry color so that they can interact with themselves, unlike photons in QED that do not have any electric charge.

## 2.2.1 The Phase Diagram of QCD

A water molecule is made of three atoms, one oxygen and two hydrogen atoms. It can be found in three states of matter, called phases (solid, liquid and gas), depending on the ambient temperature ( $T$ ) and pressure ( $p$ ). By changing the thermodynamic parameters ( $T$  and  $p$ ), one can control which phase is preferred and cause the substance to undergo corresponding phase transformations. Figure 2.5 illustrates the phase diagram of water in the  $(T, p)$  plane.

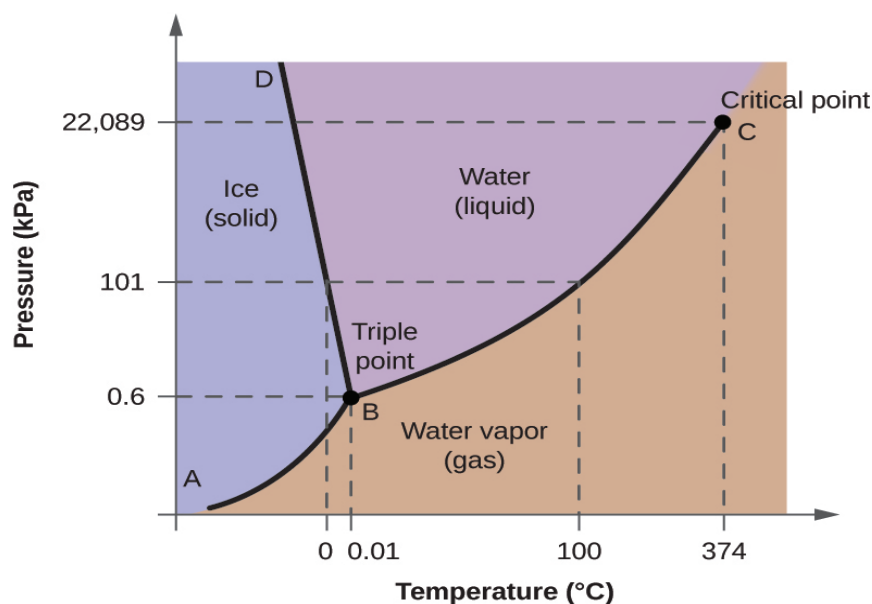


Figure 2.5: Phase diagram for water delineating the thermodynamic domains of three states of matter (solid, liquid and gas) joined together at the triple point (B), situated just above the  $0^{\circ}\text{C}$ . The liquid-gas phase boundary terminates at the *critical point* (C) [5].

The phase diagram of water (Fig. 2.5) shows the different regions where water can be in one phase at a particular temperature and pressure. At the boundary of two phases, the matter (water) is in two phases simultaneously at the same temperature and pressure. However, they differ in their microscopic organization and, as a result, they generally have different particle or energy densities. At this point, one can talk about the *first order of phase transition*. The phase transition line between two phases (liquid and gas) ends at the so-called *critical point* where the differences between coexisting phases cease. The study of the physical properties of a substance under thermodynamic conditions close to the critical point has been a central research interest for decades in condensed matter physics.

Analogous to the atomic matter, e.g. water, nuclear matter (atomic nuclei constituents) are expected to change into different phases at different nuclear matter densities and temperatures. These phase transitions are expected by lattice QCD calculations, and the diagram anticipated by the theory and heavy-ion collision experiments is known as the QCD phase diagram (see Fig. 2.6).

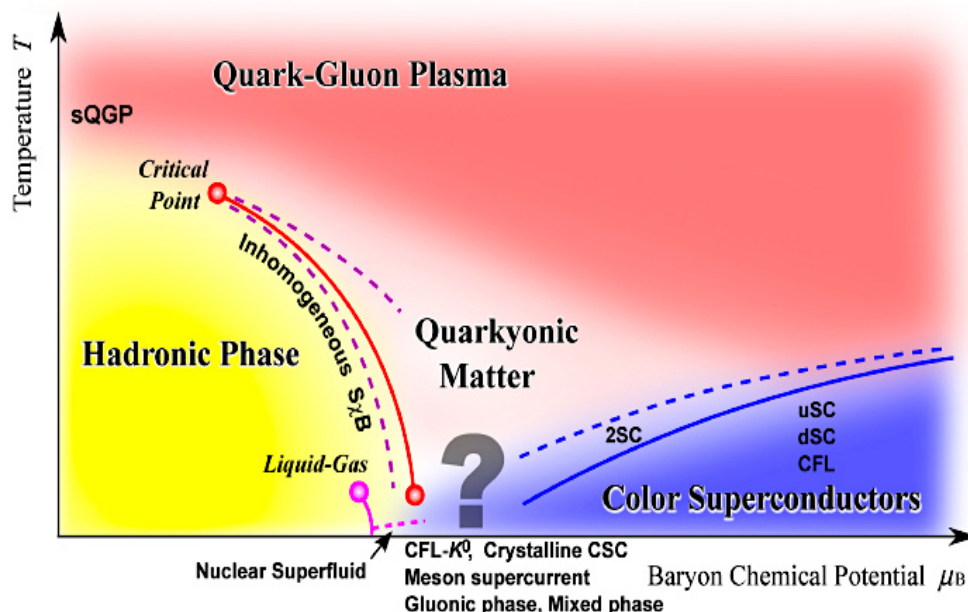


Figure 2.6: The phase diagram for strongly interacting matter in the plane of baryon chemical potential and temperature. When the temperature and/or the density is raised sufficiently, the hadrons dissolve into a quark-gluon plasma. Heavy-ion collision experiments predict a first order transition from hadronic to quark-gluon matter (red-curved line) [6].

Figure 2.6 delineates the phase transitions of nuclear matter depending on the temperature  $T$  and baryon chemical potential  $\mu_B$  (measure of the imbalance between quarks and anti quarks in the system). By increasing the quark densities and keeping the temperature low, we move into a phase of more and more compressed nuclear matter. Following this path corresponds to neutron stars. Eventually a phase transition to quark matter occurs (see Fig. 2.6). At ultra-high densities, we expect to find the Color-Flavor-Locked (CFL) phase of color-superconducting quark matter. The red-curved line indicates the phase transition from confined to unconfined nuclear matter.

The possible existence of a first-order phase transition concerning the chiral phase transition indicates that the transition line in the QCD phase diagram will end at a point known as the QCD critical point or Critical End Point (CEP). The CEP of a first order line is a critical point where the phase transition is of second order. The location of the CEP is a major goal of several heavy-ion collisions programs, including the Facility for Antiproton and Ion Research (FAIR) at GSI, the Helmholtz Centre for Heavy-Ion Research (German: Gesellschaft für Schwerionenforschung).

Several conditions such as the presence of an external magnetic field can affect the location of the CEP, which has noticeable effects on the QCD phase diagram. The intensity of the magnetic field can drive the CEP to lower densities and, eventually, the crossover at zero density between the two phases becomes a first-order chiral phase transition according to the lattice QCD results and model calculations (see Fig. 2.7) [7].

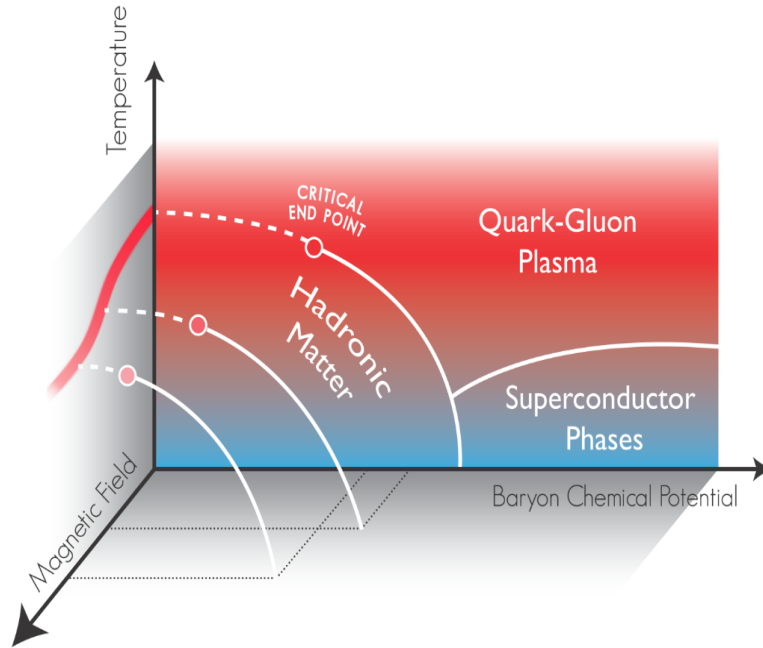


Figure 2.7: The QCD phase diagram in the presence of an external magnetic field predicted by lattice QCD and model calculation. [8].

Heavy-ion collision experiments at relativistic energies can create extreme states of strongly interacting matter reaching very high densities and temperatures. Experiments at LHC and high RHIC energies, study the QCD phase diagram in the region between Quark-Gluon Plasma (QGP) and hadron gas at small baryon chemical potentials, where matter is produced with almost equal numbers of particles and antiparticles. This region simulates the situation in the early universe. The Compressed Baryonic Matter (CBM) experiment, together with the HADES experiment, perform a search program on dense QCD matter at intermediate energies compared to LHC and RHIC. Figure 2.8 depicts the different experiments exploring the different parts of the QCD phase diagram depending on the baryon chemical potential and energy they provide.

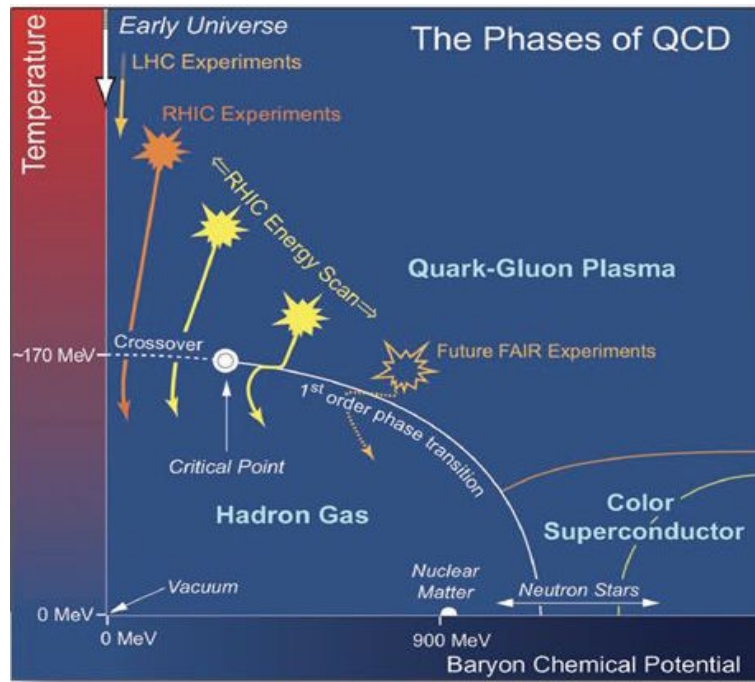


Figure 2.8: The experiments exploring the QCD phase diagram at different energies and baryon chemical densities. The future FAIR facility will explore the 1st order transition at high net-baryon densities and moderate temperatures in comparison to the experiments running at the LHC and RHIC [10].



## 2.2.2 Observables of the CBM Experiment

Colliding heavy nuclei in heavy-ion collision experiment will produce an abundance of rare particles. The fireball produced in the collision emits hadrons giving information on the dense phase of the collision (see Fig. 2.9).

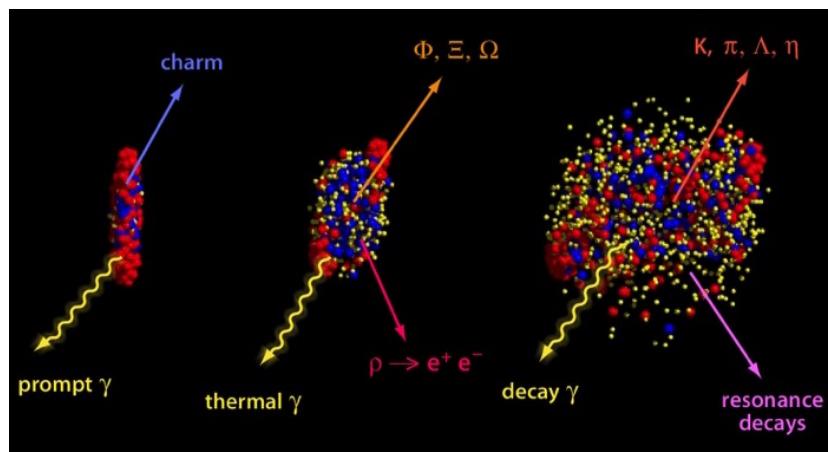


Figure 2.9: Messengers from the dense fireball. From left to right one can see the production of probes during the evolution of the fireball [9].

In the CBM experiment, a comprehensive and systematic (energy and system size) study of all relevant diagnostic probes, including (but not limited to):

- Hadrons, event-by-event fluctuations
- Multi-strange hyperons e.g. ( $\Xi^0$ ,  $\Xi^-$ ,  $\Omega$ ,  $\Omega^-$ )
- Low-mass vector mesons ( $\omega$ ,  $\rho$ ,  $\phi$ )
- Open charm ( $D^0$ ,  $D^\pm$ ,  $\Lambda_c$ )
- Charmonia ( $J/\psi$ ,  $\psi'$ )

will be explored.

The CBM experiment will measure the collective flow of identified particles in the FAIR energy range, including multistrange hyperons and dileptons. The flow of particles not significantly suffering from rescattering, like  $\Omega$  hyperons or  $\phi$  mesons, for which no experimental data exist is of particular interest. These measurements will significantly contribute to our understanding of the QCD matter equation-of-state at neutron star core densities [11].

Event-by-event fluctuations of conserved quantities such as electrical charge, baryon number and strangeness can provide insight into the properties of matter

created in high-energy nuclear collisions. Up to date, no experiment has measured higher-order event-by-event fluctuations at SIS100 energies. The CBM experiment will, for the first time, perform a high-precision study of higher-order fluctuations at various beam energies in order to search for the elusive QCD critical point in the high net baryon density region [11].

## Strangeness

Particles containing strange quarks are important probes of the excited medium created in heavy-ion collisions. High-precision measurements of excitation functions of multi-strange hyperons in A+A collision with different mass numbers ( $A$ ) at SIS100 energies will allow to study the degree of equilibration of the fireball and open the possibility to find a signal for the onset of deconfinement in QCD matter at high net-baryon densities.

The strange hadrons, including multi-strange (anti-) hyperons will be measured in the CBM experiment multi-differentially. The expected particle yields are sufficient to study with unprecedented statistical significance the production and propagation of heavy strange and anti-strange baryons up to  $\Omega^+$  hyperons in the dense nuclear matter [11].

## Dileptons

Dileptons are lepton - anti lepton pairs that are emitted throughout the whole evolution of heavy-ion collisions, offering a unique opportunity to investigate the microscopic properties of strongly interacting matter. Electromagnetic radiation is one of the important probes. In order to minimize systematic errors of dileptons measurement, the CBM experiment investigates dielectron and dimuon pairs in the full mass range from the photon point up to charmonia (a bound state of a charm quark and anti-charm quark) [12].

Vector mesons can directly decay into lepton-anti lepton pairs. One, therefore, aims to infer information on the modifications induced by the medium on specific properties of the vector meson, such as its mass and/or its width, from the invariant mass dilepton spectra [13]. Figure 2.10 shows an invariant mass spectrum only for  $e^-e^+$  pairs.

In the low invariant mass region ( $0 - 1 \text{ GeV}/c^2$ ), the decay products are expected to originate from light vector mesons such as  $\rho$ ,  $\omega$ , and  $\phi$ . In the

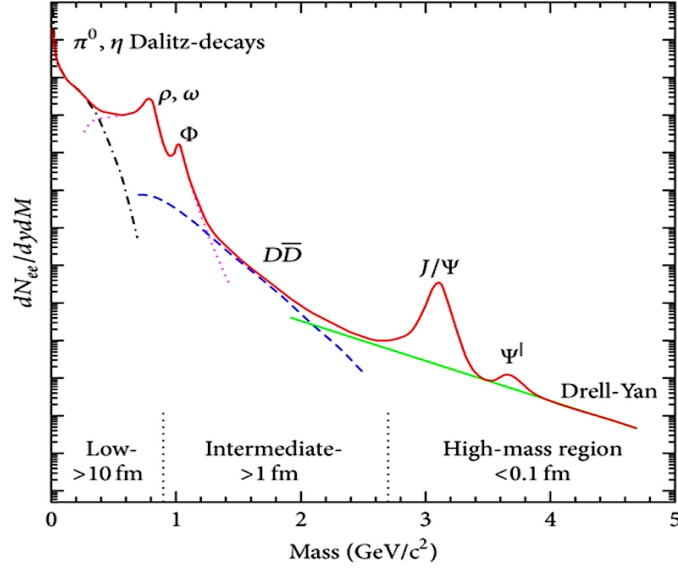


Figure 2.10: The sources of  $e^-e^+$  production as a function of invariant mass in high energy ultra relativistic heavy-ion collisions [14].

intermediate mass region ( $1 - 1.5 \text{ GeV}/c^2$ ), the main contributing processes are low mass vector mesons and open charms. At high masses, over  $2.7 \text{ GeV}/c^2$ , Drell-Yan-Processes and the quark-antiquark annihilation of heavier quarks like charm - anti charm and bottom-anti bottom are relevant processes [15].

### J/ψ Measurement

The J/ψ suppression in nuclear collisions provides the signature for the QGP formation [16]. The J/ψ is a state of a bound charm-anticharm ( $c\bar{c}$ ) quark pair and it is the lightest vector meson of the charmonia [15]. An anomalous J/ψ suppression data is measured by NA50 in Pb+Pb collisions and by NA60 in In+In collisions at top CERN-SPS energies. Up to now, no data on J/ψ production have been measured in the nucleus - nucleus collisions at beam energies below 158A GeV due to the limitations by the absorber technique used in NA50/NA60 [17].

Particles containing charm quarks (e.g.  $D^0$ ,  $D_s$ ,  $D^\pm$ ,  $\Lambda_c$ ) are expected to be generated in the very first stage of interaction. The charm and anti-charm quarks hadronize into D mesons, charmed baryons, or charmonia, depending on their interaction with the medium [16]. Charm production will be studied for the first

time at beam energies close to the production threshold with the CBM experiment at SIS100 energy range. Figure 2.11 illustrates the meson production at SIS100 and SIS300 energy range in central Au+Au collision.

Looking for the rare probes like charmonia ( $J/\psi$ ,  $\psi'$ , etc.) at energies close to their kinematic threshold is one of the important tasks of the CBM experiment. Charmonia can be measured via their decay in di-muons ( $\mu^- - \mu^+$ ) and di-electrons [18]. The CBM experiment will measure charmonia in both the electron and the muon decay channel. The challenge for the electron case is the separation of electrons from hadrons exploiting both the Cherenkov radiation in the RICH detector and the transition radiation in the TRD. The Time – Of – Flight (TOF) detector provides information on pion suppression at low momenta and the Electromagnetic CALorimeter (ECAL) gives this information at high momenta. The simulations show that pion suppression factors of more than  $10^3$  can be reached by combining the information from these detectors. Figure 2.12 shows the  $J/\psi$  signal in the invariant-mass spectrum in e (left) and  $\mu$  (right) decay channels. The  $J/\psi$  peak is well visible above the remaining background [19].

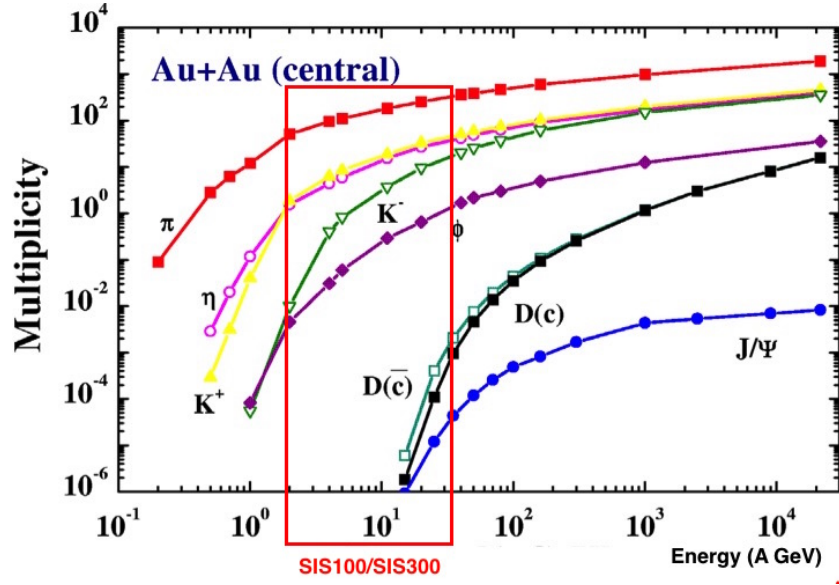


Figure 2.11: Theoretical prediction of meson production in central Au+Au collision. The energy range of SIS100 and SIS300 is shown as the red box [20].

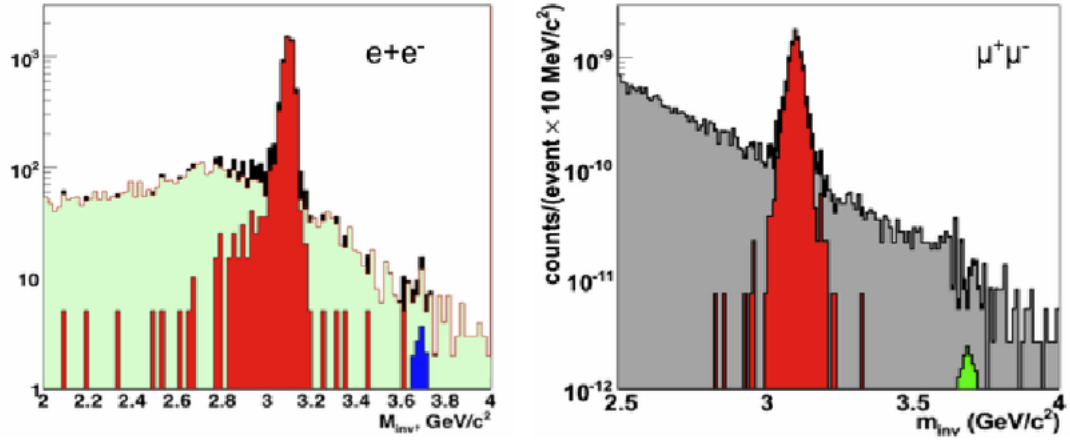


Figure 2.12:  $J/\psi$  signal in the invariant-mass spectrum of electron pairs (left) and muon pairs (right), obtained from simulation of central Au+Au events at 25A GeV. The statistics correspond to 25 days of data taking at 10 MHz interaction rate [19].

## Chapter 3

# Facility for Anti-proton and Ion Research

What is the origin of the elements? What holds nuclei together? Why is the proton 50 times heavier than the combined mass of its constituents (quarks and gluons)? The Facility For Anti-proton and Ion Research (FAIR) is a new and unique international laboratory, which is being constructed in Darmstadt, Germany, dedicated to explore these questions. This highly sophisticated accelerator complex will provide many kinds of ions and antiprotons at unprecedented quality and intensities to be accelerated to create new and highly exotic particles in a series of parallel experimental programs.

The CBM experiment at FAIR will complement studies of the hot quark-gluon plasma state being accomplished with the LHC at CERN, Geneva. The CBM experiment will simulate conditions in the early universe, at the cores of giant stars and in ultra-dense stars.

Figure 3.1 shows the planned layout of FAIR and the experiments. The existing injector complex is shown in blue, and the red lines indicate the planned complex. Two *SchwerIonen-Synchrotron* rings (SIS100 and SIS300) are the major particle accelerators of this facility with 1100 meters in circumference. UNILAC and SIS18 will pre-accelerate the ions before they are injected into the first ring SIS100. To inject high-intensity proton beams, a new proton linear accelerator will be built.

The accelerators SIS100 and SIS300 are different in their magnetic rigidity ( $R$ ) by value of  $R_{SIS100} = 100$  Tm, and  $R_{SIS300} = 300$  Tm, respectively. FAIR provides

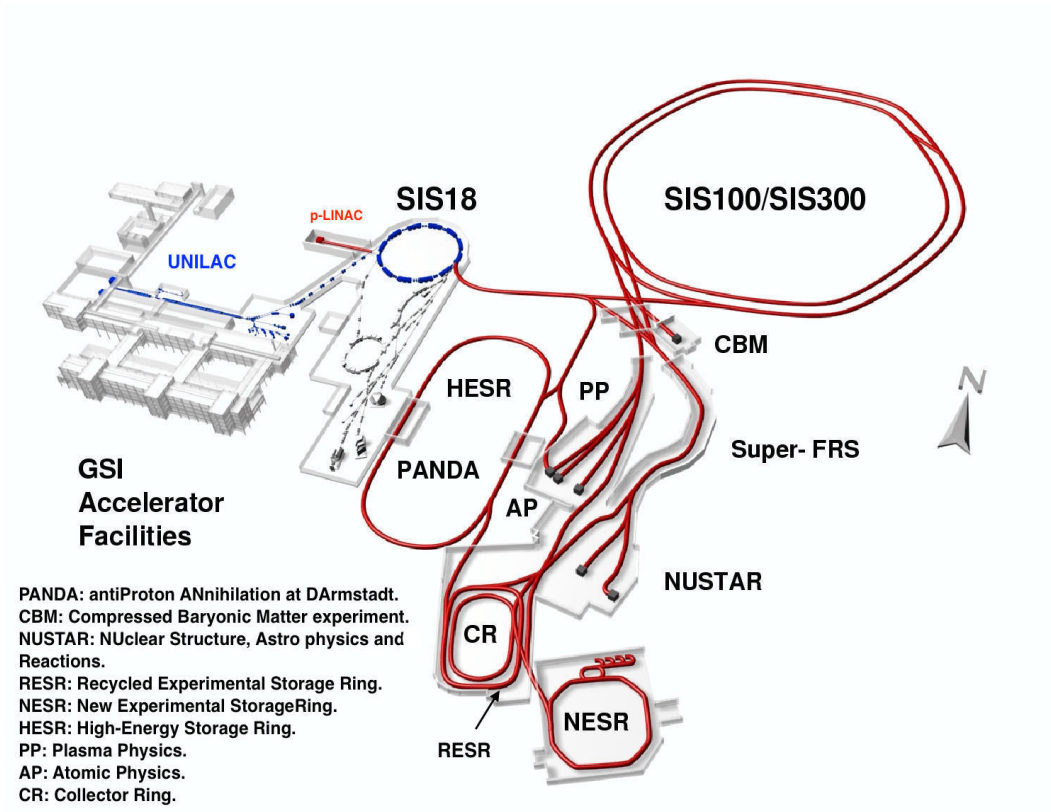


Figure 3.1: Layout of the future FAIR accelerator complex. The existing accelerators (SIS18) are shown in blue and the additional new FAIR complex is shown in red [21].

radioactive ion beams for nuclear astrophysics and nuclear structure physics, anti-proton beams for hadron physics, and heavy nuclei and ion beams for heavy-ion experiment and plasma physics.

The heaviest unstable nuclei will be produced in large enough quantities for precision studies. They are then directed to three experimental areas, the high-energy branch, the low-energy branch and the ring branch where exotic nuclei are collected, cooled and stored in the FAIR ring systems (CR-RESR-NESR).

Antiproton beams are made by bombarding a target with protons, cooled in the two cooler rings (CR and RESR) and then stored in the High-Energy Storage Ring (HESR). The interaction region is enclosed by the multi-purpose anti-Proton ANnihilation at DArmstadt (PANDA) experiment.

In the FAIR complex, the SIS100 synchrotron accelerates heavy nuclei such



as Au in an energy range from 2 to 11.4 GeV, light nuclei like C and Ca up to 14.4 GeV and protons up to 29 GeV. In the next stage of FAIR, the SIS300 synchrotron delivers heavy-ion beams up to 35.4 GeV, light ions up to 45.4 GeV and protons up to 90 GeV energy to explore the lower net-baryon densities. Collision rates up to  $10^7$  per second are required to produce very rare probes with unprecedented statistics in this energy range. The high beam intensities up to  $10^9$  ions per second allow access to most rare probes like charm production near threshold [22].

Figure 3.2 shows an environmental view of the FAIR complex. The major fields of physics that will be scrutinized at FAIR are Atomic, Plasma Physics and Applications (APPA physics), nuclear matter physics (Compressed Baryonic Matter experiment), Nuclear Structure, Astrophysics and Reactions (NUSTAR physics). The Compressed Baryonic Matter (CBM) experiment as the main topic of this dissertation will be described in detail.

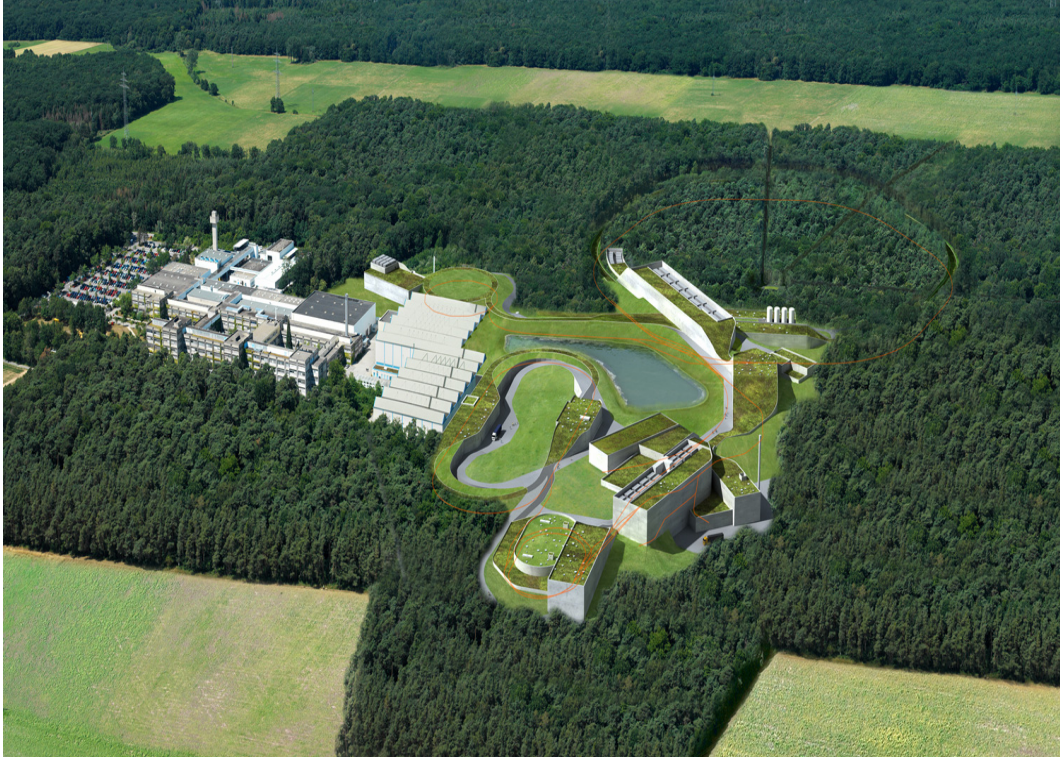


Figure 3.2: Environmental view of the FAIR complex. Beam lines are highlighted in red [21].



## Chapter 4

# The Compressed Baryonic Matter Experiment

The strong force is responsible for binding the constituents of atomic nuclei. The strong force as part of the standard model of elementary particle physics is well established. However, the phase transition of the confinement of quarks and gluons into hadrons and the generation of mass is still unperceived. Creating compressed baryonic matter in the laboratory and study the results of the experiment, will assist us to learn more about the QCD phase diagram and phase transition of strongly interacting matter at highest net-baryon densities and moderate temperatures [23].

The CBM experiment is being designed to measure hadronic, leptonic and photonic observables at interaction rates up to 10 MHz [24]. The beams will collide with a fixed target to produce a significant amount of rare probes. This high interaction rate requires very fast and precise particle detection systems. Two main detector setups (electron identification and muon identification) are planned for the CBM experiment in the SIS100 energy range at FAIR. The TRD setup in the SIS100 and the SIS300 energy range will be discussed in the TRD section.

It is possible to determine particle multiplicities and phase-space distributions, the collision centrality and the reaction plane in the CBM experiment. The simultaneous measurement of various particles permits the study of cross correlations [25]. To reach this aim, two detector setups for the SIS100 beams are planned to identify electrons and muons. Figures 4.1 and 4.2 depict the electron identification setup and the muon identification setup, respectively.

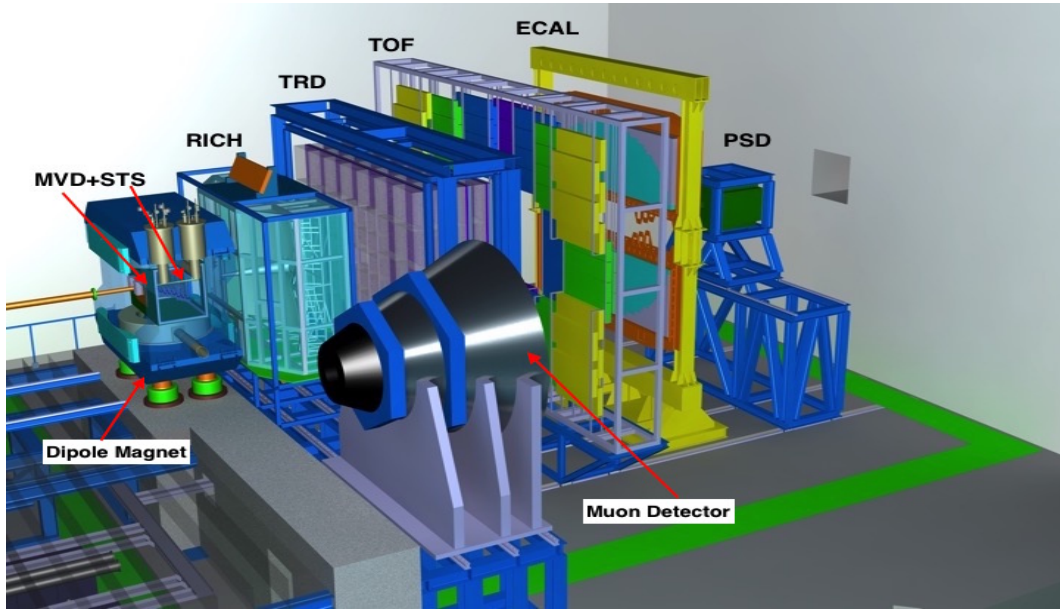


Figure 4.1: Electron identification setup in the CBM experiment planned for SIS100 at FAIR [25].

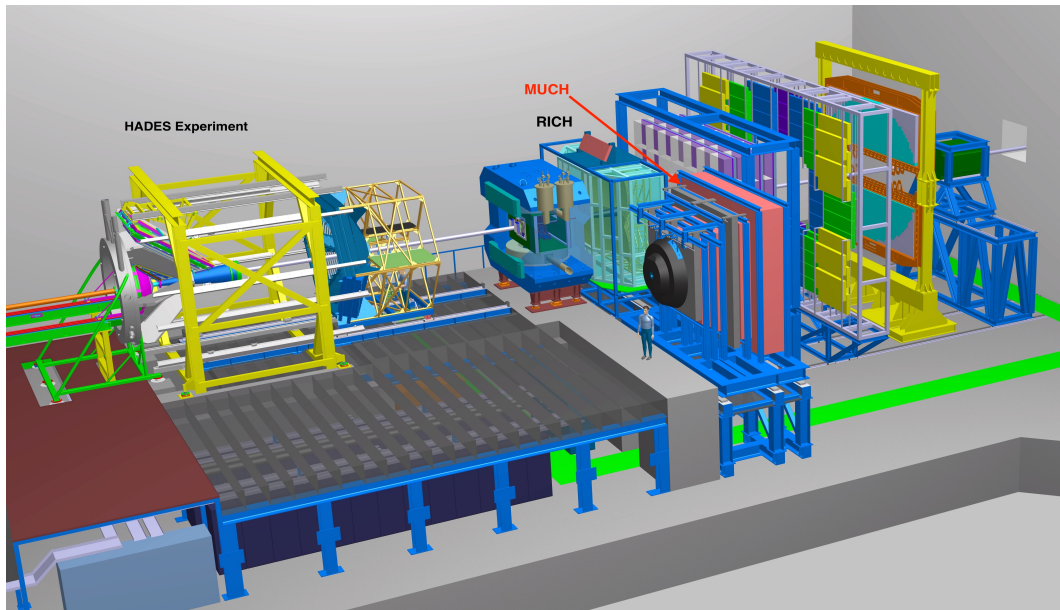


Figure 4.2: The HADES and the CBM experiment setup planned for SIS100 at FAIR. For the muon identification setup in the CBM experiment, the RICH will be replaced by the MUCH detector system [25].

In the electron identification setup, the Micro Vertex Detector (MVD) and a high-resolution Silicon Tracking System (STS), as the first part of the setup following the downstream direction, are located behind the collision vertex, which is surrounded by the superconducting dipole magnet. The major task of the STS is to measure the trajectories and momenta of charged particles originating from the interactions of heavy-ion beams with nuclear targets [26], and the main task of the MVD is the reconstruction of D mesons in heavy-ion collisions at FAIR energies [27].

The Ring Imaging Cherenkov (RICH) detector and the TRD will be placed outside of the magnet to identify electrons in the momentum range relevant for low-mass vector meson and charmonium measurements. The TOF detector, consisting of an array of resistive plate chambers, will be used for hadron identification purposes. The ECAL completes the setup and will be used to identify photons and electrons [28].

The RICH detector will be movable in order to arrange the experiment for the muon identification setup. Here, the MUon CHamber (MUCH) will be inserted (see Fig. 4.1). In the CBM experiment, the polar aperture of  $2.5^\circ - 25^\circ$  is equipped throughout by all detector systems to cover the forward hemisphere in the laboratory frame (see Fig. 4.6) [11].

The CBM experiment will be set up right after the High Acceptance Di-Electron Spectrometer (HADES) in the same beam line and cave. Both, the HADES and the CBM experiments will be operated in the same cave and will use the same beam line in the initial phase of the SIS100 operation (see Fig. 4.3).

In this section, every sub-detector of the CBM experiment and its physics objective, excluding the TRD, is briefly explained. As this work addresses the TRD and its readout electronics significantly, the TRD in the CBM experiment will be elucidated in a separate section.

## 4.1 Superconducting Dipole Magnet

The superconducting dipole magnet is a H-type magnet with cylindrical superconducting coils in two separate cryostats and a warm iron yoke. Each coil has 1749 turns and will be cooled down by liquid helium. The magnet has a large cavity ( $1.4 \times 2.5 \text{ m}^2$ ) in order to accommodate the target, the MVD and the STS. It will provide a magnetic field with total bending power of 1 Tm over a length of

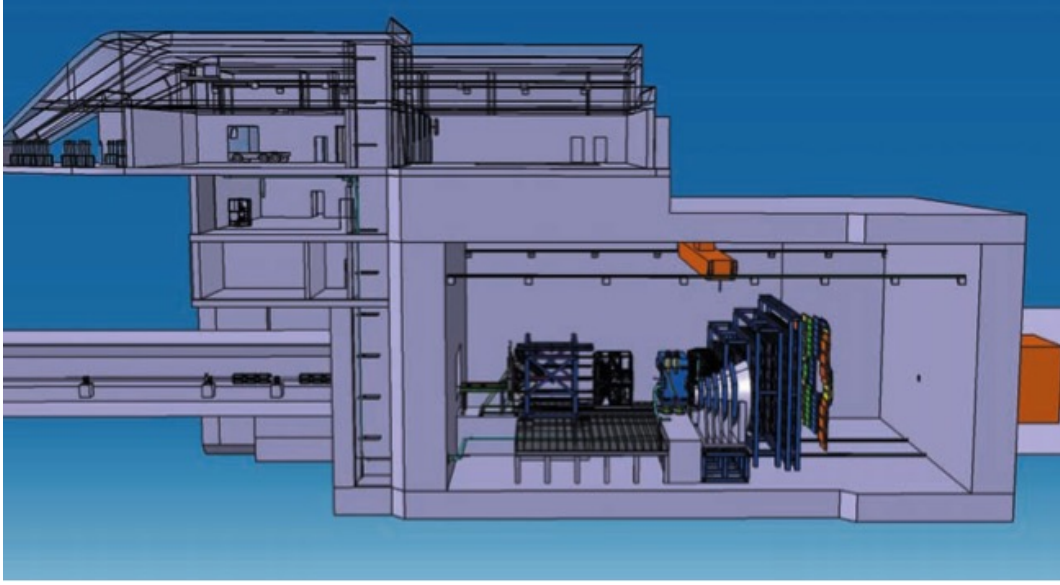


Figure 4.3: Illustration of the building where the CBM and HADES experiments will be located.

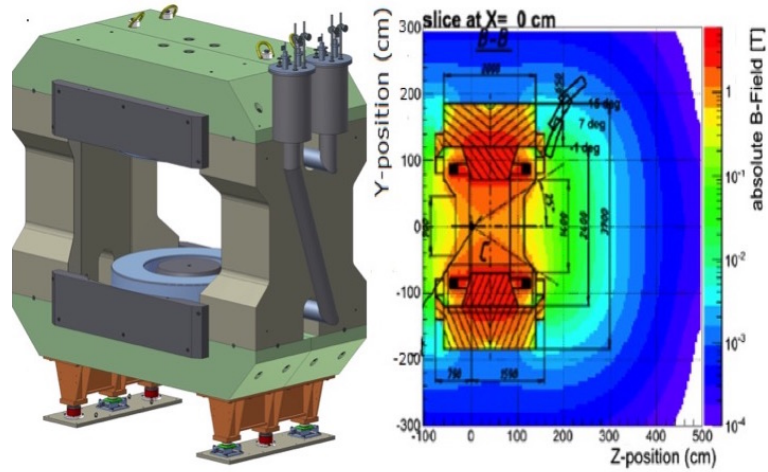


Figure 4.4: Perspective view of the CBM dipole magnet with the support (left), and magnetic field map (right) [29].

1 m from the target. The superconducting magnet will store about 5.15 MJ at its operating current of 686 A. Figure 4.4 shows a perspective view of the CBM dipole magnet with the support (left) and the magnetic-field map (right) [30].

## 4.2 Detector Systems

### Micro Vertex Detector

The Micro Vertex Detector (MVD) is the first tracking device whose first station is placed only 5 cm downstream of the fixed target. It improves the vertex resolution of the CBM tracking system to identify rare particles by the spatial displacement of their decay vertices. The MVD for the CBM experiment has a large geometrical acceptance that enables it to track low-momentum particles, which can improve the background suppression capability in dielectron measurements. Figure 4.5 illustrates a sample of the MVD designed for the CBM experiment (left), and the orientation of the MVD, the target and the STS (right).

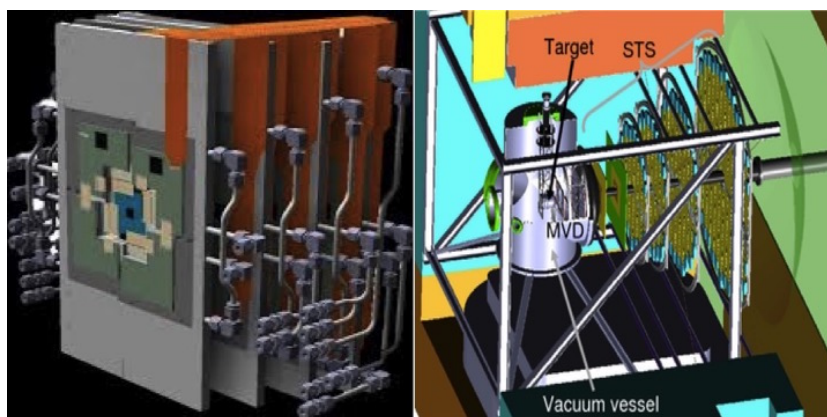


Figure 4.5: An illustration of the MVD (left) [31]. The MVD is near target, which both are enclosed in the vacuum vessel. STS layers are the next detector system (right) [32].

### Silicon Tracking System

The STS will be used for the reconstruction of the tracks of charged particles and the determination of their momenta. It consists of eight tracking stations placed between 30 cm and 100 cm away from the target. Each station will be constructed from 300  $\mu\text{m}$  double-sided silicon micro-strip sensors with outer dimensions of  $6.2 \times 2.2 \text{ cm}^2$ ,  $6.2 \times 4.2 \text{ cm}^2$ ,  $6.2 \times 6.2 \text{ cm}^2$  and  $6.2 \times 12.2 \text{ cm}^2$ , that will be accommodated downstream of the target inside the superconducting magnet. The STS will provide a track reconstruction efficiency for fast primary tracks on the level of 95% and higher. A cross-section of the STS in the magnet and its polar acceptance angle ( $2.5^\circ - 25^\circ$ ) is shown on Fig. 4.6.



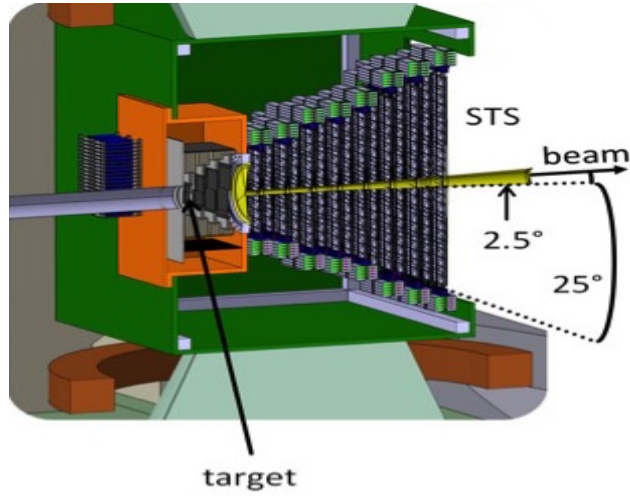


Figure 4.6: Conceptual design of the Silicon Tracking System, showing a cut through the detector in the dipole magnet and the acceptance polar angle [33].

The STS comprises 896 detector modules, including 120 double-sided micro strip sensors that are mounted on ladder-like support structures. There are 4 – 5 modules in each ladder. Each module consists of sensors, analog micro cables and front-end boards. To provide the optimal spatial resolution in the magnet's bending plane along the horizontal axis, the sensors are tilted  $7.5^\circ$  between the front and back side strips. Figure 4.7 shows the eight stations of the STS, its mechanical unit and a ladder [15, 34].

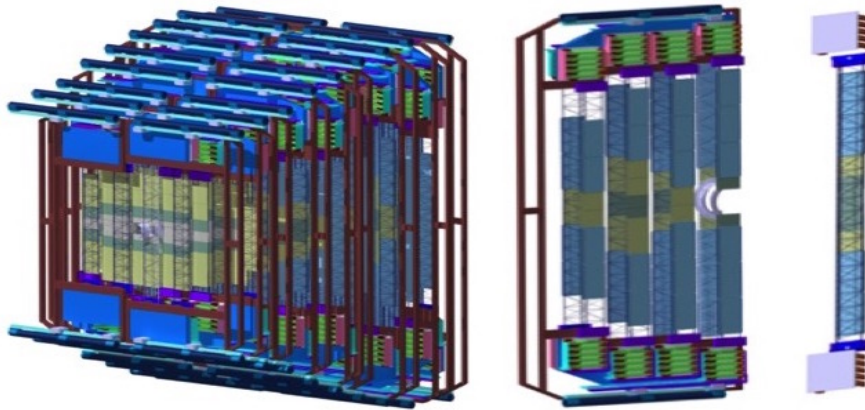


Figure 4.7: Eight tracking stations of STS to be mounted on the detector's main support frame (left), the mechanical unit (middle) and a ladder (right) [33].

## Ring Imaging Cherenkov Detector

The RICH Detector in the CBM experiment is designed to identify electrons in the momentum range resulting from low-mass vector-meson decays, i.e. up to 5 – 6 GeV/ $c$ . When a charged particle passes through a dielectric medium, it emits electromagnetic radiation (*Cherenkov radiation*) if its velocity is above the speed of light in the medium.

$$c > v_p > \frac{c}{n} \quad (4.1)$$

Where  $v_p$  is the speed of particle in medium,  $n$  is the refraction index and  $c$  is the speed of light in the vacuum. The right part of the Eq. (4.1) indicates the speed of light in the medium. By measuring the angle of the Cherenkov radiation, the identification of charged particles is achieved. A pion suppression factor in the order of 500 – 1000 is required for a sufficiently pure electron sample. The RICH detector together with the TRD, will provide a pion suppression factor of  $10^4$  in the CBM experiment.

To reflect the Cherenkov light cones on the 2.4 m<sup>2</sup> photo-detector plane, spherical glass mirrors with Al + MgF<sub>2</sub> coating will be used. The photo-detector plane will be equipped with the Hamamatsu H8500 multi-anode photo-multiplier tubes that in total have 55,000 channels. CO<sub>2</sub> as a gas radiator (1.7 m length) will be used as it is needed to separate electron and pions with momenta up to 10 GeV/ $c$ . Figure 4.8 illustrates technical drawing of the CBM–RICH detector system [35].

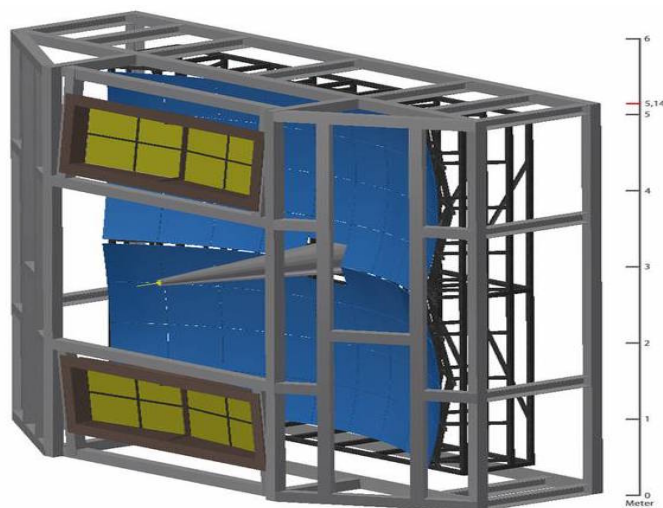


Figure 4.8: Technical drawing of the CBM-RICH detector system [35]. The mirrors are shown in blue.

## Time-Of-Flight Detector

In the CBM experiment, an array of Multi-gap Resistive Plate Chambers (MRPC) and the large Time-Of-Flight (TOF) detector system to identify hadrons due to its good time resolution. Particle identification is done by measuring its momentum and its time of flight:

$$m = \frac{p}{\gamma\beta c} = \frac{p\sqrt{1-\beta^2}}{\beta c} \quad (4.2)$$

with:  $\beta = \frac{L}{c\Delta t} = \frac{v}{c}$  and  $\gamma = \frac{E}{m} = \frac{1}{\sqrt{1-\beta^2}}$

Where  $L$  is the flight path of the particle,  $\Delta t$  is the time difference between the start and stop signal received by the TOF detector,  $p$  is the momentum of the particle and  $c$  is the speed of light in the vacuum. The TOF wall area is about  $10 \times 15 \text{ m}^2$  and it will be placed 6 m downstream of the target for measurements at the SIS100 and 10 m from the target at the SIS300. Approximately 60,000 independent cells on the TOF wall provide a time resolution of about 80 ps. Figure 4.9 depicts the upper view of the TOF wall (left), and simulation of the ability of the TOF system to separate kaons and pions up to 3 GeV/ $c$  and proton up to 7 GeV/ $c$  (right).

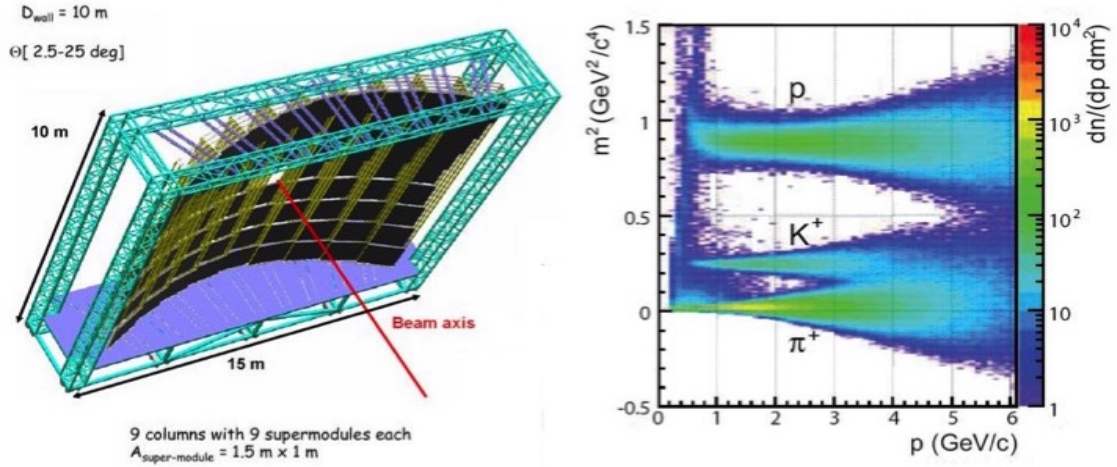


Figure 4.9: (Left) The upper view of the TOF wall, (Right) The simulation of particle separation for the TOF in the SIS300 energy range. Kaons and pions can be separated up to 3 GeV/ $c$  while protons can be identified up to 7 GeV/ $c$  by the TOF system in the CBM experiment [37].

In order to handle the high-rate intensity, the Resistive Plate Chambers (RPC) should be able to cope with a rate of more than 20 kHz/cm<sup>2</sup> [38].



## Muon Chamber System

The MUon CHamber (MUCH) will be used for the measurement of low mass vector meson and charmonia via its decay into muon pairs, e.g. ( $J/\psi \rightarrow \mu^- + \mu^+$ ). In the setup for the SIS100, the MUCH consists of three detector triplets and for the next stage (the SIS300), it will be upgraded to the full system with six triplets. Muon identification can be done by tracking the particles through a sandwich-shaped hadron absorber, which is made of iron plates of 20, 20, 20, 30, 35 and 100 cm thicknesses, and through triplets of gaseous tracking chambers, placed between the six absorber stations (see Fig. 4.10) [39].

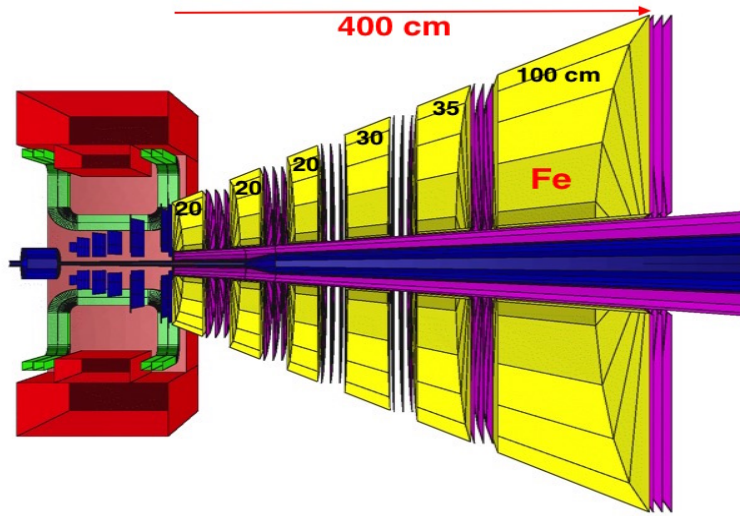


Figure 4.10: The sandwich-shaped Muon Chamber consists of six hadron absorbers made of iron plates (yellow parts), and triplets of gaseous tracking chambers placed between the absorber [40].

To cope with high rates of up to 1 hit/cm<sup>2</sup> per event in the first detector layers, the muon chambers will be based on the Gas Electron Multiplier (GEM) technology. Several multi-GEM prototypes ( $10 \times 10$  cm<sup>2</sup>) have been built and tested with radioactive sources and proton and pion/muon beams. An efficiency of 90% of particle identification is achieved [39].

## Electromagnetic calorimeter

In the electron identification setup, an Electromagnetic CALorimeter (ECAL) will be used to measure direct photons and decay photons from neutral mesons, e.g.  $\pi^0$  ( $\pi^0 \rightarrow \gamma + \gamma$ ) and  $\eta$  ( $\eta \rightarrow 2\gamma$  or  $\eta \rightarrow \pi^+ + \pi^- + \gamma$ ) [41]. The ECAL will be made of 140 modularized layers of 1 mm lead followed by 1 mm scintillator, in cell sizes of  $3 \times 3 \text{ cm}^2$ ,  $6 \times 6 \text{ cm}^2$  and  $12 \times 12 \text{ cm}^2$ . The modules will be assembled on a wall or in a tower geometry and placed in variable distances from the target [42].

## Projectile Spectator Detector

The last detector system in both the electron and the muon setups is the Projectile Spectator Detector (PSD). The PSD will be used to determine the collision centrality and the orientation of an event plane. It works via measuring the energy distribution of the projectile nuclei fragments (spectators) and forward going particles produced close to the beam rapidity. The PSD consists of fully compensating 44 individual modules, each with 60 lead-scintillator calorimeter layers, which provide high and uniform energy resolution. It faces the beam with a surface of  $20 \times 20 \text{ cm}^2$ . The PSD detector is positioned at 8 m from the target at the SIS100 and at 15 m away from the target for the SIS300 energies [42].

## Readout Electronics, Data Acquisition and On-line Event Selection

The CBM experiment will run at high reaction rates with high event statistics. The measurements of rare probes require event rates of about 10 MHz (up to  $10^7$  collision rates per second), while the event selection requires complex global triggers like a secondary vertex search. Consequently, the CBM experiment needs a fast self-triggered detector front-end and data readout architecture. Several readout ASICs (Application-Specific Integrated Circuits) are under development for the CBM detector systems. The First-Level Event Selector (FLES) is chosen for the CBM experiment to receive all hits and perform online event selection on the 1 TByte/s input data stream. From all detector systems, the data messages will be shipped via fast optical links to a readout buffer. The data are then passed via a high-throughput event-building network to a large computer farm (FLES), where online event selection is performed [43].

In order to determine an event, the formation of pre-events by time-slice sorting of detector hits, followed by track finding, track fitting and the assignments

of tracks to interactions are applied [42]. Figure 4.11 demonstrates the CBM readout chain. The ASICs (FEE and GBT) on or near the detectors collect the raw data from the detectors and send them to the data processing part, a Field-Programmable Gate Array (FPGA), in the CBM control room for building micro slice containers. After time synchronization and/or slow control configuration, the data transfer to the FLIB (FLES Interface Board), which provides macro slice containers and then to the FLES in the Green cube for event building, reconstruction event selection and monitoring. The Green cube is a computing center where online event building and selection will be performed (see Fig. 4.12).

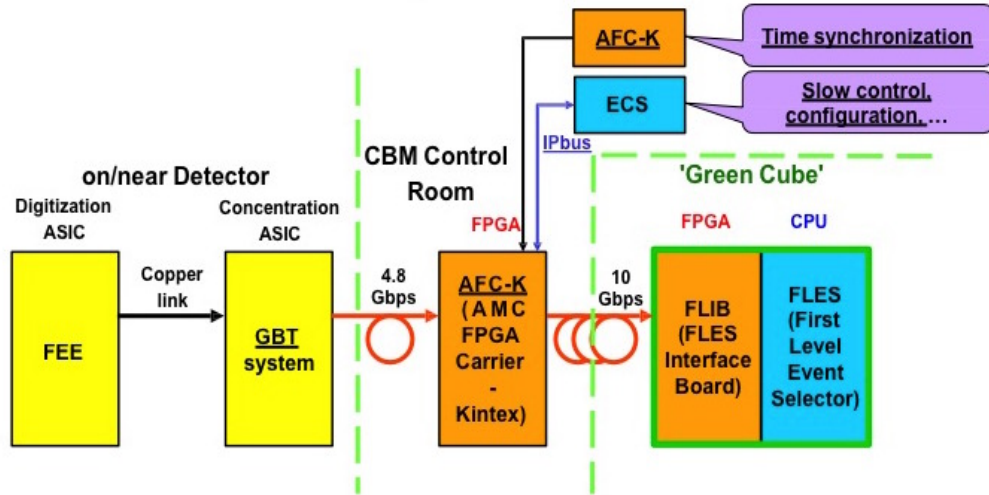


Figure 4.11: Diagram of the CBM readout chain. The yellow parts indicate the electronics on/near detectors, which collect the raw data and send them to the data processing part (CBM control room) to build micro slice containers. The data will be transferred to the FLIB and the FLES to build macro slice containers and perform event-building, event-reconstruction, event-selection and monitoring [44].

The Technical Design Reports (TDR) of the CBM detector systems are submitted to FAIR until the mid of 2017. The production of components and the construction of the systems are planned to be completed by 2018. The sub-system installation into the CBM cave will be ready at the end of 2020 and most of the sub-systems are ready for the first beam time provided by the SIS100 until 2021 [45].

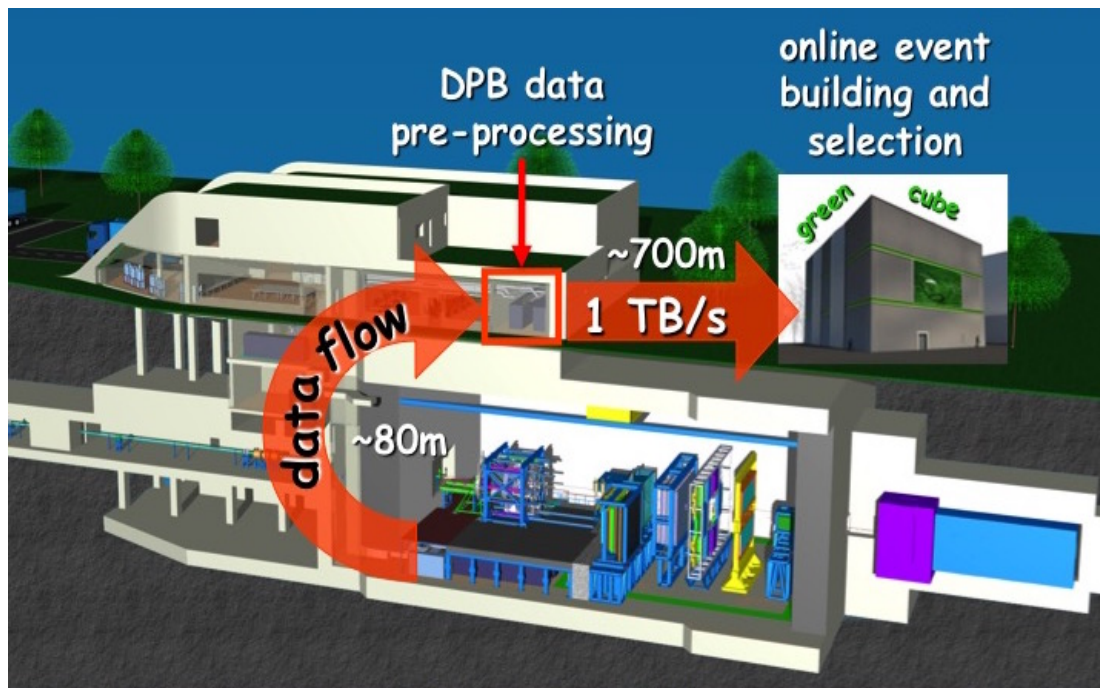


Figure 4.12: Schematic of the CBM and the HADES cave (underground) and the CBM control room and green cube, where online event building and selection will be performed (on the ground) [92].

# Chapter 5

## Transition Radiation Detector

A particle detector can connect – through adequate amplification – one of our sensory organs or a computer with the effect produced by the interaction of the particle with the matter. In heavy-ion collision experiments, a Transition Radiation Detector (TRD) is used to identify electrons. To understand better how the TRD works, a description of the interaction of charged particles and photons with matter is useful. In this chapter, different forms of interaction of photons and charged particles with matter, the working principle and design features of the TRD for the CBM experiment will be explained.

### 5.1 Gamma- and X-ray Interaction in Matter

The dominant interactions of x- and  $\gamma$ -ray in matter are:

- Photoelectric effect
- Compton effect
- Pair production
- Rayleigh (coherent) scattering
- Photonuclear interactions.

The first three interactions result in the transfer of energy to matter in many Coulomb-force interactions along their tracks. In Rayleigh scattering, the photon is scattered by the combined action of the whole atom. The photon is merely redirected within a small angle with no energy loss, and that is why the event is elastic. In this interaction, the atom moves enough to conserve the momentum.

The photoelectric, Compton and pair production interaction domains depend on both the photon quantum energy ( $E_\nu = h\nu$ ), where  $h$  is Plank's constant and  $\nu$  is the frequency of the radiation, and the atomic number  $Z$  of the absorbing medium. Figure 5.1 presents the regions in which each interaction predominates for matter with atomic number  $Z$  and photons with energy  $E_\nu$ . The curves indicate where two interactions are equally probable. The  $\sigma_f$ ,  $\sigma_c$  and  $\sigma_p$  are the cross sections of the photoelectric effect, the Compton effect and pair production, respectively. In low  $Z$  medium and for the photons with medium energies, the Compton effect is dominant. For photons with lower energies, the photoelectric effect takes over, and pair production takes place with photons at high energies [46].

The energy range of x-rays, which is of interest of this work in terms of transition radiation, is between 100 eV–100 keV and the atomic number of Xe and Ar (the gases in which the TRD is filled) are 54 and 18, respectively.

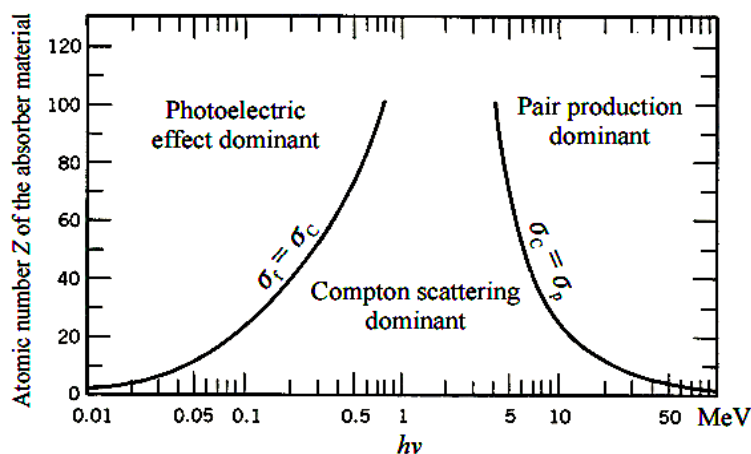


Figure 5.1: The relative importance of various processes of photon radiation interaction with matter [47].  $\sigma_f$ ,  $\sigma_c$  and  $\sigma_p$  are the cross sections of the photoelectric effect, the Compton effect and pair production, respectively. The curves show where the two interactions are equally probable.

## Photoelectric Effect

A photoelectric effect takes place when a photon strikes an atomic-shell electron, gives enough kinetic energy to the electron with potential energy  $E_b$  to eject it from the atom. The photon vanishes, giving a kinetic energy of  $T = h\nu - E_b$  to the electron, which departs at an angle  $\theta$  relative to the incident photon's direction. To

conserve the momentum, the atom shifts away at an angle  $\phi$  with a new momentum  $\rho_a$  and the electron carries out momentum  $\rho$  (see Fig. 5.2).

The photoelectric effect happens only if the quantum energy of a photon  $h\nu$  is higher than the potential energy  $E_b$  of an atomic-shell electron ( $h\nu > E_b$ ) [46]. The photoelectric effect is dominant in case of low energy photons (mostly below the x-ray energy range) interacting with high  $Z$  materials. In this interaction, photoelectrons tend to be emitted in the direction of the electric field of the incident photon. The direction of the electric field of the incident photon is the direction of its polarization (if it polarizes linearly)<sup>1</sup>. The higher the energy of the incident photon, the lower the scattering angle  $\theta$  of the photoelectron is. However, theoretically,  $\theta = 0$  is forbidden because that is perpendicular to the electric field vector of the incident photon [46].

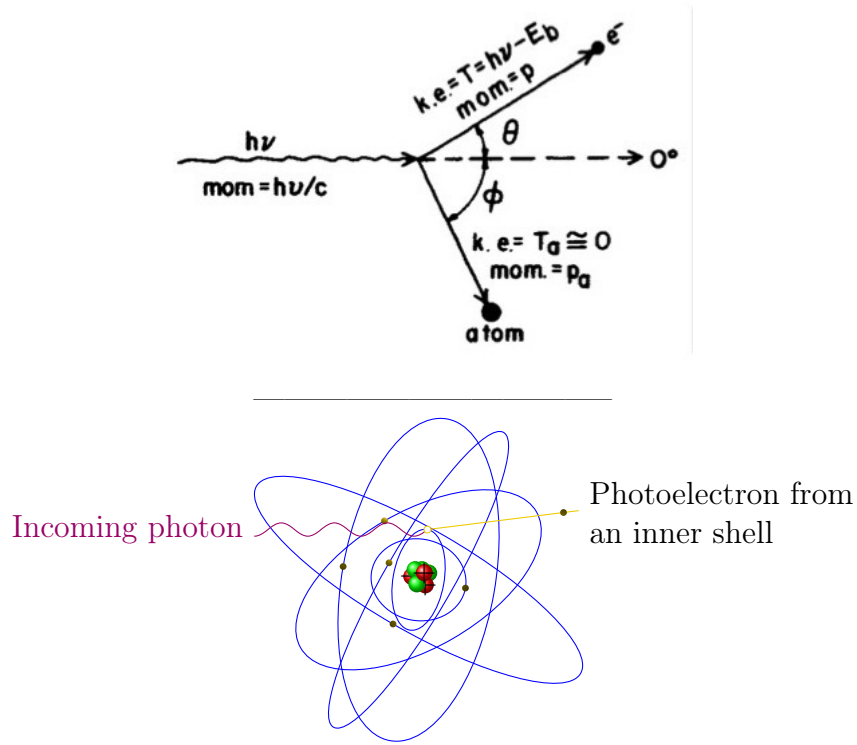


Figure 5.2: Kinematics of the photoelectric effect (upper panel) [46]. A photon with energy  $h\nu$  incident from the left hits an electron in an atom with binding energy  $E_b$ . Atomic schematic of the photoelectric event (lower panel).

<sup>1</sup>Linear polarization of the electromagnetic radiation is a confinement of the electric field vector (or magnetic-field vector) to a given plane along the direction of propagation.

## Compton Effect

In the Compton effect, a photon of energy  $h\nu$  collides inelastically with an electron, giving a part of its energy to the electron, and emerges from the scattering with a lower wavelength than before the collision. Figure 5.3 shows the kinematics of the Compton effect. The initial energy (and therefore momentum) of the electron is assumed to be zero. After the collision, the electron departs at an angle  $\theta$  and the photon scatters at an angle  $\phi$  relative to the incident photon's direction. The kinematics of the interaction can be solved by applying conservation of both energy and momentum. Equations 5.1 and 5.2 indicate energy and momentum conservation, respectively. The momentum conservation is along the original photon direction ( $0^\circ$ ) [46].

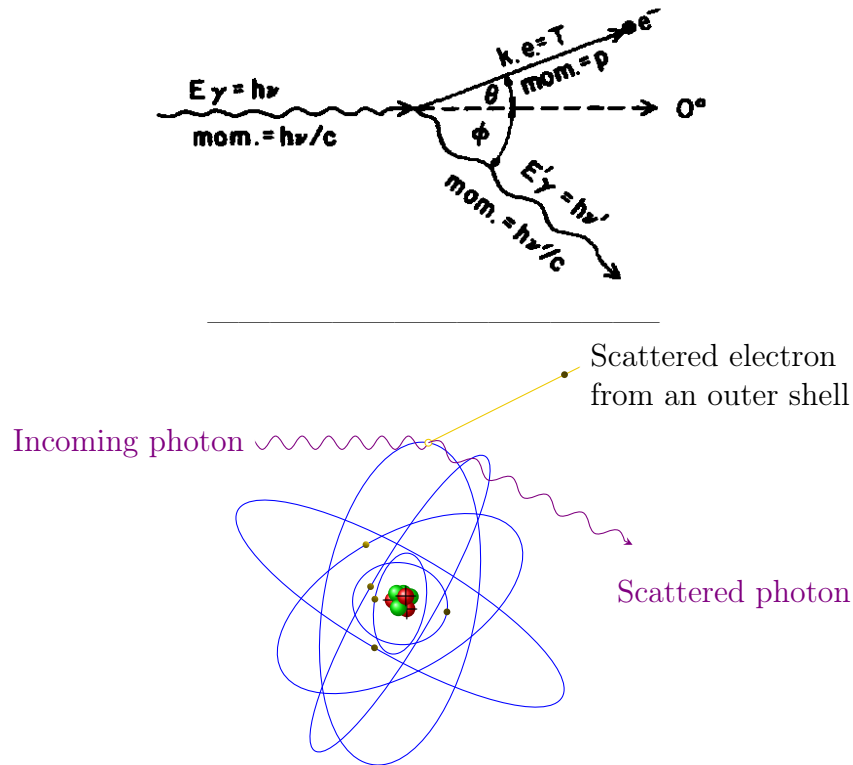


Figure 5.3: Kinematics of the Compton effect (upper panel) [46]. A photon with momentum  $h\nu/c$  and quantum energy  $h\nu$  strikes with an electron and scatters with a lower energy at an angle  $\phi$ . To conserve the momentum, the electron departs with a momentum of  $p$ . The lower panel shows an atomic schematic of the Compton effect.

$$T = h\nu - h\nu' \quad (5.1)$$



$$h\nu/c = h\nu'/c \cos \phi + \rho \cos \theta \quad (5.2)$$

where  $T$  is the kinetic energy that the electron gets from the photon,  $h\nu$  is the initial energy of the photon and  $h\nu'$  is the photon's energy after the collision. In Eq. 5.2,  $c$  is the speed of light in the vacuum.

## Pair Production

In a Coulomb field (usually near an atomic nucleus), a photon can disappear and give rise to an electron and a positron. For pair production to occur in the nuclear field, a minimum photon energy of  $2m_0c^2$ , where  $m_0$  is the mass of the electron, is required. Figure 5.4 illustrates a pair production by a photon in a nuclear field. The whole quantum energy of the photon ( $h\nu$ ) transforms into the creation of the electron-positron pair with kinetic energies  $T^-$  and  $T^+$ . The energy-conservation equation, ignoring the small kinetic energy given to the nucleus by the photon, is [46]:

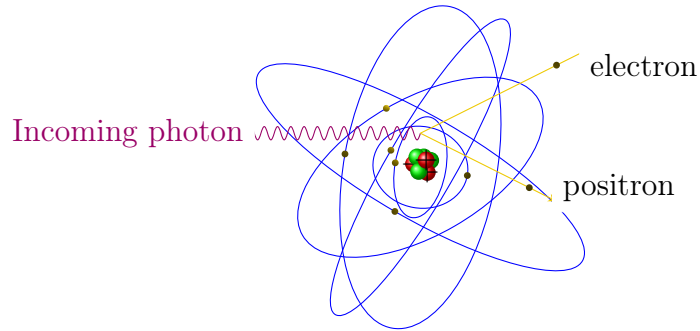
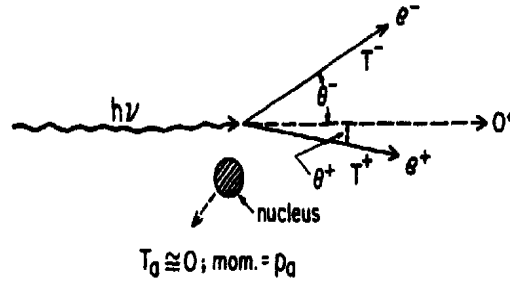


Figure 5.4: Kinematic of a pair production event (upper panel) [46]. A photon of minimum quantum energy  $h\nu = 2m_0c^2$  transforms into an electron-positron pair in the Coulomb field of an atomic nucleus. The lower panel shows an atomic schematic of the pair production.

$$h\nu = 2m_0c^2 + T^- + T^+ = 1.022 \text{ MeV} + T^- + T^+ \quad (5.3)$$

The kinetic energies of the electron and positron are not necessarily equal, however, their average energy is given by:

$$\overline{T} = \frac{h\nu - 2m_0c^2}{2} \quad (5.4)$$

If the quantum energy of the incident photon is well above the threshold energy  $2m_0c^2$ , the created electrons and positrons are strongly forward directed. Their average angle of the moving direction relative to the original photon direction is roughly [46]:

$$\bar{\theta} \cong \frac{m_0c^2}{\overline{T}} \quad (\text{radians}) \quad (5.5)$$

## Rayleigh (coherent) scattering

Rayleigh scattering is an interaction between a photon and an atom in a way that the photon loses none of its energy. The photon scatters and to conserve the momentum, the atom moves just slightly. The photon is usually scattered at a small angle only. The interaction is coherent as the photon is scattered by the combined action of the whole atom. Because no energy is given to any charged particle, no ionization or excitation takes place [46].

## Photo-nuclear Interaction

Photo-nuclear reaction is an interaction between an atomic nucleus and a photon. A photon with a few MeV energy enters and excites a nucleus, in result a proton ( $\nu$ , p) or a neutron ( $\nu$ , n) is emitted out [46].

## 5.2 Interaction of Charged Particles with Matter

A charged particle that moves through a medium loses energy constantly and is deflected slightly from its initial direction. These effects are due to inelastic collisions (excitation and/or ionization) with the atomic shell (electrons) and elastic collisions with the nuclei (that do not cause a loss of energy, but a variation in the direction). According to the terminology of the ICRU (International Commission on Radiation Units and Measurements), ionizing radiation can be classified into:

- **Directly Ionizing Radiation:** fast charged particles deliver their energy directly to the medium they traverse via many small Coulomb-force interactions along the particle's track [49].

- **Indirectly Ionizing Radiation:** x-rays or  $\gamma$  photons or neutrons that first transfer their energy to charged particles in the matter. The resulting fast charged particles in turn deliver the energy as directly ionizing particle. The dominant processes of indirectly ionizing radiation are Compton effect, photoelectric effect and pair production [49].

Introducing  $b$  as the classical impact parameter of a charged particle (where the Coulomb field around the charged particle can affect other particles or atoms along its path) and  $a$  as the classical atomic radius, there are three types of charged-particle Coulomb-force interactions:

### 1. Soft Collision ( $b \gg a$ )

When a charged particle passes an atom at a considerable distance, the Coulomb field of the particle affects the atom either by distorting and exciting it to a higher level of energy or ionizing it by ejecting a valence shell electron. Thus, it transfers a small amount of energy (a few eV) to an atom of the absorbing medium. This is the dominant process of the charged particle interactions as the cross-section of the vicinity of an atom is much bigger than the geometric cross-section of the atom itself (if  $b \gg a$ , then  $\sigma_b \gg \sigma_a$ ) [49].

If the velocity of the charged particle traversing a transparent dielectric material is higher than the velocity of the light in that material (see Eq. 4.1), a very small part of the energy spent by a charged particle in soft collisions can be emitted as coherent UV light called Cherenkov radiation. Cherenkov radiation is a good means for particle identification. The velocity of a charged particle can be

measured by the properties of the Cherenkov light it emits in a certain medium. If the momentum of the charged particle is determined, the mass of the particle can be computed by its momentum and velocity, and hence allows to identify the particle.

## 2. Hard Collision ( $b \sim a$ )

If  $b$  is of the order of the atomic dimensions, the interaction of the incident particle with a single atomic electron is more probable. The electron is then ejected from the atom with considerable kinetic energy and is called a delta ( $\delta$ )-ray. The  $\delta$  rays are energetic enough to undergo additional Coulomb-force interactions on their own. If an inner-shell electron is ejected from an atom by a hard collision, characteristic (fluorescence) x-rays and/or Auger electrons will be emitted [49].

## 3. Coulomb Interactions with the External Nuclear Field ( $b \ll a$ )

When  $b \ll a$ , the Coulomb interaction takes place mainly with the nucleus. This process is significant for  $e^-$  and  $e^+$ . In this case, in most of the such encounters, the electron is scattered elastically and does not emit an x-ray photon or excite the nucleus. It loses a small amount of its kinetic energy to satisfy conservation of momentum for the collision. In a small number of these incidents, in which the electron passes near the nucleus, the electron deviates from its direction, emits an x-ray photon and gives most of its energy to the photon. The x-ray photon emitted in this inelastic radiative interaction is called *bremsstrahlung* (the German word for “breaking radiation”). Bremsstrahlung production is insignificant in low- $Z$  materials for electrons below 10 MeV [49].

## Nuclear Interactions by Heavy Charged Particles

When the impact parameter of a heavy and high-energy ( $\sim 100$  MeV) charged particle is less than the nuclear radius, it may interact inelastically with the nucleus. Consequently, one or more individual nucleons are driven out of the nucleus. The highly excited nucleus emits nucleons of relatively low energy and  $\gamma$ -rays. An important process is  $\pi$  production. These particles have a mass 273 times that of the electron and interact by Coulomb forces to produce excitation and ionization along their track. They are unstable and decay into  $\mu$ , and consequently, the  $\mu$  decays to an electron [49].

## The Bethe-Bloch formula

The energy loss of a charged particle traversing a medium is given by the *Bethe-Bloch formula* (with a good approximation including relativistic effects) [50]. This equation takes into account the mean ionization potential of the medium and the maximum energy transferred to the atomic electron.

$$\frac{-dE}{dx} = 2\pi N_a m_e r_e^2 c^2 \rho \frac{Z}{A} \frac{z^2}{\beta^2} \left[ \ln \left( \frac{2m_e \gamma^2 \nu^2 E_{max}}{I^2} \right) - 2\beta^2 - \delta - 2\frac{C}{Z} \right] \quad (5.6)$$

where

$r_e = \frac{e^2}{m_e c^2} = 2.818 \cdot 10^{-13}$  cm classical electron radius;

$N_e = N_A \cdot Z \cdot \rho / A$ ;  $2\pi N_a m_e r_e^2 c^2 = 0.1535$  MeVg<sup>-1</sup>cm<sup>2</sup>;

$N_A$  = Avogadro's numbers = 0.5511 MeV/c<sup>2</sup>;

$I$  = mean ionization (excitation) potential of the target;

$Z, A$  = atomic number and atomic weight of the absorbed medium;

$\rho$  = material density;

$z$  = charged of the incident particle;

$\beta = v/c$  of the incident particle;

$\gamma = 1/\sqrt{1 - \beta^2}$ ;

$\delta$  = density effect correction (important at high energy);

$C$  = shell correction (important at low energy);

$E_{max}$  = maximum kinetic energy imparted to an electron in a single collision

$\simeq 2m_e c^2 \beta^2 \gamma^2$ , for  $M \gg m_e$ .

The *density effect* ( $\delta$ ) is larger in materials of high density (solids and liquids) than in gases. This relativistic effect implies that at high  $\beta$ , target electrons contribute in the interaction, but they are screened by electrons closer to the projectile particle trajectory. The *shell correction* takes into account the effect that occurs when the speed of the incident particle is comparable or smaller than the atomic electron orbital speed [50].

The specific energy loss depends on the velocity ( $\beta = v/c$ ) and the charge of the ionizing particle, but not on the mass of the charged particle. The specific energy loss decreases with  $1/\beta^2$  until a minimum is reached at  $\beta\gamma \approx 4$ . Particles in this region are called *Minimum Ionizing Particles* (MIP). The relativistic rise of  $dE/dx$  can reach values of 50-70% of the MIP energy loss for noble gases and only around 10% for solid materials [15].

## Transition Radiation

The features of Transition Radiation (TR) are important to design transition radiation detectors. When a charged particle passes a boundary of two homogeneous media with two different dielectric constants, an electromagnetic radiation is emitted. This phenomenon can be used to identify charged particles in the TRD. For ultra-relativistic charged particles ( $\gamma > 1000$ ), the spectrum of the emitted radiation extends into the x-ray region. In this case, the total energy loss of a charged particle is proportional to the Lorentz factor ( $\gamma = E/mc^2$ ) of the particle. According to the electrodynamic nature of the emitted radiation, the number of photons per particle is of order  $\alpha = 1/137$  in an interface between two different dielectric media. However, by using a multilayered dielectric radiator, it is possible to increase the radiation yield [51].

A charged particle traversing the boundary of two different media with dielectric constants  $\epsilon_1$  and  $\epsilon_2$  (assume  $\mu_1 = \mu_2 = 0$ ) <sup>2</sup> with constant velocity  $v$  emits TR into the forward hemisphere with an intensity of [51]:

$$\frac{d^2W}{d\omega d\Omega} = \frac{2e^2v^2\sqrt{\epsilon_2}\sin^2\theta\cos^2\theta}{\pi^2c^3(1-\beta^2\epsilon_2\cos^2\theta)} \times [((\epsilon_1 - \epsilon_2)(1 - \beta^2\epsilon_2 - \beta\sqrt{\epsilon_1 - \epsilon_2\sin^2\theta})) \times ((1 - \beta\sqrt{\epsilon_1 - \epsilon_2\sin^2\theta}) \times (\epsilon_1\cos\theta + \sqrt{\epsilon_1\epsilon_2 - \epsilon_2^2\sin^2\theta}))^{-1}]^2 \quad (5.7)$$

where  $e$  is a charge moving at a constant velocity  $v$  normal to the surface and  $d^2W/(d\omega d\Omega)$  is the energy radiated into solid angle ( $d\Omega$ ) at an angle  $\theta$  to the trajectory of the particle in a bandwidth of frequency  $d\omega$ .

The absorption length of TR photons as a function of TR energy for Ar, Kr and Xe in gaseous detectors is shown in Fig. 5.5. The Xe with highest  $Z$  has the best detection efficiency with an absorption length around 10 mm for typical TR photon energies in the range of 3 - 15 keV. The data are taken from the NIST<sup>3</sup> database [52].

---

<sup>2</sup> $\mu$ : mass absorption coefficient [ $\text{cm}^2\text{g}^{-1}$ ]

<sup>3</sup>National Institute of Standard and Technology

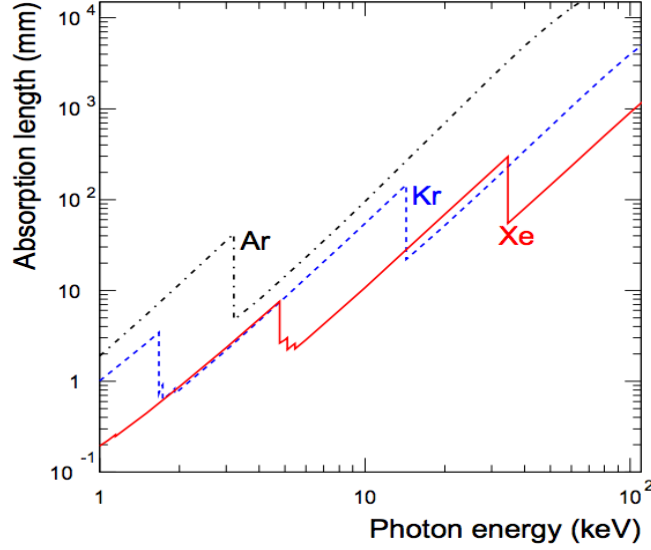


Figure 5.5: Absorption length as a function of the photon energy in argon, krypton and xenon. As shown, Xe is an optimum noble gas for absorbing the highest amount of photons in the detector [52].

### 5.3 Multi-Wire Proportional Chamber

A Multi-Wire Proportional Chamber (MWPC) in a simple form is composed of a grid of thin, parallel and equally spaced anode wires, which are symmetrically sandwiched between two cathode planes. Cathode planes can either be a conductor plane or a set of thin equally spaced wires. Depending on the application of the chamber, the gap between anode and cathode wires should be filled with an appropriate mixture of gases. By applying a High Voltage (HV), an electric field is formed between the anode and the cathode wires (see Fig. 5.6) [55]. This region is called *amplification region*.

When a fast charged particle passes the amplification region, it ionizes the gas atoms and releases electrons. The released electrons (primaries) will drift towards an anode wire. The electric field at a far distance ( $\sim 20$  times the wire-diameter) from the anode wires is basically constant. However, near the wires, it becomes inversely proportional to the  $r^2$  distance measured from the wire. Thus, the primary electrons can gain enough kinetic energy to inelastically collide with the gas molecules and produce new ionizations by generating secondary electrons. This process can continue further and result in what is called *an electron avalanche* or

*charge multiplication*. Figure 5.7 presents the process of generation of an avalanche around an anode wire. If the total collected charge is proportional to the number of primary electrons, then the chamber is said to operate in the “proportional mode”. The constant of this proportionality is called *multiplication factor*, which depends exponentially on the applied HV [55].

While the electron avalanche is collected by the anode wires rapidly ( $\sim \text{ns}$ ), the positive ions left over in the trail of multiplying electrons move into the opposite direction toward the cathode and induce image charges on surrounding electrodes that result in a negative signal on the wire where the avalanche originated (see Fig. 5.7) [55].

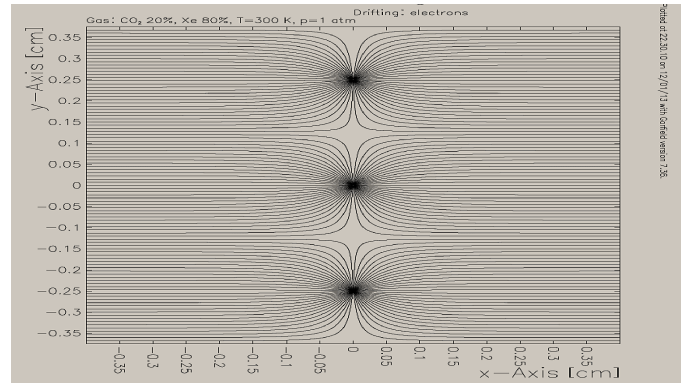


Figure 5.6: Electric field lines between anode wires and two cathode planes [68]. In the middle are three anode wires located in parallel with a pitch of 2.5 mm between them.

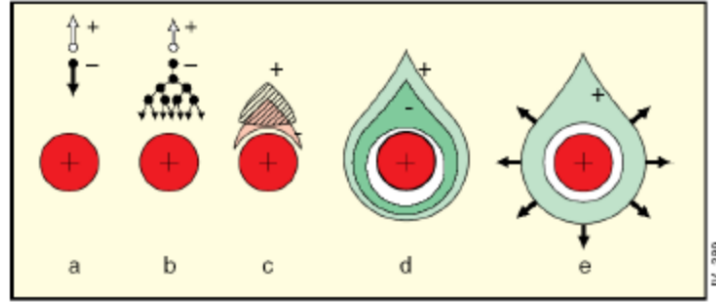


Figure 5.7: Different stages in the gas amplification process next to the anode wire[65]. An electron avalanche is generated by an electron drifting towards an anode wire. The avalanche is then rapidly ( $\sim \text{ns}$ ) collected by the anode wire.



### 5.3.1 Prototype Characteristics

The characterization of a MWPC can be done by a set of measurements i.e. gas gain, energy resolution and pad response function. In this section, we define these characteristics and explain how to measure them.

#### Gas Gain

The amount of charges arriving at one wire cell for a given ionizing event with the detector at a certain high voltage is called *gas gain*. To measure the gas gain ( $G$ ) of a MWPC, one can measure the current of the anode wires ( $I$ ) while the detector is exposed to ionizing radiation at a certain HV, and compare it with the primary current ( $I_0$ ) without applying HV [15]:

$$G = \frac{I}{I_0} \quad (5.8)$$

To compare the empirical gas gain result with the simulated one, an absolute gas gain measurement has to be performed. An absolute gas gain can be obtained by subtracting the dark current ( $I_D$ ) from the actual measured current ( $I_A = I - I_D$ ). The dark current is the current measured in the absence of an ionizing source. The primary current is defined as the charge of an electron multiplied by the rate of absorbed photons from the radioactive source ( $R$ ) multiplied by the electrons released per primary ionization ( $N_P$ ), which is determined as the ratio of the radiation energy of the utilized source ( $E_\gamma$ ) and the ionization potential of the used gas mixture ( $E_I$ ) [15]. The rate ( $R$ ) is specified as the directly counted rate with a correction factor. The absolute gas gain ( $G_A$ ) can be measured as:

$$\begin{aligned} G_A &= \frac{I_A}{I_P} = \frac{I - I_D}{e \cdot R \cdot N_P} \\ \text{with: } N_P &= \frac{E_\gamma}{E_I} \\ \text{and: } R &= \frac{R_M}{1 - R_M \cdot \tau} - R_D \end{aligned} \quad (5.9)$$

where  $R_D$  is the rate measured without source to be used for correction of background and noise,  $R_M$  is the measured ionizing radiation and  $\tau$  is the dead time

of the used electronics, which has to be taken into account for each measurement [56].

## Energy Resolution

The ability of the detector to accurately determine the energy of the incoming radiation is defined as energy resolution. This ability defines how precisely the detector can resolve two peaks that are close together in energy. This characteristic of a MWPC is important for the particle identification. To measure the energy resolution, the detector can be irradiated by a radioactive source (for instance  $^{55}\text{Fe}$ ) and the energy spectrum of the source has to be recorded. The energy resolution then will be defined by the Full Width (of the photopeak) at Half its Maximum height (FWHM). If a standard Gaussian shape is assumed for the measured spectrum, the FWHM is given by:

$$\text{FWHM} = 2\sigma\sqrt{\ln 2} \quad (5.10)$$

where  $\sigma$  is the width parameter of the Gaussian. Smaller FWHM corresponds to higher resolution.

$^{55}\text{Fe}$  is a radioactive isotope with a half-life of 2.73 years. It decays via electron capture to an excited state of Manganese. The process of electron capture leaves a hole in the  $K$ -shell which is then filled by an electron of an upper shell. Several  $K$ - and  $L$ - transitions are possible, leading to the release of the energy difference between the shells via the emission of x-rays or Auger electrons. The energy of the Auger electrons and the  $L$  transition x-rays ( $\sim 0.6$  keV) is too low to allow them to leave the source and hence they can not be detected. Therefore, only the x-rays originating from  $K$  transitions after the decay of  $^{55}\text{Fe}$  to Manganese have to be considered [57]. The x-ray energies of the different shell transitions are represented in Tab. 5.1. Table 5.2 shows the binding energies of electrons in the different shells of the argon atom.

Using Ar as the counting gas in the MWPC and an  $^{55}\text{Fe}$  source, an energy spectrum with two peaks is expected: a photopeak due to the  $k_\alpha$  x-rays (5.9 keV) and an additional peak which appears in the left part of the  $^{55}\text{Fe}$  spectrum when x-rays with energies higher than the absorption edge of argon are emitted [15, 57]. A  $^{55}\text{Fe}$  source emits photons with 5.9 keV. The  $K$ -edge of the Ar atom has a binding energy of 3.2 keV, which means the photons emitted by  $^{55}\text{Fe}$  source have enough energy to release an electron from the  $K$ -shell of an Ar atom. If a primary electron is released from its atom by the incident x-ray, the relevant gap in the

Table 5.1: The energies of different  $K$  and  $L$  transition. The energy transition takes place to fill the gap in the  $K$  shell of the Manganese atom after  $^{55}\text{Fe}$  decayed to Manganese through an electron capture process [57].

Transition	X-ray energy
$K_{\alpha 1}$	5.90 keV
$K_{\alpha 2}$	5.88 keV
$K_{\beta}$	6.49 keV
$L1$	0.55 keV
$L_{\alpha 1/2}$	0.63 keV

Table 5.2: The binding energies of the electrons – given in keV – in the different shells of the argon atom [57].

Shell	$K$	$L_1$	$L_2$	$L_3$	$M_1$	$M_2$	$M_3$
Binding energy	3.2	0.326	0.25	0.248	0.029	0.016	0.015

$K$ -shell will be filled by an electron from an upper shell. After this transition, the energy is either released via Auger electrons or a photon. Events where this photon escapes the detector appear in the escapepeak, peaking at a mean energy of  $\sim 2.99$  keV deposited in the detector.

The result of a laboratory measurement of a  $^{55}\text{Fe}$  source spectrum is shown in Chap. 6.

## Pad Response Function

The inner cathode plane of a TRD is subdivided into rows, each consisting of several separate pads. The distribution of a generated cluster charge and its spread over the read out pads in the back of the detector is called Pad Response Function (PRF). It is plotted as the signal height of a given pad versus its reconstructed position with respect to the pad with the maximum signal [59]. To collimate the  $^{55}\text{Fe}$  source exactly in the middle of a specific pad, one can measure the signals from two or more neighboring pads and compare them. Figure 5.8 presents the spread of a cluster charge (red area) on two neighbor pads and its true (red vertical line) and reconstructed (green vertical line) position.

The PRF can be calculated by the empirical Mathieson formula for the induced charge distribution  $\rho(y)$  on the cathode pad plane which describes this

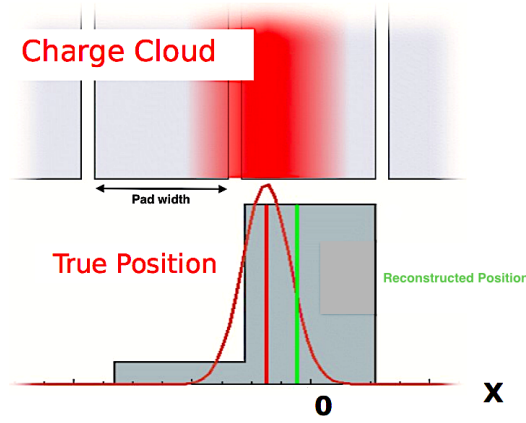


Figure 5.8: Distribution of a cluster charge on two neighboring pads and its true (red line) and reconstructed (green line) position [58].

phenomenon in a symmetric MWPC <sup>4</sup>. Therefore, the PRF is obtained by integration of  $\rho(y)$  over the width of the pad ( $W$ ) [59, 60]. For  $y = d/h$ , we have:

$$PRF(y) = \int_{y-W/2}^{y+W/2} \rho(y') dy' \quad (5.11)$$

where  $h$  is the distance between the anode wire plane and cathode plane, and  $d$  is the track position relative to the center of the pad with maximum charge. By calculating the integral in Eq.5.11, one gets [59]:

$$PRF(d/h) = - \frac{\arctan(\sqrt{K_3} \tanh(\pi(\sqrt{K_3} - 2) \cdot \frac{W-2 \cdot d}{8h}))}{2 \arctan(\sqrt{K_3})} - \frac{\arctan(\sqrt{K_3} \tanh(\pi(\sqrt{K_3} - 2) \cdot \frac{W+2 \cdot d}{8h}))}{2 \arctan(\sqrt{K_3})}. \quad (5.12)$$

where  $K_3$  is a function of characteristic chamber parameters such as the anode wire radius  $r_a$ , the distance between the anode and the cathode  $h$ , and the anode wire pitch  $s$ . The Mathieson formula in Eq. 5.12 is symmetric with respect to  $d = 0$  [59]. Figure 5.9 shows the values of  $K_3$  for empirical distributions in different chamber geometrical parameters, parallel (left) and normal (right) to the anode wire direction [62]. Before performing a PRF measurement, some primary processes such as noise correction, baseline correction and cluster reconstruction

<sup>4</sup>A symmetric MWPC consists of a plane of anode wires centered between two planar cathodes.

have to be carried out. A pad response function analysis of a TRD prototype is discussed in Chap. 9.

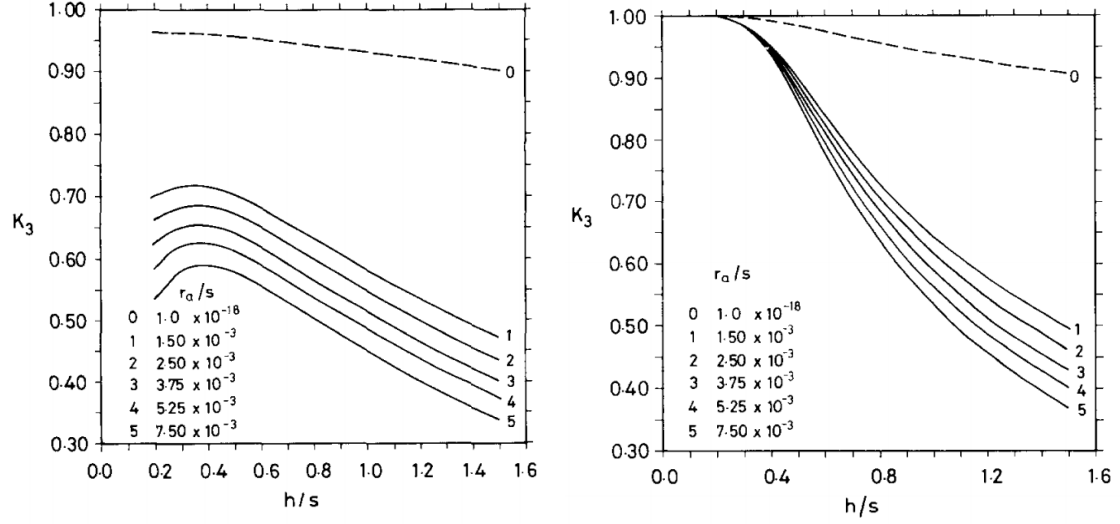


Figure 5.9: Values of  $K_3$  as a function of chamber geometrical parameters ( $h/s$  and  $r_a/s$ ) for an empirical distribution  $\rho(y)$ , parallel to anode wire direction (left), and normal to anode wire direction (right) [62].

## Track Position

To determine the position  $d$  of a track, a charge fraction on the pad ( $i$ ) with maximum charge and also on two left and right hand neighbor pads ( $i - 1$  and  $i + 1$ ) has to be measured. The PRF measured by the charge sharing between adjacent pads can be used to determine the position of a track on the pads. For this reason, the charge fraction on each pad can be specified in terms of values of the PRF as [59]:

$$\frac{Q_i}{Q_{i-1} + Q_i + Q_{i+1}} = A \cdot \exp\left(-\frac{d^2}{2\sigma^2}\right) \quad (5.13)$$

$$\frac{Q_{i-1}}{Q_{i-1} + Q_i + Q_{i+1}} = A \cdot \exp\left(-\frac{(d+W)^2}{2\sigma^2}\right) \quad (5.14)$$

$$\frac{Q_{i+1}}{Q_{i-1} + Q_i + Q_{i+1}} = A \cdot \exp\left(-\frac{(d-W)^2}{2\sigma^2}\right) \quad (5.15)$$

where  $A$  is the pad aspect ratio,  $W$  is the pad width,  $\sigma$  is the variance of the Gaussian fitted to the PRF and  $Q_i$ ,  $Q_{i-1}$ ,  $Q_{i+1}$  are the charges on the central, left and right hand pads, respectively. To derive  $d$  from the three above equations, one can divide Eq. 5.13 by Eq. 5.14 and Eq. 5.14 by Eq. 5.15 and get two equations (A and B). By dividing A by B and B by A, Eq. 5.16 and Eq. 5.17 are obtained [59]:

$$\frac{Q_{i+1}}{Q_{i-1}} = \exp\left(\frac{2dW^2}{2\sigma^2}\right) \quad (5.16)$$

$$\frac{Q_i^2}{Q_{i-1} \cdot Q_{i+1}} = \exp\left(\frac{W^2}{\sigma^2}\right) \quad (5.17)$$

By solving for  $d$ , the result is:

$$d = \frac{W}{2} \cdot \frac{\ln\left(\frac{Q_{i+1}}{Q_{i-1}}\right)}{\ln\left(\frac{Q_i^2}{Q_{i-1} \cdot Q_{i+1}}\right)} \quad (5.18)$$

## Cluster Reconstruction

The displacement  $dis_y$  of the hit from the center of pad  $i$  (pad with maximum charge) can be measured using neighboring pads ( $i - 1$  and  $i + 1$ ). Applying an average weighted method with weights  $w_1$  and  $w_2$  [63]:

$$dis_y = \frac{1}{w_1 + w_2} \left[ w_1 \left( -\frac{W}{2} + \frac{\sigma^2}{W} \cdot \ln \frac{Q_i}{Q_{i-1}} \right) + w_2 \left( \frac{W}{2} + \frac{\sigma^2}{W} \cdot \ln \frac{Q_{i+1}}{Q_i} \right) \right] \quad (5.19)$$

where  $W$  is the pad width,  $\sigma$  is the variance of the Gaussian fitted to the PRF. Since the error of the measurement is roughly proportional to the inverse recorded pulses on the side pads, one can consider  $w_1 = Q_{i-1}^2$  and  $w_2 = Q_{i+1}^2$ , with  $Q_i$  being the charge on pad  $i$ . The cluster position can be reconstructed with the knowledge of the displacement [63].

## Position Resolution

The distance between the position of the reconstructed  $y_{rec}$  and the true  $y_{fit}$  value (see Fig. 5.8) of the cluster position can be considered as residual  $\Delta_y$  for a given track [63] :

$$\Delta_y = y_{rec} - y_{fit} \quad (5.20)$$

For a large number of tracks, the position resolution of two detectors  $\sigma_y$  can be determined by the variance of a Gaussian fitted to the distribution of residuals  $\Delta_y$ . There is no need for external tracking devices to determine the position by using this method. As long as two TRD prototypes are identical in construction, the position resolution  $\lambda$  of a single prototype is given by [63]:

$$\lambda = \sigma_y / \sqrt{2} \quad (5.21)$$

Figure 5.10 shows a sample of measured PRF fitted by the Mathieson formula (a) and a Gaussian curve (b). A typical distribution of residuals for moderate particle rates is illustrated in Fig. 5.11.

## Particle Identification

The most appealing features of TR, for highly relativistic particles, are its dependence on the Lorentz factor  $\gamma$  and the radiation emission in the x-ray region, which are important in experimental high-energy physics for particle identification. A transition radiation detector provides particle identification and  $e/\pi$  separation [64]. Several methods can be used to perform this task such as truncated mean signal, one- or two dimensional (logarithmic) likelihood, and neural network.

The combined signal resulting from specific ionization and the absorption of transition radiation is called truncated mean signal. After truncating the signals by removing a certain fraction of highest values, in order to reduce Landau fluctuations, truncated signal was plotted. Figure 5.12 shows the truncated mean signal

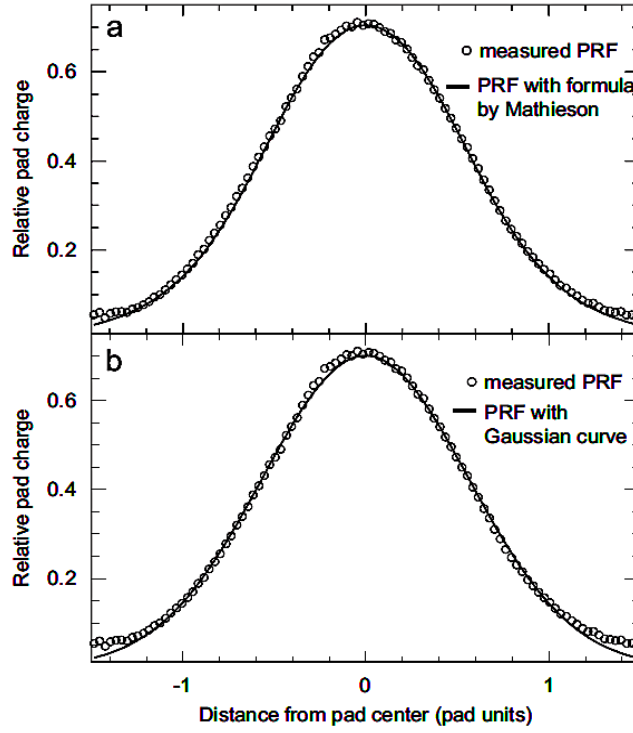


Figure 5.10: An example of a PRF. The circles show the measured PRF. The fitted curve line indicates a PRF calculated using the Mathieson formula (a), and an approximated Gaussian fit (b) [63].

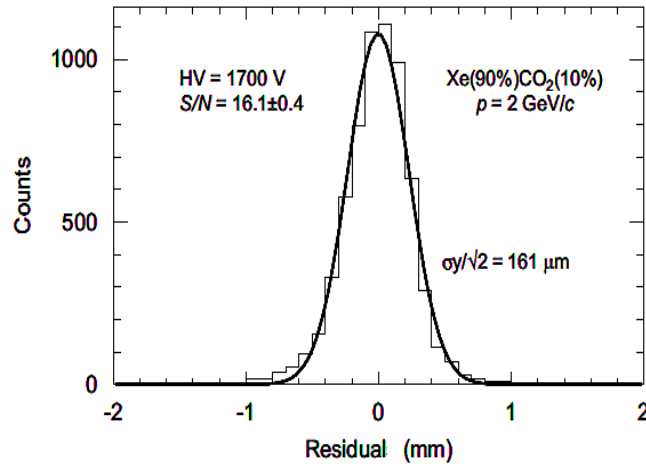


Figure 5.11: An example of the distribution of residual with a Gaussian fit [63].



versus momentum in p-Pb collisions at  $\sqrt{s} = 5.02$  TeV for the ALICE-TRD. This method allows identification of light nuclei and hadrons [64].

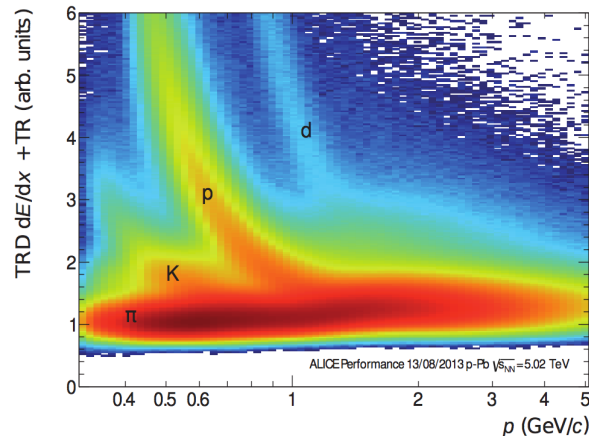


Figure 5.12: Truncated mean signals as a function of momentum for charged particles in minimum bias data from p-Pb collisions at  $\sqrt{s} = 5.02$  TeV [64].

## Likelihood

The likelihood methods are often used to identify the particle identity of reconstructed tracks. The spectra of the deposited charge can be used as an input to construct the one-dimensional likelihood. Figure 5.13 (left) presents a simulation of the spectra of the deposited energy of pions and electrons in a Xe-based detector. It shows the energy loss of pions in the gas, and the sum of the ionization energy loss and the signal produced by the absorption of the TR photons for electrons. As the energy loss spectrum of pions has a long tail, the detector system needs to be built of several layers of TRD [53].

If a full charge signal is obtained, the  $e/\pi$  separation is preferably done by a likelihood method from the measured spectra of identified particles. Assuming these spectra after normalization to unity in each layer as probability distributions for electrons ( $P(E_i | e)$ ) and pions ( $P(E_i | \pi)$ ) to produce a signal of magnitude  $E_i$ , the likelihood to be an electron ( $L_e$ ) and the likelihood to be a pion ( $L_\pi$ ) are [54]:

$$L_e = \frac{P_e}{P_e + P_\pi}, \quad L_\pi = \frac{P_\pi}{P_e + P_\pi} \quad (5.22)$$

$$\text{with} \quad P_e = \prod_{i=1}^N P(E_i | e), \quad P_\pi = \prod_{i=1}^N P(E_i | \pi) \quad (5.23)$$

where the sum runs over the number of detector layers.

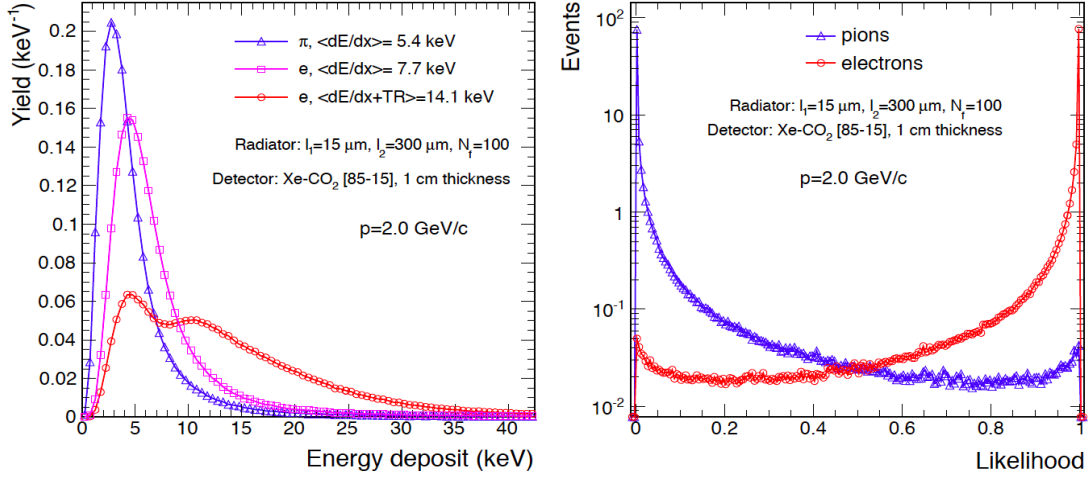


Figure 5.13: Simulation of the total energy deposition of pions and electrons in one layer of a TRD (left), and electron likelihood distributions constructed from them using six layers of TRD (right) [53].

The likelihood shown on the right side of Fig. 5.13 is derived from the integrated charge signal for pions and electrons. The electron identification performance of a TRD is the fraction of pions wrongly identified as electrons.

In the logarithmic likelihood, the range of possible values is  $[-\infty, \infty]$ , which allows for a wider separation of the likelihood values while using the same input spectra as the classic (one dimension) method. The logarithmic likelihood for electron and pion can be calculated as [15]:

$$L_e = \log \frac{P_e}{P_\pi}, \quad L_\pi = \log \frac{P_\pi}{P_e} \quad (5.24)$$

## 5.4 Principle of Operation of a TRD

A sketch of the TRD working principle is shown in Fig. 5.14. The TRD is composed of two general parts: the Read-Out Chamber (ROC) and the radiator. The design of the CBM-TRD, as it is foreseen for the experimental setups of CBM at the SIS100, will be based on a Multi-Wire Proportional Chamber (MWPC) with an amplification region of  $3.5 + 3.5$  mm thickness, combined with a thin drift region of 5 mm thickness. These two regions are separated by a cathode wire plane.

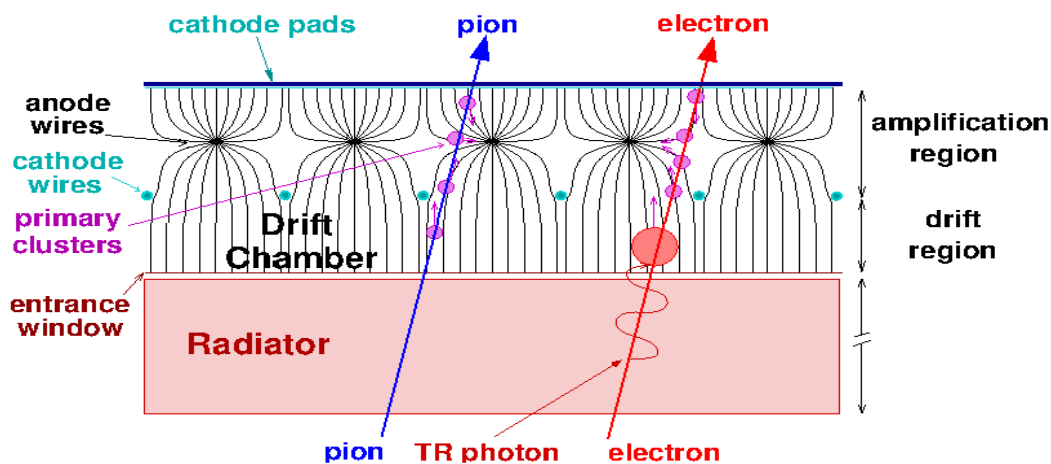


Figure 5.14: A sketch of the working principle of the CBM-TRD. It shows a projection in the plane perpendicular to the wires. Electrons produced by ionization energy loss ( $dE/dx$ ) and by TR absorption drift along the field lines towards the anode wires [68].

In the momentum range from 1 to 10 GeV/ $c$ , only electrons produce TR. When an electron passes through the radiator and ROC, it generates TR and ionizes the gas atoms. Pions also ionize the gas atoms and generate electrons. Both the ionization electrons and those from the absorption of the TR photons drift along the anode wires due to the electric field in the amplification region and create avalanches which induce a signal on the cathode pad [68].

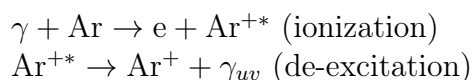
The probability of TR production is about 1% per boundary crossing, thus several hundred radiator interfaces are required for practical TR detectors. Taking into account absorption inside the radiator itself, a radiator of about 100 foils produces about one net TR photon with energies in the useful range of soft X-rays (1 – 30 keV) [66].

A radiator is mounted in front of the ROC entrance window. The entrance window is defined by a thin aluminized Kapton/Mylar foil, which also serves as cathode for the drift field. The ionized gas starts an ionization avalanche in the proximity of parallel thin wires at high voltage. This abrupt current change induces a fast electric signal that can be collected on the pad plane which is mounted on the back panel of the ROC. To reconstruct the position of the ionization processes, the pad plane is segmented. The differences in energy loss ( $dE/dx$ ) provide the possibility to separate and identify the nuclear fragments.

## 5.5 Choice of Gas for the TRD

In order to achieve an efficient electron identification by a TRD with a limited thickness, a short absorption-length (for the TR-photons) gas should be used. Nobel gases are used as they are not electronegative (i.e. they do not combine with electrons) and do not react chemically with the detector components. They (Ar, Kr and Xe) can be dense (high  $Z$  materials), so that the energy loss of charged particles and the TR absorption rate are high. Argon is the most widely used counting gas, due to its low cost. However, to reach an efficient electron identification, xenon with an absorption length of 10 mm (for a typical TR-photon energy of 10 keV) is an optimum noble gas (compared to Ar and Kr), since it provides a higher sensitivity to TR-photons (see Fig. 5.5).

An avalanche can generate additional avalanches through photons created during the amplification process. The wavelength of these photons is in and around the ultraviolet region of the spectrum. The process of emission of these ultraviolet photons is de-excitation of the gas atoms. For instance, if argon is used, we see the following processes [67]:



where  $\gamma$  in the first reaction represents any ionizing radiation and  $\gamma_{uv}$  in the de-excitation process represents the ultraviolet photon emitted by an excited argon ion atom. The minimum energy of these  $\gamma_{uv}$  is higher than the ionization potential of the metals commonly used in the MWPCs. If a  $\gamma_{uv}$  strikes the cathode wall, it might knock off an electron from the metal. This electron would be accelerated due to the high electric field inside the amplification region. Eventually, it may approach the anode and cause another avalanche and lead to non-linearities in the response of the MWPC. One solution to this problem is to add an agent in the gas which has a high absorption coefficient for the photons in the ultraviolet region.

The process of decreasing the probability of secondary charges is called *quenching* and the agent used for this purpose is called *quencher* [67]. For TRD at SIS100 xenon as the ionizing gas and CO<sub>2</sub> as the quencher gas, with the mixture ratio of 85% Xe to 15% CO<sub>2</sub>, is foreseen.

## 5.6 Radiator

The main purpose of the radiator is TR production. The radiator can also provide mechanical stability for the entrance window and can thus reduce the bulging of the entrance window, which can occur due to changes in pressure. The radiator can be classified as regular and irregular according to their different types of boundaries and geometries. The regular radiators are mostly made of equally spaced foils and produce a relatively large number of photons per incident electron. The irregular radiators are made of foams or fiber mats in which the mean number of produced photons is lower - compared to regular radiators - due to the missing coherent interference and/or the irregular structure size in foams or fiber mats. The intensity and the energy of the produced TR affects the efficiency of electron-pion separation. The choice and structure of the radiator determine both quantities of the TR.

To optimize the TR-yield, it is important to understand the influence of radiator parameters like material, foil, number of foils and gap thickness. The optimization parameters of a radiator are strongly related to the detector characteristics. If the photon absorption probability spectrum (see Fig. 5.15) and the TR-photon production spectrum are well matched, it leads to an optimal PID performance of the entire detector system. The foil and the gap thickness of the radiator influence the shape of the TR-spectrum. The total TR-yield can be improved by increasing the number of foils. The material properties of the radiator e.g. plasma frequency, conductivity and cross-section are important for the optimization [68].

### Radiator Options

By taking into account three criteria (performance, mechanical stability and cost efficiency) three types of radiator are chosen as possible options (see Fig. 5.16):

1. PolyEthylene (PE) foam-foil (irregular) radiator (type H: 125 × 2.0 mm layers) with a radiation length of 1.39 – 1.75% and a total weight of 334 g.
2. PolyPropylene (PP) fiber radiator G30 (made of 30 fiber fleece layers) with a

radiation length of  $1.70 - 1.96\%$ . The distribution of the fiber diameters is uniform, but their spacing is completely chaotic. Its high performance is mostly due to the pure amount of interfaces between fibers and gas per unit volume.

3. POKALON radiator (K++) is a micro-structured self-supporting radiator. It is a combination of the advantages of a regular radiator with the mechanical stability of an irregular radiator. It is frame-less and made from 350 foil layers with a low weight of 176 g in total and has a higher radiation length ( $3.09\%$ ), due to its oxygen content. However, its high price makes it uneconomical [68].

According to radiator performance studies, the most efficient radiator is a regular radiator made of Polyethylene foil, because of its high regularity and high yield due to its interference. Study also showed the Münster 2012 prototype equipped with this kind of radiator has a better pion efficiency at 90% electron efficiency. However, such a radiator can not be an option for the CBM experiment, since the foil support frames would increase the material budget of the TRD and it is difficult to construct and, therefore, expensive. Among three mentioned optional choices, the PP-fibers and the POKALON foils are not considered because of their high material price. Thus, the radiator type H is left as the preferred option [68].

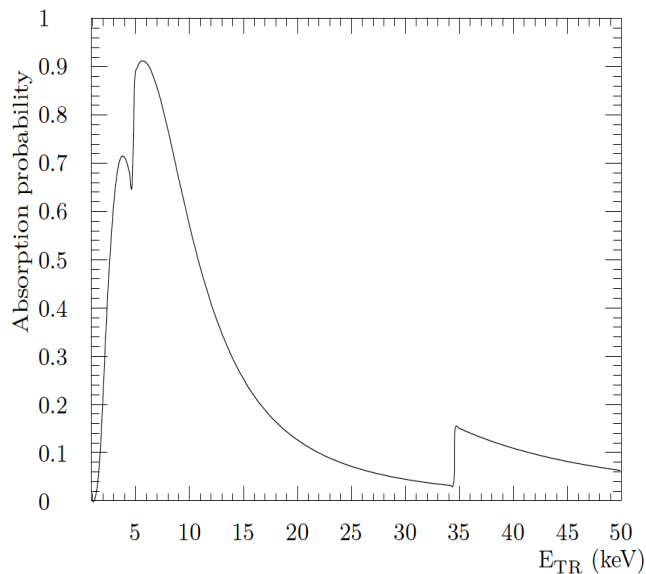


Figure 5.15: A simulation of the absorbed photon spectrum of the 2012 Münster prototypes as seen by one readout chamber [68].

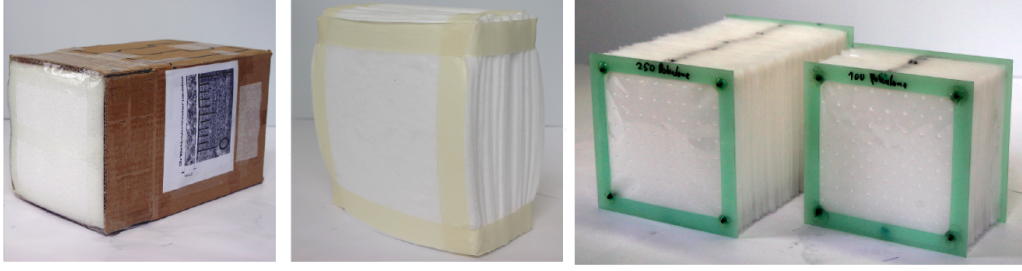


Figure 5.16: **Left:** PE foam-foils radiator (type H:  $125 \times 2.0$  mm). **(center):** fiber-fleece layers,  $30 \times 4$  mm PP LRP 375 BK (type G30). **right:** type K, self-supporting micro-structured POKALON N470 foil radiator. [68].

## 5.7 Readout Chamber Design

For the SIS100 one station of four layers of the TRD is planned (see Fig. 5.17 and Fig. 5.18). This setup can be extended to ten layers for the possible use of the TRD at SIS300 (see Fig. 5.19). TRD modules are built in only two different sizes for both the SIS100 and the SIS300. The small modules (types 1, 2 and 3) are designed for the inner areas of each layer and have outer dimensions of  $57 \times 57$  cm<sup>2</sup>. The large modules (types 6, 7 and 8) will be covering the outer areas of each layer with the outer dimensions of  $95 \times 95$  cm<sup>2</sup>.

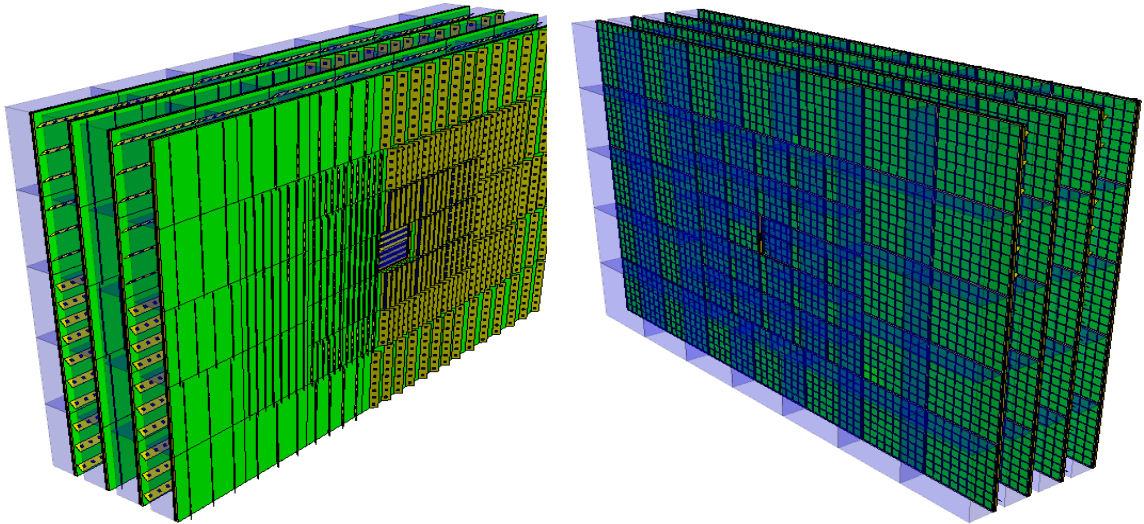


Figure 5.17: CBM-TRD geometry of the station of four layers for SIS100. The front view (right) shows the ROCs with the radiator boxes. The rear view (left) displays the backpanels of the ROCs together with the front-end electronics [68].

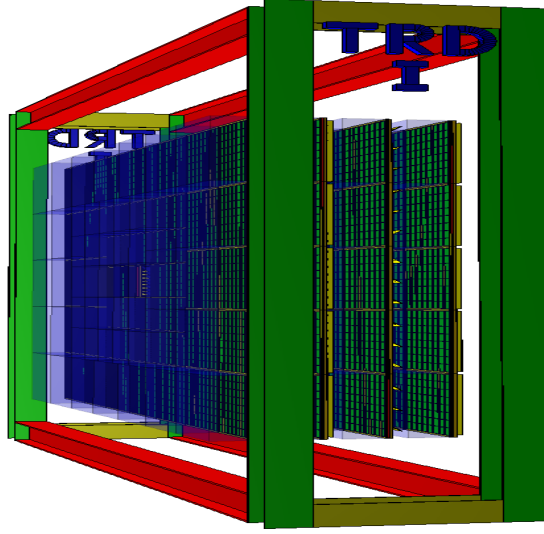


Figure 5.18: One station with four layers of the TRD proposed as the SIS100 CBM-TRD geometry. The small modules are designed for the inner part of each layer and the large modules will be placed in outer part of each layer [68].

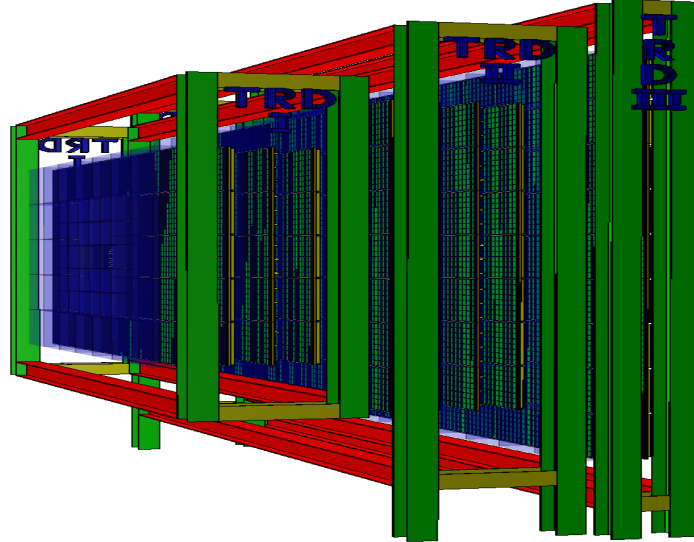


Figure 5.19: Three stations with ten layers in total of the TRD proposed as the SIS300 CBM-TRD geometry [68].

A MWPC with drift region is considered as the default solution for the ROCs of the CBM-TRD at SIS100 and SIS300. The prototypes with drift region have



the advantage of a higher TR absorption probability and a higher gain stability of the ROC under external pressure variations. However, prototypes without drift region are faster in their signal collection time, and are considered as a possible alternative for CBM-TRD ROCs. Figure 5.20 illustrates the cross-section of the outer part of a CBM-TRD ROC with drift region and corresponding dimensions. Figure 5.21 shows the structure of a TRD prototype with its components [68].

A TRD module is composed of entrance window (frame, carbon-lattice structure and foil), electric contact for the foil, distance ledge, cathode wire grid-plane, anode wire grid-plane, pad plane, back panel (honeycomb structure, carbon plane and aluminum frame), gas-feed through and HV-LV connectors. A radiator will be amounted in front of the entrance window and front-end electronic boards will be connected to the pad plane at the back of the module.

## Entrance Window

A carbon lattice support structure is glued to the entrance window (in Münster prototypes) to avoid a deformation of the Kapton foil due to over- or under-pressures inside the detector volume, especially for large modules (see Fig. 5.22).

The entrance window is made of aluminized Mylar foil with thickness of 20  $\mu\text{m}$  (in Frankfurt prototypes) or aluminized Kapton foil with a thickness of 25  $\mu\text{m}$  (in Münster prototypes) which is aluminized only on one side. The thickness of the aluminum coating is 0.05  $\mu\text{m}$ . The foil is stretched out using the thermal expansion of a Plexiglas frame, PMMA (PolyMethylMethAcrylate), when increasing the temperature from 20° C to 50° C. The foil is prepositioned using Kapton adhesive tape and fixed on the frame by 52 screws. The device which is used for stretching the foil consists of an aluminum frame attached to the foil and is shown in Fig 5.23. The aluminum frame can be heated by electrical heating elements to a well defined temperature up to 65° C (the lower temperature limit for PMMA deflection). The Kapton foil expands about  $0.04 \pm 0.01$  cm [68].

The Kapton or Mylar foil will then be glued to the chamber body to enclose the gas volume. As the entrance window also serves as the drift potential plane, a part of the Kapton/Mylar foil is crimped over a copper strip covered on both sides with silver glue to provide the electrical connection. The drift HV cable is then soldered to this copper strip after hardening. To isolate electrically the copper strip from the outside, it will be covered by a Kapton adhesive tape.

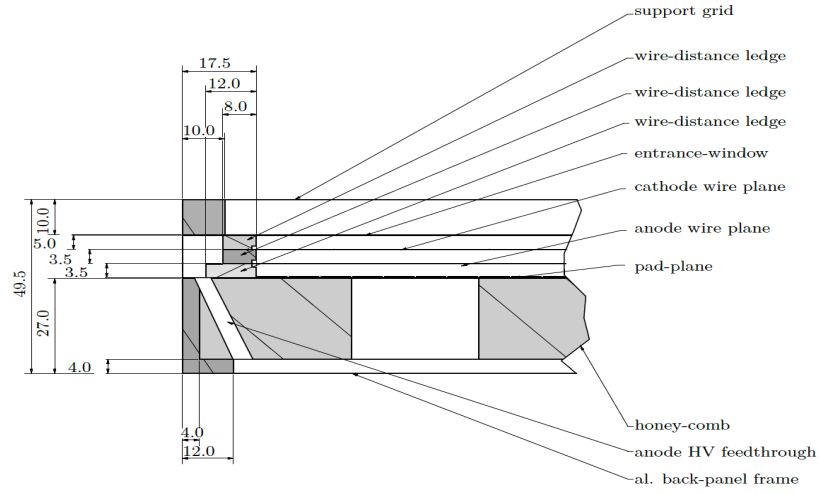


Figure 5.20: Cross section of the outer part of a CBM-TRD ROC with drift region including the corresponding dimensions and positions. All lengths are in millimeter [68].

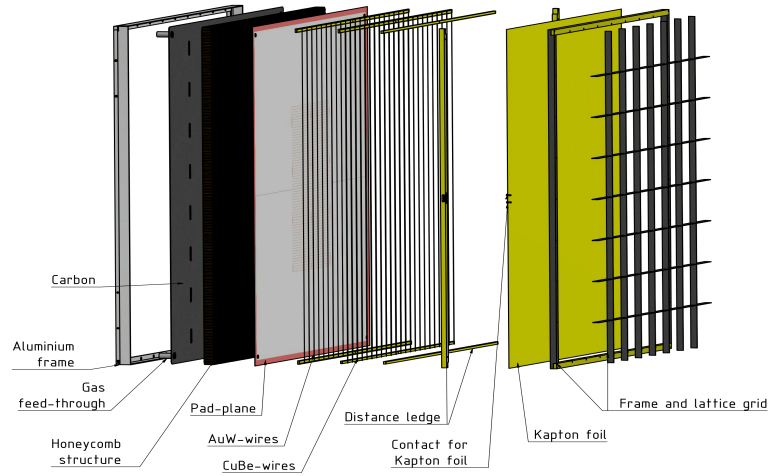


Figure 5.21: The structure of a TRD chamber with its components. This structure is applied to both small ( $57 \times 57 \text{ cm}^2$ ) and large ( $95 \times 95 \text{ cm}^2$ ) modules. The entrance window shown in the figure is an aluminized Kapton foil (Münster prototypes). In the Frankfurt prototypes, an aluminized Mylar foil is used as the entrance window without a lattice grid [68].

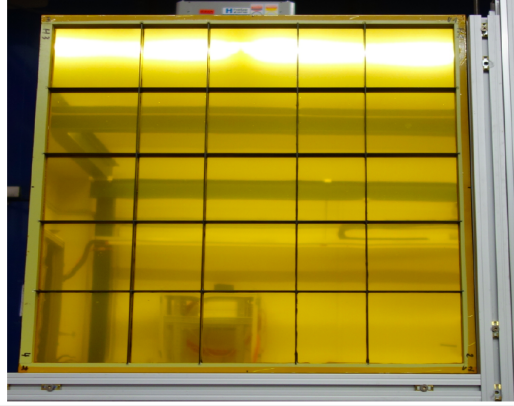


Figure 5.22: Aluminized Kapton foil supported with a carbon lattice window structure [68].

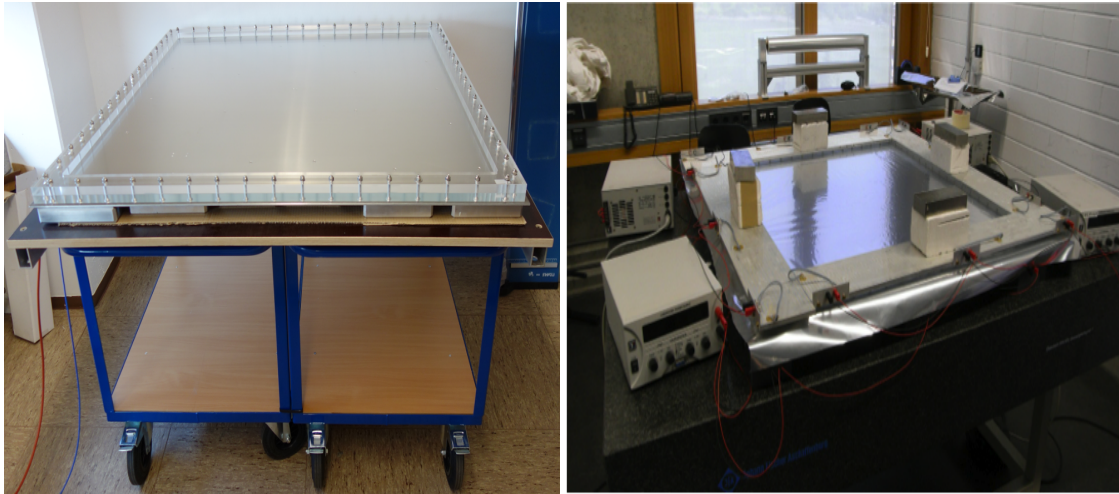


Figure 5.23: **Left:** A PMMA stretching frame on an aluminium heating plate for a foil with dimension of  $1 \text{ m}^2$  located in the Institute für KernPhysik (IKP) in Münster. **Right:** The frame with heating coils and power supplies to prepare the cathode foil for the entrance window at a well defined tension for the prototypes smaller than large ones ( $1 \text{ m}^2$ ) in the Institute für Kernphysik in Frankfurt (IKF).

## Wire Grid Planes

An amplification region thickness of  $3.5 + 3.5$  mm allows for keeping the size of the induced charge clusters small, which is of high importance in experiments with a high occupancy environment like CBM. The anode and cathode wire planes are placed at 3.5 mm distance from each other between the pad plane and the entrance window. The distance between the cathode wire plane and the entrance window is 5 mm which defines the thickness of the drift region. The distance between anode wire plane and pad plane is 3.5 mm which results in a  $3.5 + 3.5$  mm amplification region. The anode (sense) wires are made of gold-plated tungsten (Au-W) with a diameter of  $20\text{ }\mu\text{m}$ . The cathode (field) wires are made of Cu-Be with a diameter of  $75\text{ }\mu\text{m}$ . The pitch between two wires are 2.5 mm. A sectioned view of the anode and cathode wire-grid position relative to the pad plane and the entrance window is shown in Fig. 5.24.

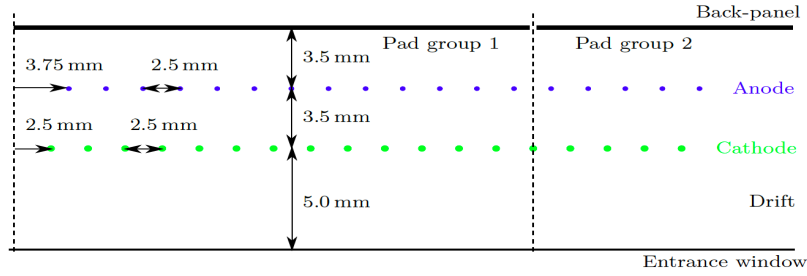


Figure 5.24: Sketch of the anode-cathode wire grid position relative to the pad plane and the entrance window. The pitch between the wires is 2.5 mm. A total gas volume length of  $3.5+3.5+5$  mm and an amplification region thickness of  $3.5+3.5$  mm are presented. The gas volume is enclosed by the back panel (pad plane and honeycomb carbon fiber structure) on the back side and by the entrance window from the front side of the chamber [68].

## Back Panel

The incident radiation produces charged particles inside the active area of the TRD. The charged particles then induce a signal on the segmented pad plane where it can be amplified and collected by the Front-End Boards (FEBs) which will be mounted on the outer side of the back panel. Pad planes face the chamber interior and enclose the gas volume of the TRD chamber from the back side. There are six different rectangular pad plane types designed for the small and large sized TRD modules where three of them are considered for the small modules and the other three for the large prototypes (see Fig. 5.25) [68].

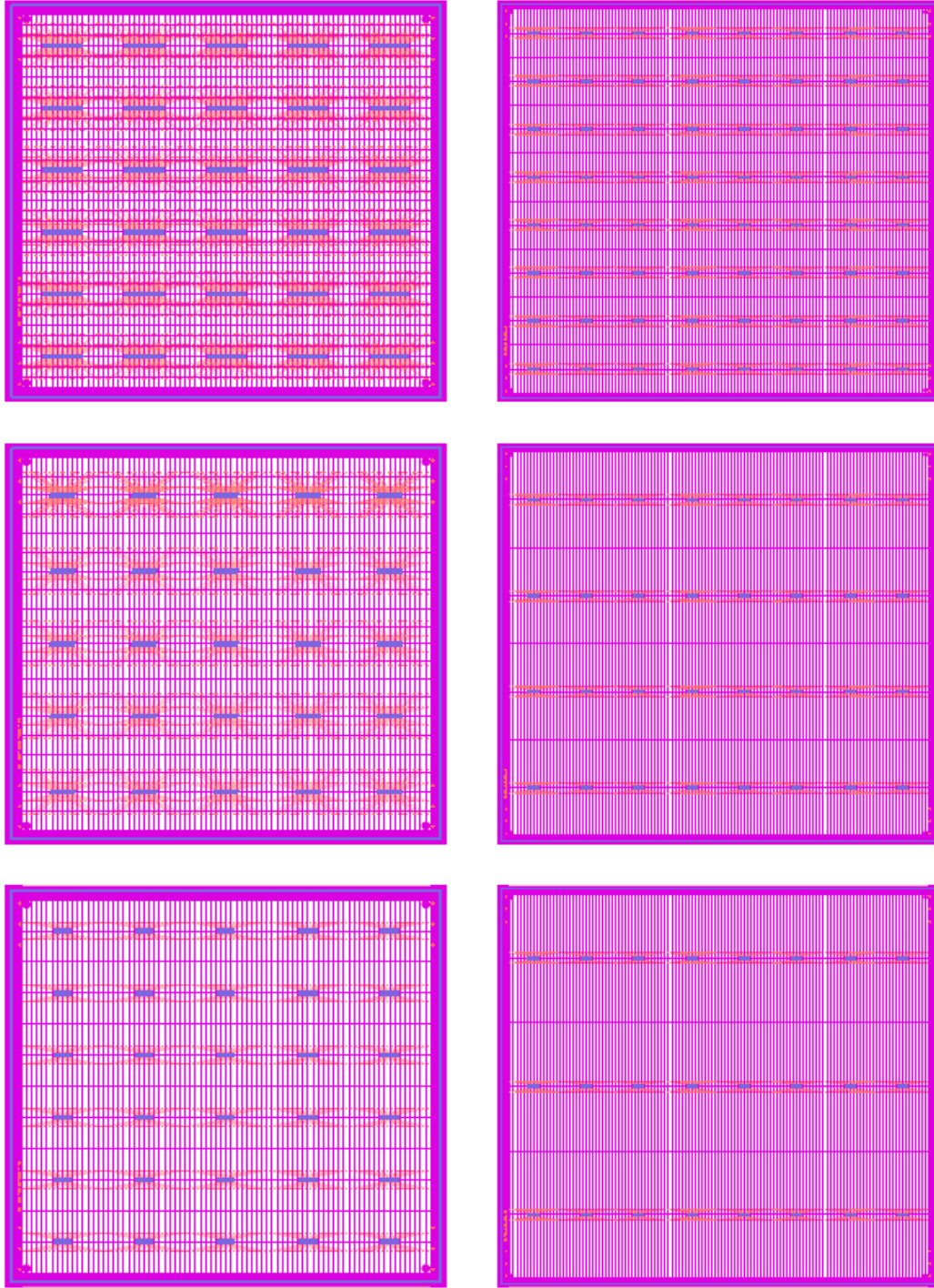


Figure 5.25: The layout of pad planes for all TRD modules. The pad planes on the left panel are for the small modules (type 1, 2 and 3 from top to bottom, respectively) in the inner areas of each TRD layer, and the pad planes on the right panel are for the large TRD prototypes (type 6, 7 and 8 from top to bottom, respectively) suited for the outer part of each layer [68].

As the hit rate in the inner areas of each TRD layer is higher than in the outer parts, a higher granularity is realized by a small pad size for the inner part of each layer. Therefore, the pad planes with the smaller pad size are considered for the small modules in the inner areas and pad planes with larger pad size are foreseen for the large modules in the outer parts of each layer of the TRD. The pad planes can be manufactured as a single Printed Circuit Board (PCB) for the small modules, while for the large modules the pad plane is constructed from two or more PCBs as they cannot be produced in large size. To avoid complications in routing the connectors to the pads, the lengths of the traces leading from the pads to the connectors have to be short. For this reason, pads in two, four or six different pad rows are grouped onto a single connector. Three different pad configurations are foreseen in order to achieve the necessary channel integration for the different pad sizes (see Fig. 5.26) [68].

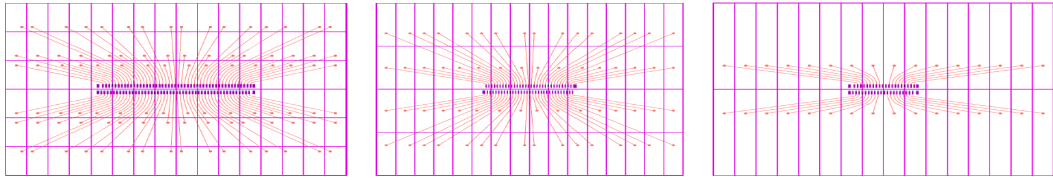


Figure 5.26: Layout of the different pad groups with different pad sizes designed for the six pad plane types of the TRD. **Left:** The high granularity pad plane grouped into 96 channel footprints which consists of 6 rows of 16 pads (ultimate density). **Middle:** The super density pads are grouped into 64 channel footprints which consists of 4 rows of 16 pads. **Right:** The 32 channel footprints pad groups with 2 rows of 16 pads [68].

The so-called ultimate density pad groups has 96 pads consist of 16 pads in each of its six rows (left panel in Fig. 5.26). However, this pad is not considered any more for the TRD purposes due to its complication of construction. The super density pad groups has 64 pads formed of four pad rows of 16 pads (middle panel in Fig. 5.26). The regular density is composed of 32 pads in two rows of 16 pads (right panel on Fig. 5.26). This configuration of pads leads to a 32- or 64-channel group connector. The TRD modules will be rotated  $90^\circ$  between each detector layer in order to attain a good position resolution in both  $x$ - and  $y$ -direction [68].

The gas volume is enclosed by the pad plane on the back side of the chamber. The pad plane is glued to a 23 mm thick honeycomb carbon fiber structure enclosed by an aluminum frame to provide higher mechanical stability. All supplies to a TRD chamber, including gas feed-through, HV and LV supply, are embedded in the backside of the detector to maximize the acceptance of each detector plane.

## Front-End Boards (FEBs)

The FEBs are designed according to the different channel density on each pad plane. For a group of 32 channels, one ASIC is foreseen. Two ASICs can be grouped in the case of 64 channel connectors. For the TRD module types 1, 2 and 3 (all small prototypes) three kinds of FEBs with 5, 10 and 15 ASICs are planned. For all large prototypes (types 6, 7 and 8), one FEB type with 8 ASICs is assumed. The FEBs for module types 1, 2 and 3 have 160, 320 and 480 channels, respectively. The FEB designed for the large prototypes has 256 channels. Figure 5.27 shows the different FEBs corresponding to the small and large TRD modules [68].

The FEBs will be mounted to the back panel. Figure 5.28 depicts different TRD modules with their corresponding FEB designs. To reduce the FEB and material budget and to conform the FEB with the Read Out Boards (ROB), FEBs with  $5 \times 3$  and  $5 \times 1$  ASICs are replaced by FEBs with  $7 \times 1$  and  $8 \times 1$  ASICs (see Sect. 6.4) for TRD at SIS100.

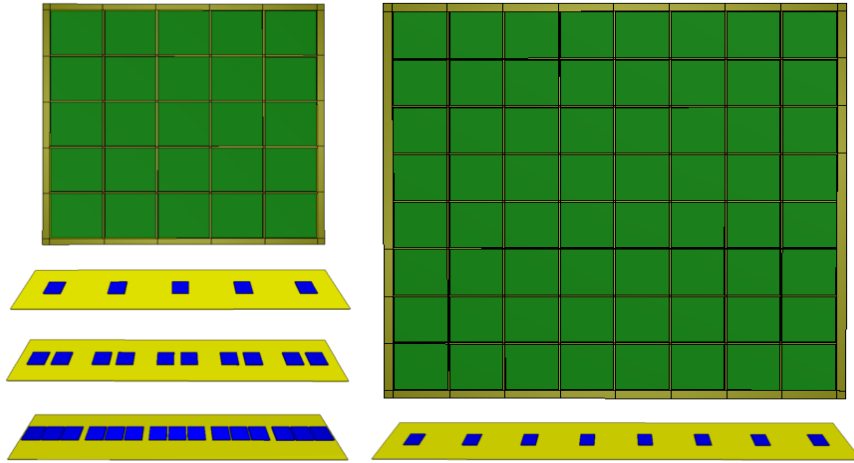


Figure 5.27: The three types of FEB ( $5 \times 32$ ,  $10 \times 32$  and  $15 \times 32$  channels) are considered for the small TRD prototypes. For the large prototypes, a  $8 \times 32$  channel FEB is assumed. The blue squares on each FEB indicate the ASIC numbers [68].



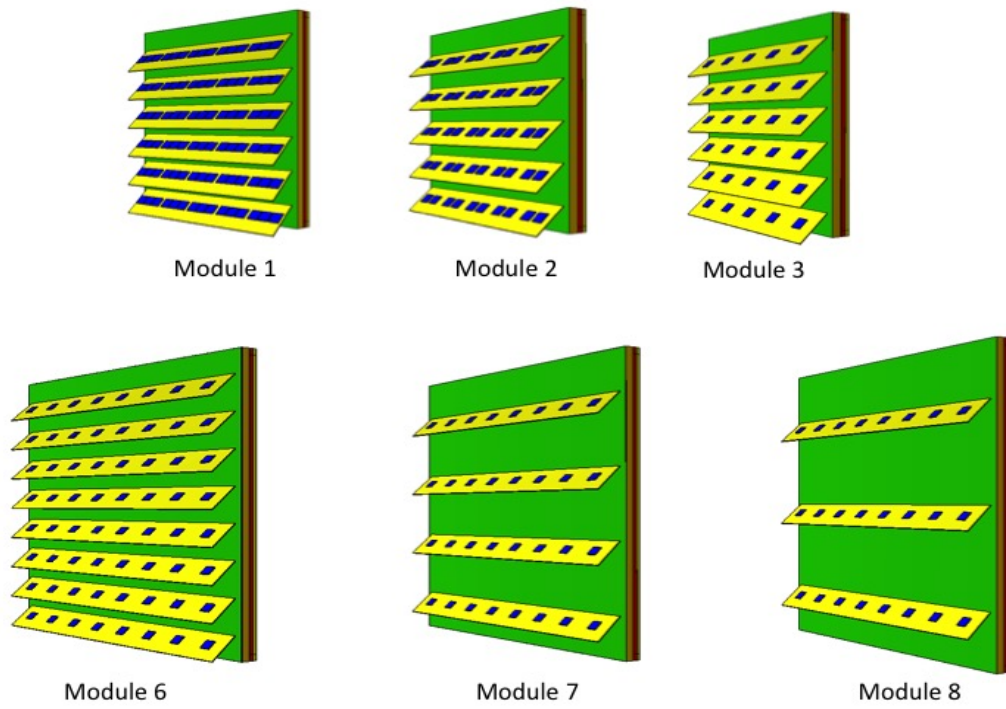


Figure 5.28: Rear view of the six proposed TRD module types for the CBM-TRD equipped with their corresponding FEBs in yellow, according to the simulation [68].



# Chapter 6

## Prototype Design and Construction

As an alternative option to the baseline design configuration of the CBM-TRD for SIS100, as summarized in Chap. 5, some other design configurations of the ROC have been investigated at the Institute for Kernphysik in Frankfurt (IKF) and National Institute for Physics and Nuclear Engineering in Bucharest, Romania, to provide solutions to probable unforeseen experimental challenges.

### 6.1 Prototype Development in Bucharest

The TRD prototypes developed at the National Institute for Physics and Nuclear Engineering in Bucharest follow the design of a MWPC characterized by a 4 mm drift zone and an amplification region with a thickness of 4+4 mm. The pitch between the cathode wires is 1.5 mm and anode wire plane is located in a distance of 4 mm from the cathode wire plane with a pitch of 3 mm in between (see Fig. 6.1). To increase the position resolution, each rectangular pad ( $7.3 \times 27.7 \text{ mm}^2$ ) on the pad plane is segmented diagonally into two triangulars, such that each triangular pad can be readout separately (see Fig. 6.2). The space between each pad is 0.2 mm. The amplification region is separated from the drift zone by a cathode wire plane [69]. The diameters of the cathode wires are  $75 \text{ }\mu\text{m}$ . In the center of the amplification region, an anode wire plane with  $20 \text{ }\mu\text{m}$  diameter is located. The active area of the detector is  $36 \times 8 \text{ cm}^2$ . The data are readout by Fast Analog Signal Processor (FASP) as a front-end board. FASP is designed in Bucharest to operate in a high counting rate environment. It provides signal amplification and shaping with a very high signal-to-noise ratio ( $S/N$ ) [68, 15].

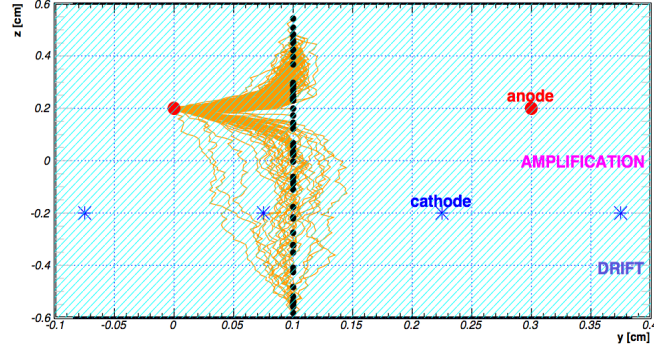


Figure 6.1: Geometry of the active volume and anode-cathode wire planes of the Bucharest TRD prototype [69]. The drift region thickness is 4 mm. The pitch between the cathode wires is 1.5 mm. The anode wire plane is located in 4 mm distance from the cathode wire plane and the pitch between them is 3 mm. An electron avalanche drift and a signal formation in the TRD is simulated with Garfield++ [70].

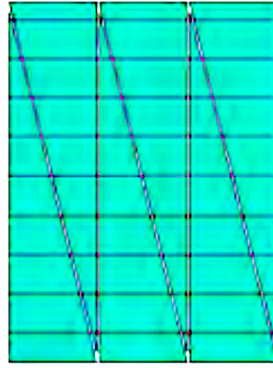


Figure 6.2: The pad plane structure of the Bucharest TRD prototype [69]. A rectangular ( $7.3 \times 27.7 \text{ mm}^2$ ) pad is segmented into two triangular for a better position resolution.

## 6.2 Prototype Development in Münster

The TRD prototypes developed at the Institut für KernPhysik (IKP) in Münster are mostly close to the baseline design configuration of the CBM-TRD for SIS100. Introducing a drift region and enlarging the gas-gap thickness increases the absorption probability of the generated TR photons and therefore the efficiency for the signal generation and particle identification will be optimized. A Kapton-aluminum foil is utilized as the entrance window and cathode plane with a lattice-support structure to avoid entrance window deformation due to the varia-

tion in gas pressure inside the detector. The pad plane and the front-end electronic boards (SPADIC v0.3 and v1.0) summarized in Chaps. 5 and 7, respectively, are used for both Frankfurt and Münster TRD prototypes.

## 6.3 Prototype Development in Frankfurt

At the Institute für Kernphysik in Frankfurt (IKF), the focus had been on developing a fast Read-Out Chamber (ROC) prototype by removing the drift volume from the gas region. The symmetrical design of the chamber without drift region requires only one plane of anode wires (no cathode wire plane) inside the gas region of the detector, which simplifies the construction of this prototype. A thin aluminum Mylar foil is used as the entrance window and cathode plane. To reduce the material budget of the prototypes, no support structure is used for the entrance window. To reduce the effects of the distortion of the entrance window and consequently gas gain variation distortion of the entrance window an alternating wire plane (sense and field wires in a row) is applied in the center of amplification region. Other improvements have been performed which will be discussed in this section.

### 6.3.1 Fast ROC design

Different TRD prototypes based on a fast MWPC design with various active areas and configurations have been constructed and tested at the IKF. The importance of a fast ROC design is due to the high hit rate in the area close to the beam axis. This phenomenon has to be taken into account for SIS300, where the interaction rate will be much higher than at the SIS100. The IKF design concept allows for a signal collection time below  $0.15\ \mu\text{s}$  and thereby can be considered for the chambers in the inner most area of the TRD layers at the SIS300 [68].

The left panel of Fig. 6.3 shows a conceptual design of a fast TRD and the right panel illustrates the layout of a fast TRD prototype, as used during the 2012 test beam at the CERN-PS. The conceptual design, from left to right, consists of a radiator, a thin aluminized Mylar foil ( $20\ \mu\text{m}$  thickness) as entrance window and cathode plane, the amplification region with only one anode wire plane in the center, and the pad plane. It is fast in signal collection time and simple to construct as merely a single wire plane needs to be prepared for each chamber. However, the absorption probability for TR photons in this fast MWPC might be

lower than in the baseline design due to its thinner gas region which might reduce electron identification performance. As the electric field in the amplification region in the fast prototype is directly coupled to the entrance window, the deformation of the window foil will cause significant gain instabilities [68].

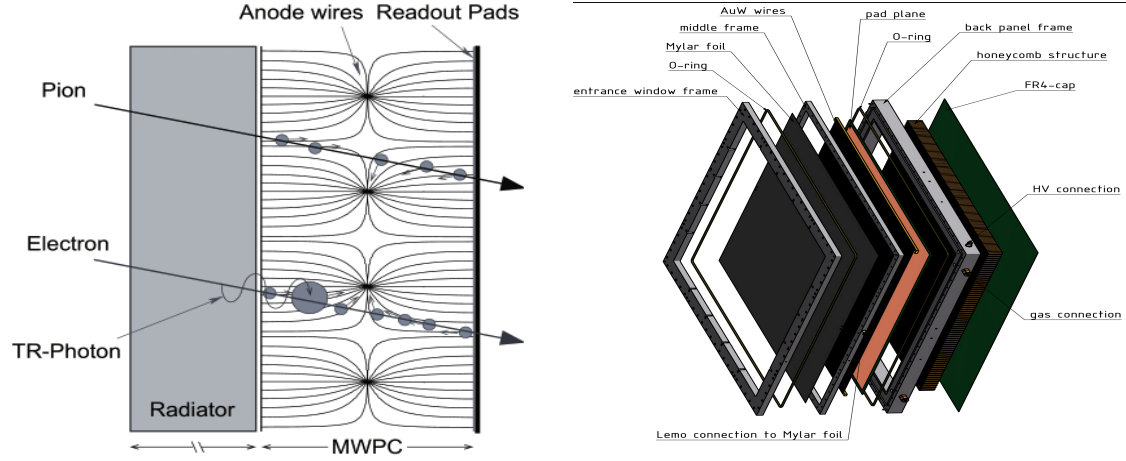


Figure 6.3: **Left:** Sketch of the fast TRD design without drift region. **Right:** A layout of the fast TRD prototype with inner dimensions of  $59 \times 59 \text{ cm}^2$  which used during the test beam at the CERN-PS in 2012. Its dimensions correspond to the full size of an inner TRD module foreseen for the SIS100 and the SIS300 [68].

Two prototypes with the layout shown in the right panel of Fig. 6.3 have been constructed and tested in the test beam at the CERN-PS in 2012. These prototypes are made with inner dimensions of  $59 \times 59 \text{ cm}^2$ . The outer frame was made of aluminum and the back panel was a composite structure of a Printed Circuit Board (PCB) as the pad plane, together with a honeycomb layer, and an exterior layer made of the glass-reinforced epoxy material FR4. These prototypes were designed in two configurations: one with a gas region thickness of  $4 + 4 \text{ mm}$  (“4+4”) and the other one with  $5 + 5 \text{ mm}$  (“5+5”) thickness. The thickness of the honeycomb structure was 30 mm and the total thickness of the chamber, including aluminum frame, was 53.2 mm and 55.2 mm for the (4+4) and (5+5) chambers, respectively. An anode wire (Au-W) grid plane with a pitch of 2.5 mm between wires was used [68]. Figure 6.4 shows a cross-section of a (5+5) prototype and its components (left) and the rear view of a full-size aluminum-frame prototype (right) based on the technical design shown on the left panel.

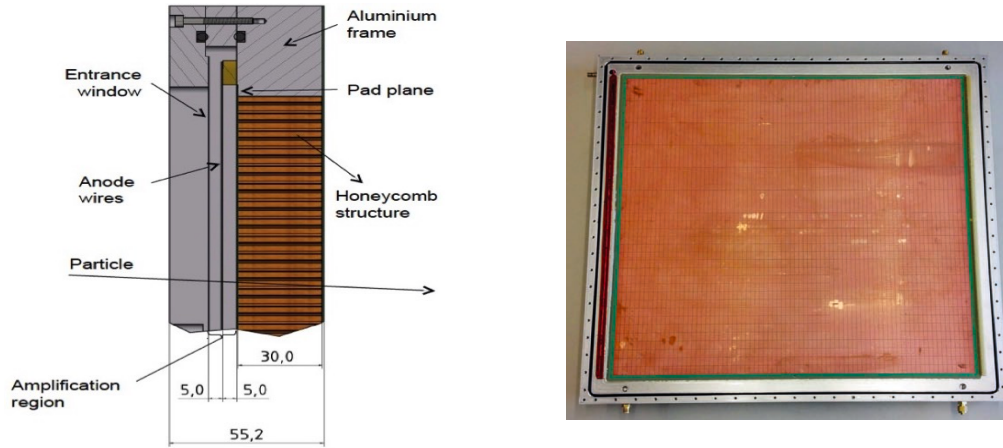


Figure 6.4: **Left:** Cross section of the fast TRD prototype in the 5+5 mm configuration. **Right:** Rear view of the same prototype [71].

### 6.3.2 Fast Prototype with Alternating Wire Configuration

The major drawback of the fast TRD design is the deformation of the cathode foil (entrance window) [hence, the distance between cathode foil and anode wire plane will change] it causes a gas gain instability. A solution to this problem is using a special alternating wire configuration which decreases gain variations caused by cathode foil deformations [77].

A small TRD prototype with aluminum frame ( $21.8 \times 21.8 \text{ cm}^2$ ) has been built to study the effect of the alternating wire configuration. An arrangement of thin sense and thicker field wires in parallel has been constructed for the high voltage anode wire plane with a pitch of 2.5 mm between field and sense wires. The sense wires are made of Au-W with 20  $\mu\text{m}$  diameter and the field wires of Cu-Be in diameter of 79  $\mu\text{m}$ . Figure 6.5 depicts the arrangement of the sense and field wires (left) and the electrical field lines around the wire plane (right). The entrance window is a thin aluminized Mylar foil (19  $\mu\text{m}$  thickness), which serves also as front cathode plane. The rear cathode is a pad plane with readout pads in the size of  $4.7 \times 49.7 \text{ mm}^2$ . This small prototype is designed with a total amplification thickness of 4+4 mm. Figure 6.6 shows the layout (left) and the sketch of the rear of the prototype (right) [15].

Following the first investigation on the alternating wire configuration, two real-size ( $58 \times 58 \text{ cm}^2$ ), thin and fast MWPCs with alternating wires have been constructed at the IKF. The frame and the back panel of this prototype are made of carbon. The use of a carbon frame provides advantages in terms of higher mechan-

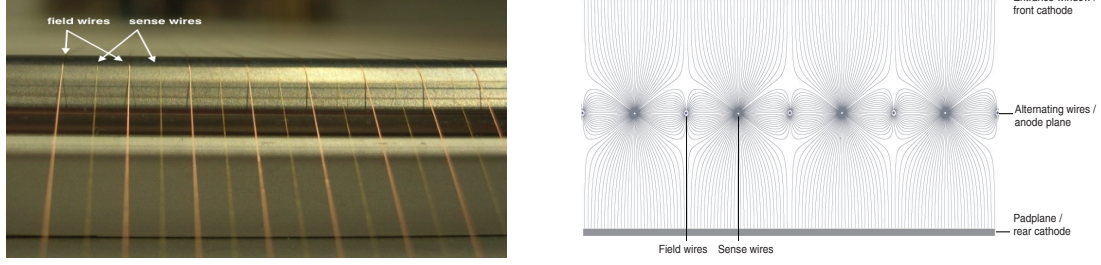


Figure 6.5: Alternating HV wire configuration. Field and sense wires are set in parallel with a pitch of 2.5 mm in between (left). The wire layout together with the resulting electrical field lines (right) [78].

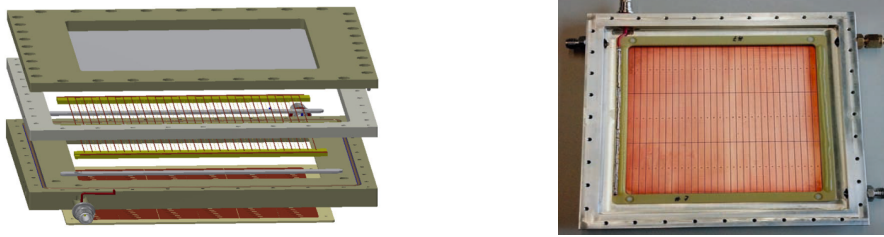


Figure 6.6: A layout of the small TRD prototype from bottom to top consisting of pad plane, aluminum frame, alternating wire plane, a frame and the entrance window foil with its support (left). Rear view of the small aluminum-frame prototype (right) [15].

ical rigidity, low thermal expansion and high friction resistance for the chamber. The thicknesses of their amplification regions (gas gap) are  $3.5+3.5$  mm and  $4+4$  mm, and the total thickness of the chamber is 3.85 cm. Thin amplification regions allow for a faster signal collection, which is of interest in a high counting rate experiment, e.g. at SIS300. The arrangement of the alternating wires is the same as in the small aluminum prototype, to provide a better gas gain stability. The total thicknesses of the chambers including the aluminum cover for the entrance window (to protect entrance window from any damage in transportation) are 4.26 cm and 4.36 cm for  $3.5+3.5$  and  $4+4$  prototypes, respectively. These prototypes are used in the test beam at CERN-PS in 2014 and in the laboratory to perform detector characterization. Figure 6.7 illustrates the chamber with carbon frame and its dimensions.

In the prototype with carbon frame, four gas feed-throughs are embedded inside the frame in the corners (see figure 6.6). Thus, it meets the structural conditions of the TRD chambers, which will have to be mounted close to each other in the final setup [80]. A honeycomb structure with a thickness of 3 cm is set behind the pad plane. The thickness of the pad plane is 0.5 mm and has an

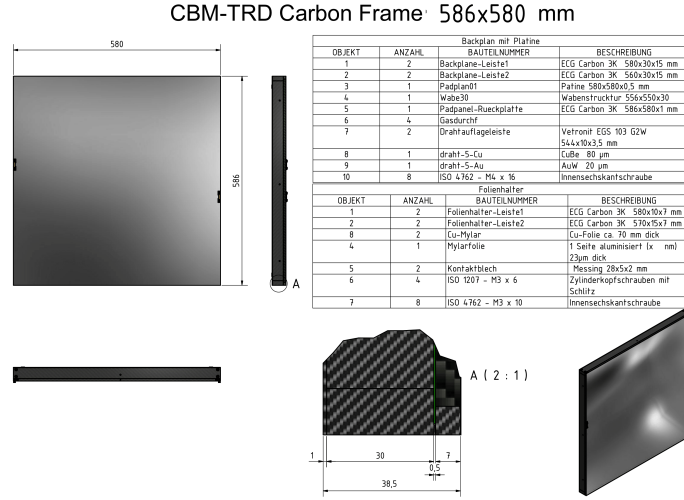


Figure 6.7: Front view of the chamber with carbon frame and alternating HV wire plane performing measurements with  $^{55}\text{Fe}$  source at the laboratory (left), and the sketch of the prototype with its dimensions (right and middle).

active area of  $540 \times 540 \text{ mm}^2$  which is shown in Fig. 6.7. This pad plane was used in Frankfurt and Münster prototypes in the beam test in 2014. The sense wires are gold-plated tungsten (Au-W) with  $20 \text{ }\mu\text{m}$  diameter and field wires are Cu-Be with  $80 \text{ }\mu\text{m}$  diameter. The pitches between sense and field wires are  $2.5 \text{ mm}$ . Figure 6.8 shows a cross-section of both the amplification region and wires (right) and the gas feed-through inside the detector (left).

To test the stability of a MWPC when different high voltages are applied to the chamber in a high rate beam environment, two old transition radiation detectors based on a thin MWPC without drift region have been refitted with a new wire plane and HV cables at the IKF. The chambers have a dimension of  $67 \times 67 \text{ cm}^2$  and gas volume thicknesses of  $4+4 \text{ mm}$  and  $5+5 \text{ mm}$  as mentioned before. An alternating wire grid plane is used in both prototypes as in the latest fast MWPC built at the IKF. The prototype with the  $4+4 \text{ mm}$  amplification region was tested during the CERN-SPS beam test in November 2015.

To sustain the high load at the CERN-SPS beam test, 13 new high voltage cables are added to provide a more segmented high-voltage supply to the detector (see Fig. 6.10). A HV box is considered for 13 HV cables on top of the chamber. The total thickness of the detector is  $55.2 \text{ mm}$  and the entrance window is a stretched, thin-aluminized Mylar foil as used for former prototypes. Figure 6.11 depicts front (right) and rear (left) drawing of this prototype.



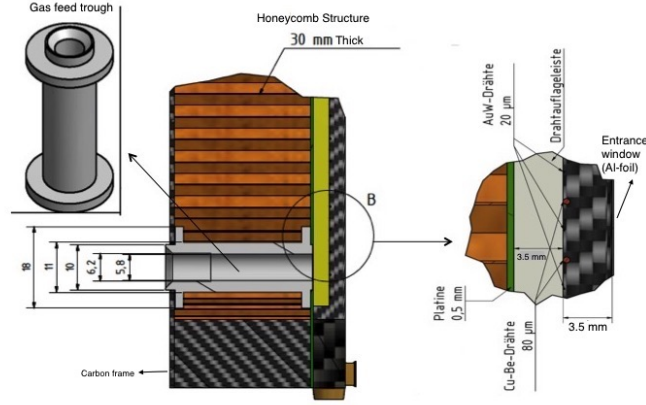


Figure 6.8: A cross-section of the amplification region including alternating wire plane, entrance aluminized Mylar foil and pad plane (right), and a gas feed-through in the corner of the chamber (left).

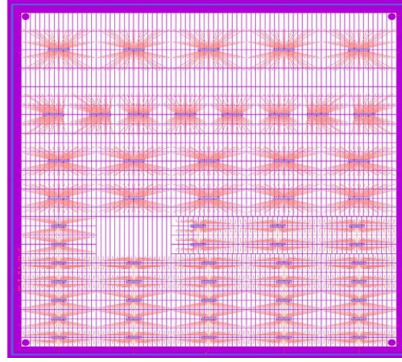


Figure 6.9: A pad plane with an active area of  $540 \times 540 \text{ mm}^2$  and 0.5 mm thickness was used in Frankfurt prototypes (carbon-frame with alternating wires and without drift region) and in Münster prototypes in the laboratory and the beam test in 2014.

## Laboratory Setup and Energy Resolution

To install the setup in the laboratory, softwares for the electronics configuration were installed on a dedicated DAQ machine. Different SPADIC v1.0 FEBs were tested offline (not connected to the detector) to identify the most stable one. A link was established between the FEB (SPADIC v1.0), the SysCore<sup>1</sup> v3.0 and the DAQ (FLIB<sup>2</sup>). A large sample of raw data was registered by triggering the

<sup>1</sup>An interface electronic board between the FEB and the DAQ (explained in Chap. 7)

<sup>2</sup>First-Level Event Selector



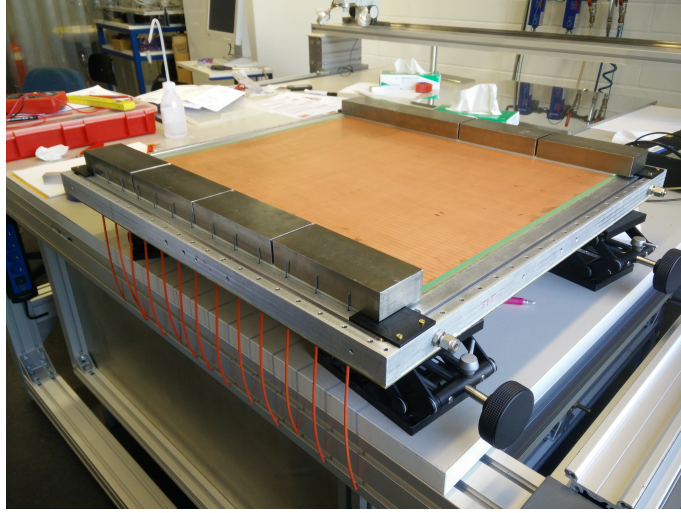


Figure 6.10: Prototype construction. 13 HV cables are added to provide a more segmented high voltage supply to the detector.

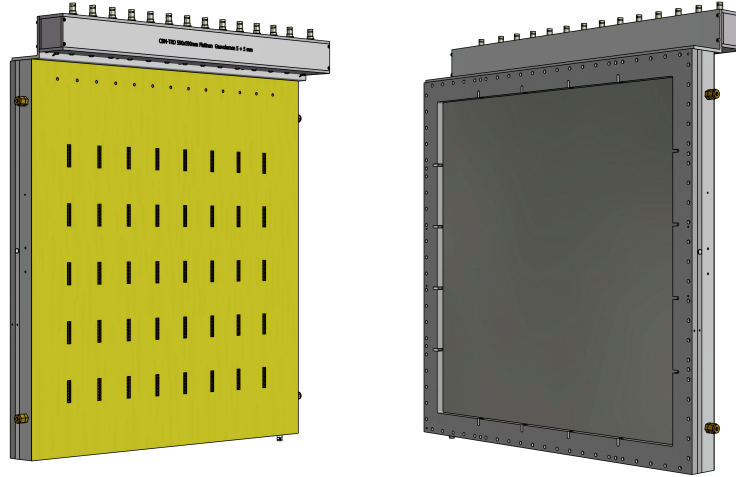


Figure 6.11: Front (right) and rear (left) view of the prototype with 13 HV cables. A HV box is designed for the 13 HV cables on top of the chamber.

SPADIC v1.0 via software to ensure the stability of the readout chain, choose a good configuration for the SPADIC and to see clean signals in all channels while the SPADIC v1.0 is offline and not affected by the noise from the readout chamber. The SPADIC v1.0 was susceptible to several effects such as external noise, small

variations in voltage and current, the temperature of the chip and the stability of the HDMI connection and SysCore v3.0. To recognize and reduce the external effects on the SPADIC v1.0 stability, several power supplies and some voltage adjustments (for both SPADIC and SysCore) were applied. Many HDMI cables with different lengths and brands tested and a grounding scheme similar to the grounding used in the test-beam at the CERN-SPS was applied. The temperature of the chip in the SPADIC v1.0 was monitored regularly. When all channels in a specific SPADIC v1.0 were working and clean signals were observed, the prototype with carbon frame and alternating wires was equipped with that SPADIC v1.0 and irradiated with a  $^{55}\text{Fe}$  source in the laboratory to perform an energy resolution analysis.

Several measurements were done at different high voltages and various SPADIC v1.0 configurations. Following the noise cancellation and baseline correction algorithm (explained in Sect. 9.2), the  $^{55}\text{Fe}$  spectrum was plotted. Figure 6.12 represents a  $^{55}\text{Fe}$  spectrum measured at a high voltage of  $V=1450$  V [81]. The small peak in the left part of the graph (at integral charge value of  $\approx 1300$ ) corresponds to the argon escape peak. Around integral charge value of  $\approx 2300$  the peak of the  $\text{Fe-}K_{\alpha}$ -line is located. A shoulder on the right part of the spectra is emerging in all measurements with all SPADIC v1.0 configurations, which its origin was not clear.

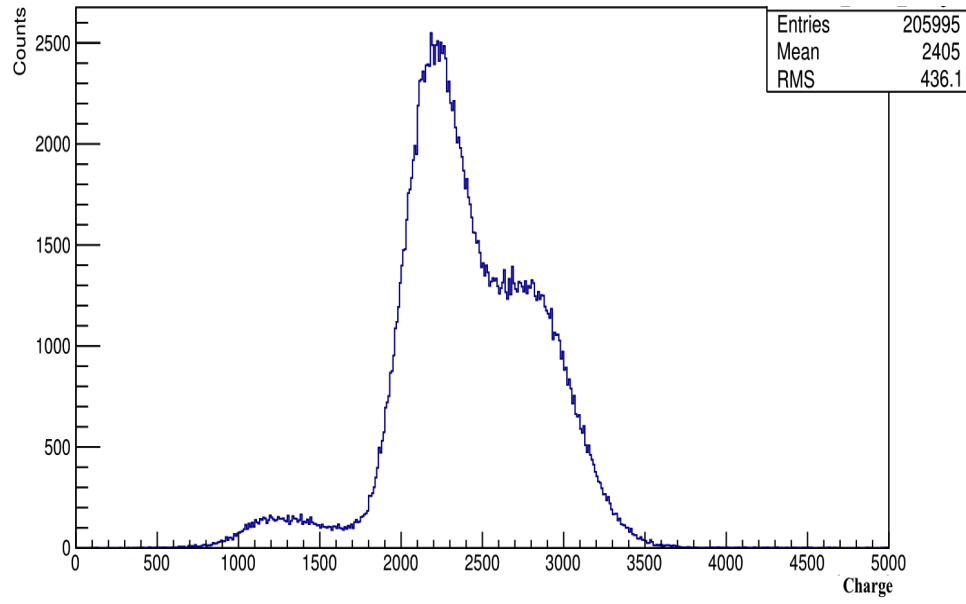


Figure 6.12:  $^{55}\text{Fe}$  spectrum obtained by irradiating the carbon-frame (3.5+3.5) prototype [81]. The first peak in the left part of the graph shows the argon escape distribution and the highest peak indicates the  $\text{Fe-}K_{\alpha}$ -line. A shoulder appears on the right part of the graph in all measurements, which its origin was not clear.

## Simulations for the Fast ROCs

Several simulations of the electric field configuration, the drift time distributions, and the amplification gain variations have been performed [73, 15] for the fast ROC design applying GARFIELD tool [72].

### Simulation of the Signal Collection Time

For two types of MWPC (4+4 and 5+5 mm amplification region thicknesses), the signal collection times are achieved by GARFIELD simulation applying nominal anode voltage [73]. The mean arrival times (over one drift cell) are  $\langle t_D \rangle = 0.054 \mu\text{s}$  and  $\langle t_D \rangle = 0.065 \mu\text{s}$  for (4+4) and (5+5) prototypes, respectively (see Fig. 6.13). The maximal signal collection time for the fast TRD ( $< 0.13 \mu\text{s}$ ) is significantly less than the one achievable for the MWPC with a drift region of 4 mm ( $\sim 0.16 \mu\text{s}$  additional drift time). The difference in the mean signal collection time  $\langle t_D \rangle$  is even of order of 4 for two types of MWPCs (with/without drift region).

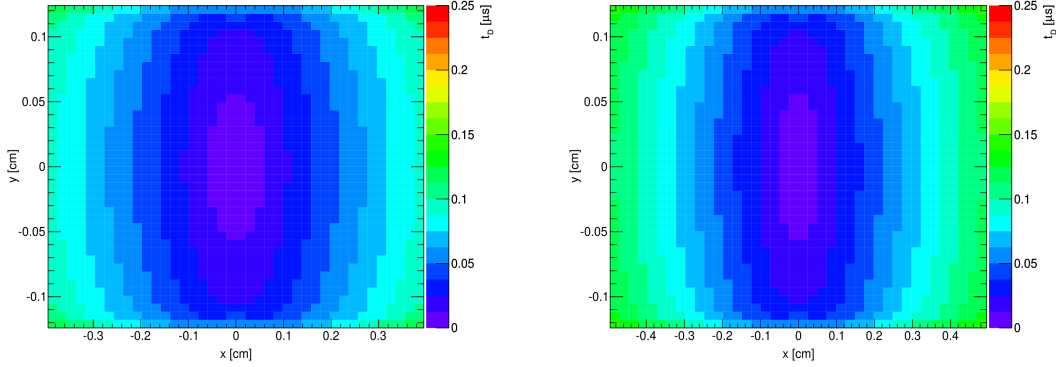


Figure 6.13: The electron arrival times in  $\mu\text{s}$  as a function of the position of the primary ionization relative to an anode wire for the 4+4 MWPC with  $U_A = 1940 \text{ V}$  (left) and the 5+5 type with  $U_A = 2220 \text{ V}$  (right). The gas mixture is Xe/CO<sub>2</sub> (80/20) [73].

Simulations also showed a difference in the signal collection time due to the differences in the electric field configurations between the two prototypes. Figure 6.14 demonstrates the calculated electron-drift time distribution in both prototypes, with alternating wires (right) and without alternating wires (left), using GARFIELD simulations [72, 73, 79]. The prototype without alternating wires displays a relatively flat time distribution in comparison with the prototype with alternating wire, which shows a distribution more peaked towards smaller times.

However, the latter prototype demonstrates a slightly longer tail in the distribution for longer times, although it contains only 20% of the signal in the tail above times of  $0.12 \mu\text{s}$ .

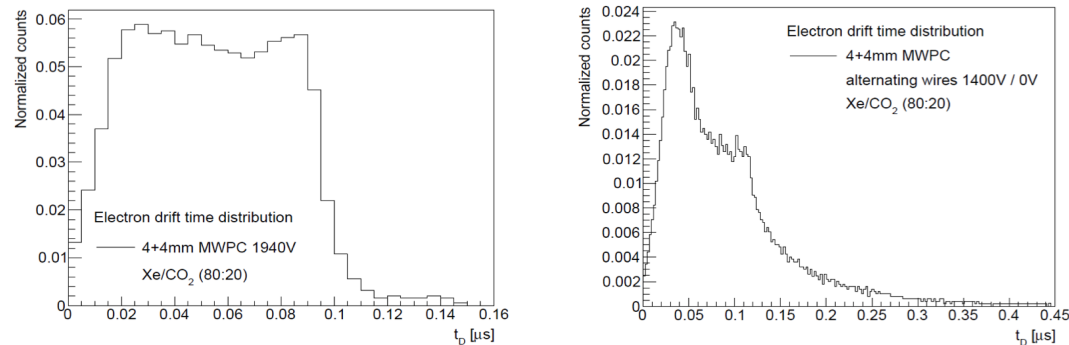


Figure 6.14: The signal collection times in prototype with standard anode wire plane 4+4mm (left) and in prototype with alternating wire plane 4+4mm(right) as simulated with GARFIELD [72, 73, 79].

The prototype with a 3.5+3.5 mm amplification region (see Fig. 6.7) showed an acceptable result in the electron-drift distribution measurement using GARFIELD simulation. A high voltage of 1370 V and a gas mixture of Xe/CO<sub>2</sub> (80/20) was applied. Figure 6.15 shows the gas gain (lower panel) and the signal collection time (upper panel) for the prototype with the 3.5+3.5 mm amplification region [73]. The mean gas gain for the 3.5+3.5 mm prototype calculated as  $\langle G \rangle = 2291$ . Figure 6.16 shows a two-dimensional drift time distribution in the same prototype with the equivalent applied HV and gas mixture.

## Simulation of the Electric Field

The simulation for the electric field in the fast design prototypes is done by [73] using the GAEFIELD program [72]. Figure 6.17 sketches the GARFIELD calculations of the constant potential (left) and electron drift lines (right) for the 4+4 prototype with a wire pitch of 2.5 mm at an anode voltage of  $U_A = 1940$  V. For this simulation, 399 anode wires with a diameter of 20  $\mu\text{m}$  are considered, which results in a total detector height of 100 cm.

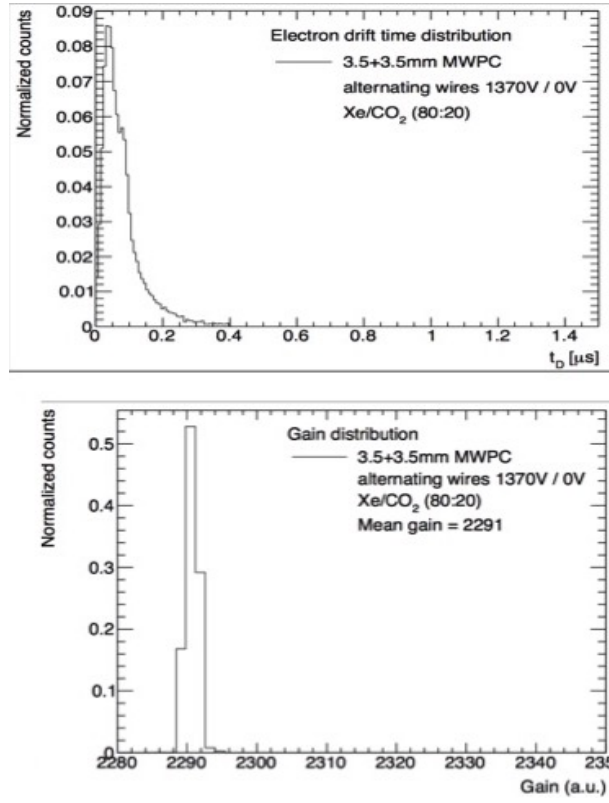


Figure 6.15: Electron drift time (upper panels) and gas gain (lower panels) measurement using GARFIELD simulation [73]. The prototype with 3.5+3.5 mm gas gap showed a shorter tail in drift time compared to prototype with 4+4 mm gas gap (see Fig. 6.11).

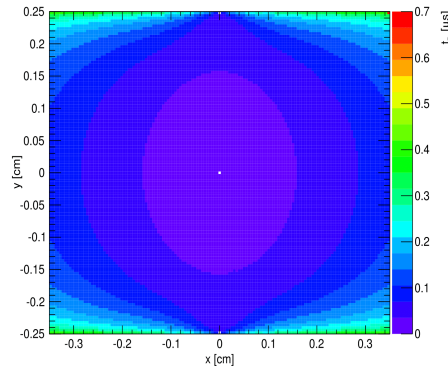


Figure 6.16: A two-dimansional electron drift time in the prototype with 3.5+3.5mm amplification region simulated by GARFIELD [73].

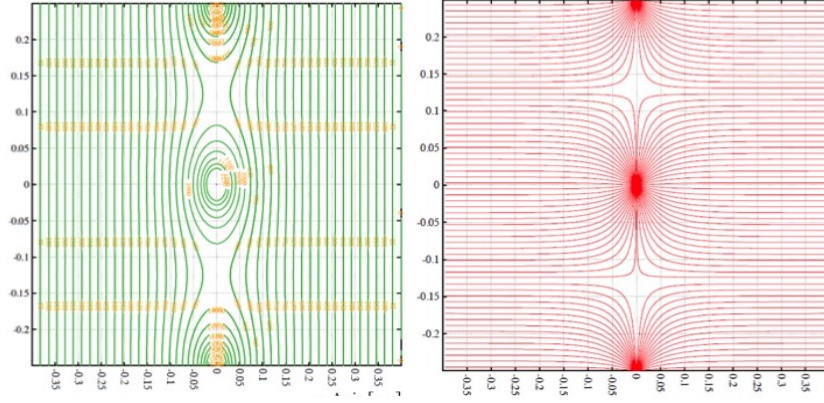


Figure 6.17: **Left:** Constant potential lines **Right:** electron drift lines as simulated by GARFIELD program [72][73] for a fast TRD prototype (4+4) with a wire pitch of 2.5 mm at an anode voltage of  $U = 1940$  V.

## Simulation of the Gas Gain

Gas gain simulations have been performed for both fast prototypes, (4+4) and (5+5), using a mixture of Xe/CO<sub>2</sub> (80/20) in two different anode-wire voltage settings. The statistical mean of the gas gain  $\langle G \rangle$  generated by the avalanche is calculated. Figure 6.18 shows the spatial distribution of the mean gas gain as a function of the position of the primary ionization relative to an anode wire in the central cell of the MWPC. In a given drift cell shown in the Fig. 6.18, a variation of the gas gain in the border of the cells is occurring due to the different drift paths of the electrons. A mean gain factor of  $\langle G \rangle = 2224$  is obtained for the (4+4) prototype applying an anode voltage of  $U_A = 1940$  V, and a mean gain factor of  $\langle G \rangle = 2227$  for (5+5) prototype using an anode voltage of  $U_A = 2220$  V [68].

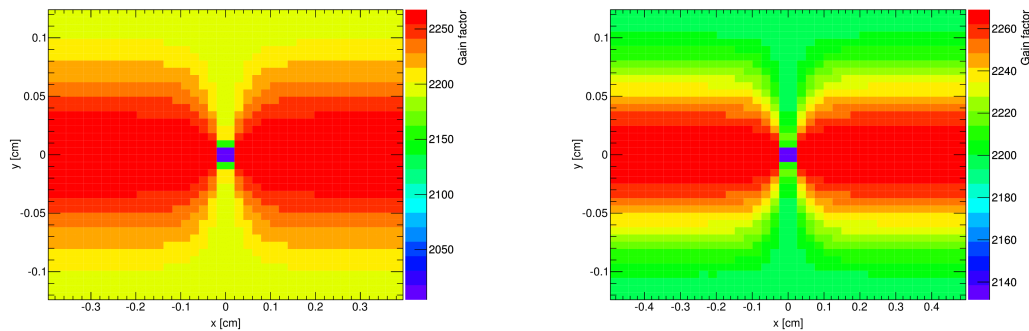


Figure 6.18: The spatial distribution of the gas gain for a gas mixture of Xe/CO<sub>2</sub> (80/20). **Left:** in (4+4) prototype applying  $U_A = 1940$ V. **Right:** in (5+5) version applying  $U_A = 2220$ V [73].

The effect of the cathode foil distortion on the gas gain variation has been quantified by another simulation, taking into account the different geometries of the amplification region [15]. Thus, the relative change of the gas gain is determined. Figure 6.19 indicates that a variation with the distance of 100  $\mu\text{m}$  results to a change of the gas gain by about 10%.

The average gas gain factor as a function of the applied anode voltage is also measured for two different gas mixture ratios (80/20 and 90/10) and three MWPC types (4+4, 5+5 and 6+6) [73]. Figure 6.20 shows the results from this simulation via GARFIELD [72].

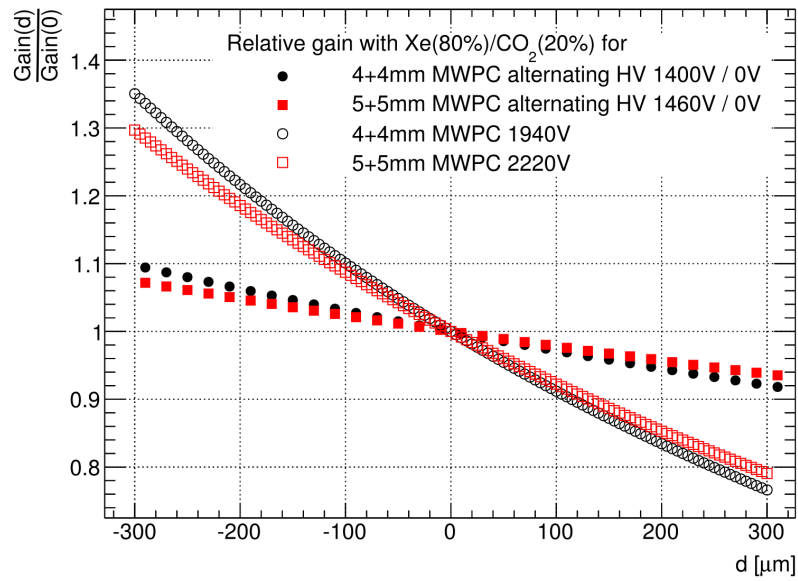


Figure 6.19: The relative gas gain factor as a function of amplification region thickness  $d$  for two geometries (4+4 and 5+5) with and without alternating HV wires. The shown gas gain is for gas mixture of Xe/CO<sub>2</sub> (80/20) [15].



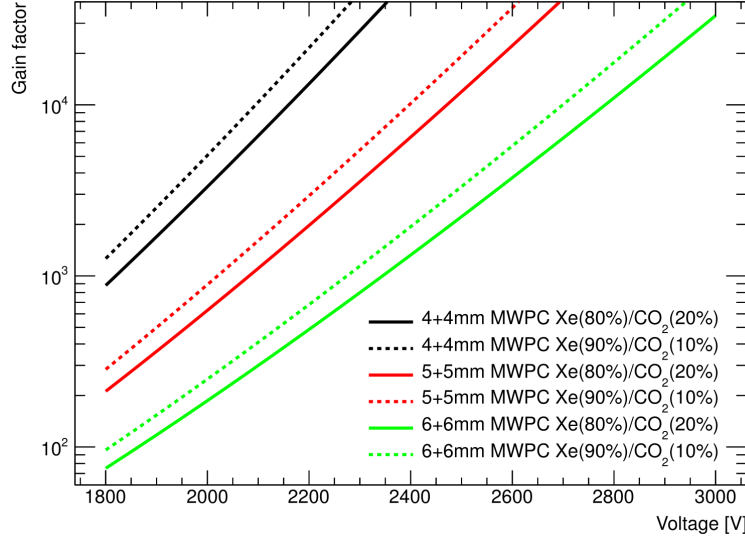


Figure 6.20: Simulation of the changes in the average gas gain factor with changes in applied HV for two gas mixture ratios (80%/20% and 90%/10%) and three different prototype geometries (4+4, 5+5 and 6+6) [73].

To relate the effect of pressure difference to a stretched foil, measurements of the behavior of stretched foils have been performed and compared to calculations [75]. Figure 6.21 represents the resulting deformation pattern of a stretched foil of  $60 \times 60 \text{ cm}^2$ , when a pressure difference of  $250 \text{ } \mu\text{bar}$  is applied. The calculation is based on the corresponding elasticity modulus and thickness of the used Mylar foil and have been done with the finite-elements program ABAQUS [76]. The maximal deformation in the center of the foil was calculated to be  $1.55 \pm 0.16 \text{ mm}$  for a pressure difference of  $100 \text{ } \mu\text{bar}$ . These simulation results are compared with a measurement on a real-size Mylar foil [75] (see Fig. 6.22) and it was found that measurements and simulations are in well agreement at least for the pressure differences below  $250 \text{ } \mu\text{bar}$ . Thus, it is possible to generate a map of gain distortions as a function of position and pressure difference by calculating the spatial distribution of the foil deformation in advance.

The prototype shown in Fig. 6.6 was used to perform some primary measurements in the laboratory with a  $^{55}\text{Fe}$  source [79]. To compare the gas gain variations, a standard prototype was used for the reference measurements. The two prototypes, one with alternating wire plane and the other without alternating wires, were of the same dimensions. While the field wires were on the ground potential, the current along the sense wire in different positions and differential

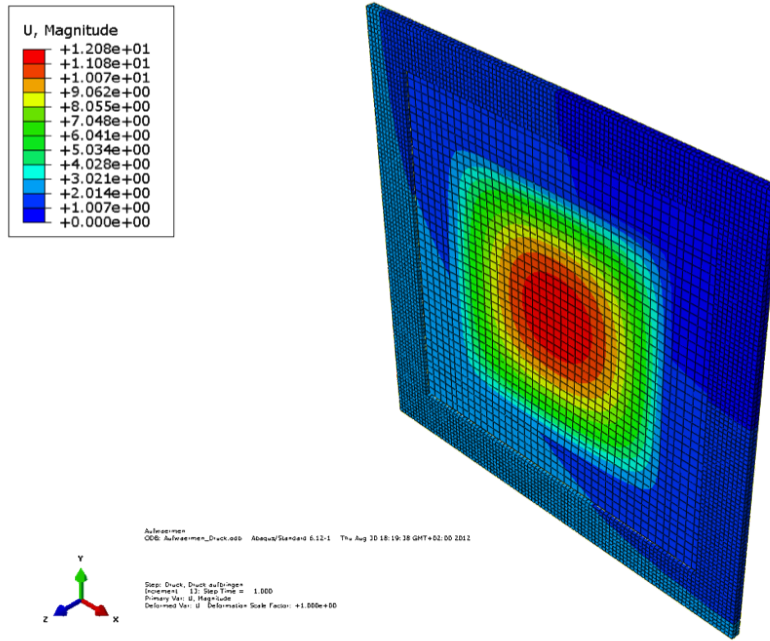


Figure 6.21: The pattern of the deformation of a stretched foil  $60 \times 60 \text{ cm}^2$  for a pressure difference of  $250 \text{ } \mu\text{bar}$  calculated by ABAQUS program [76, 75].

pressures ( $\Delta p$ ) was measured. For a relative overpressure of  $\Delta p = 0.5 \text{ mbar}$ , the standard prototype without field wires shows a variation in gas gain up to 60% (left panel of Fig. 6.23) while the variation is reduced dramatically for the setup with alternating wires to the less than 10% (right panel of Fig. 6.23).

Figure 6.24 shows a two-dimensional distribution of the gas-gain variation for the (3.5+3.5) prototype (showed in Fig. 6.7) simulated by GARFIELD and by applying a high voltage of  $V=1370 \text{ V}$  and a gas mixture of Xe/CO<sub>2</sub> (80/20) [73].

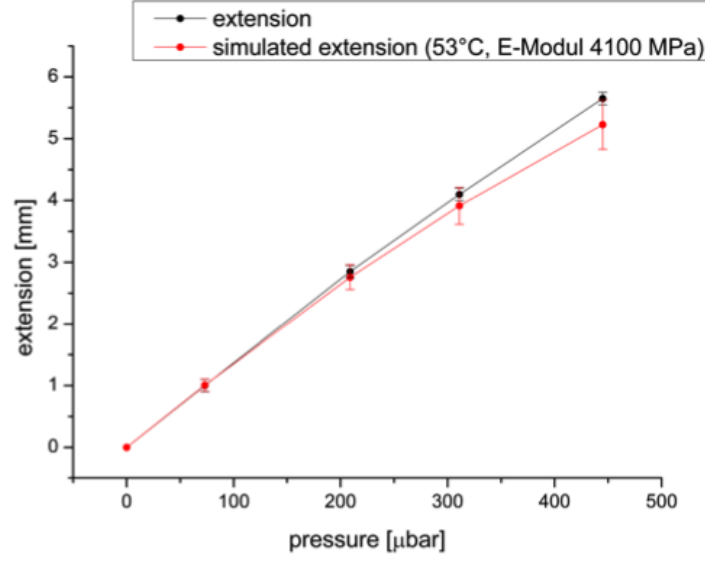


Figure 6.22: Comparison of the simulated deformation at the center of the foil to the measurement on a real size Mylar foil window [75].

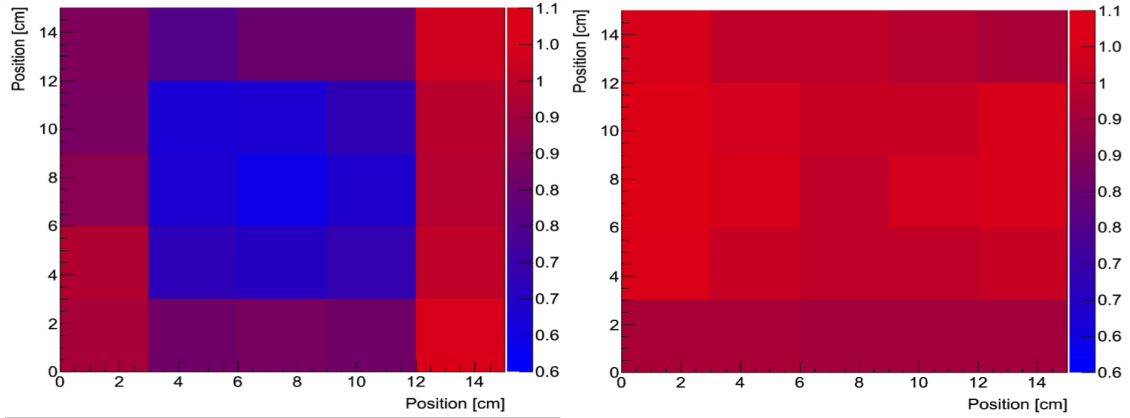


Figure 6.23: A comparison of the position dependent gas gain on the anode wires between the prototype without field wires (left) and the prototype with alternating wires (right) [79]. Measurements were performed in the laboratory for a relative overpressure of  $\Delta p = 0.5$  mbar and by using a  $^{55}\text{Fe}$  source.

## 6.4 Pad Planes for the TRD at SIS100

Three main geometries (v16b, v17a and v17b) of the pad planes are designed for the TRD, however, the v16b geometry is chosen for the all TRD layers at SIS100.

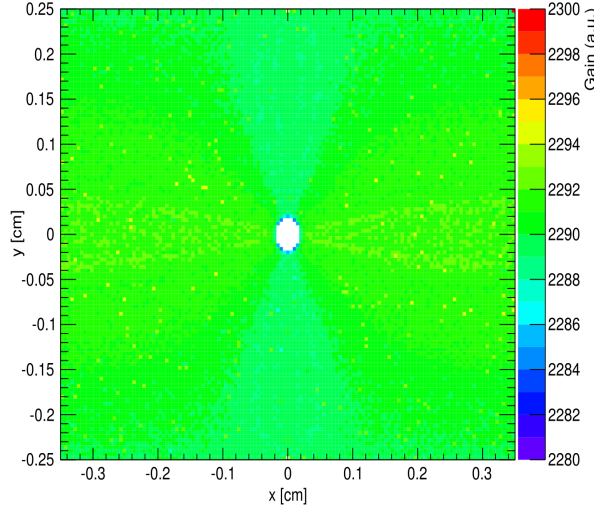


Figure 6.24: A two-dimansional distribution of the gas-gain variation for the (3.5+3.5) prototype simulated by GARFIELD [73]. A high voltage of  $V = 1370$  V and a gas mixture of Xe/CO<sub>2</sub> (80/20) is considered for the simulation.

The pad planes are designed in six different types (types 1, 2, 3, 6, 7 and 8) for six TRD module types. Table 6.1 summarizes the characteristics of the six pad planes and the type of electronics they can be equipped with. The size of the pad planes conforms with the size of the small and large TRD modules ( $57 \times 57$  and  $95 \times 95$  cm<sup>2</sup>). The pad plane for the small modules is made of a single Printed Circuit Board (PCB) and the pad plane for the large modules has to be formed of at least two PCB pieces. The pads on each pad plane are of rectangular shape. Six different pad sizes are foreseen for the six types of the pad plane. The pad planes in the TRD layers 1 and 3 will be placed vertically (i.e. the pads on the pad planes are oriented vertically) which gives an acceptable position resolution in x direction. In the TRD layers 2 and 4, the pad planes are placed horizontally (i.e. the pads are oriented horizontally) to give a good position resolution in y direction.

Three types of FEBs ( $5 \times 2$ ,  $7 \times 1$  and  $8 \times 1$  ASICs) will be used for the six types of the pad plane. Three different ROB<sup>3</sup>s and 1 or 2 GBTx<sup>3</sup> is considered for each pad plane type. Figure 6.26 shows the geometry of the TRD pad planes v16b.

---

<sup>3</sup>An interface electronic board between Front-End Board (FEB) and Data Processing Board (DPB). The SysCore v3.0 (explained in Chap. 7) is replaced by GBTx to handle more FEBs.

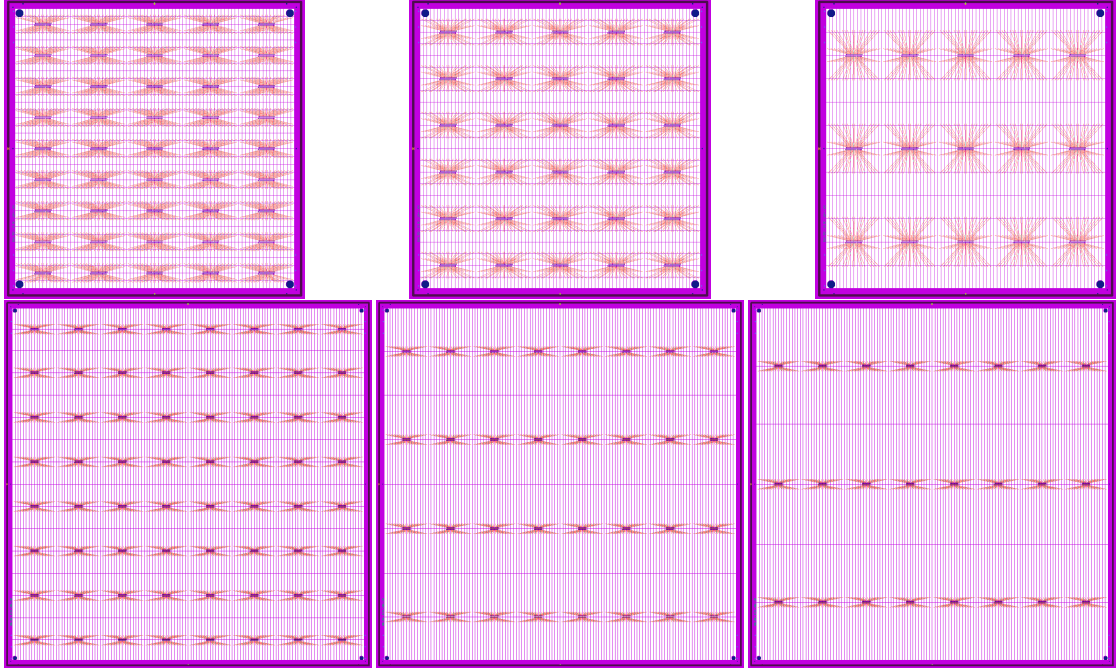


Figure 6.25: The pad planes for module types 1, 2 and 3 from left to right, respectively (upper panels) [74]. They have pads of different sizes (see Tab. 6.1) with 64-pin connectors (will be applied in inner parts in each TRD layer). The pad planes for module types 6, 7 and 8 from left to right, respectively (lower panels) [74]. They have pads of different sizes with 32-pin connectors (will be applied in outer parts in each TRD layer).

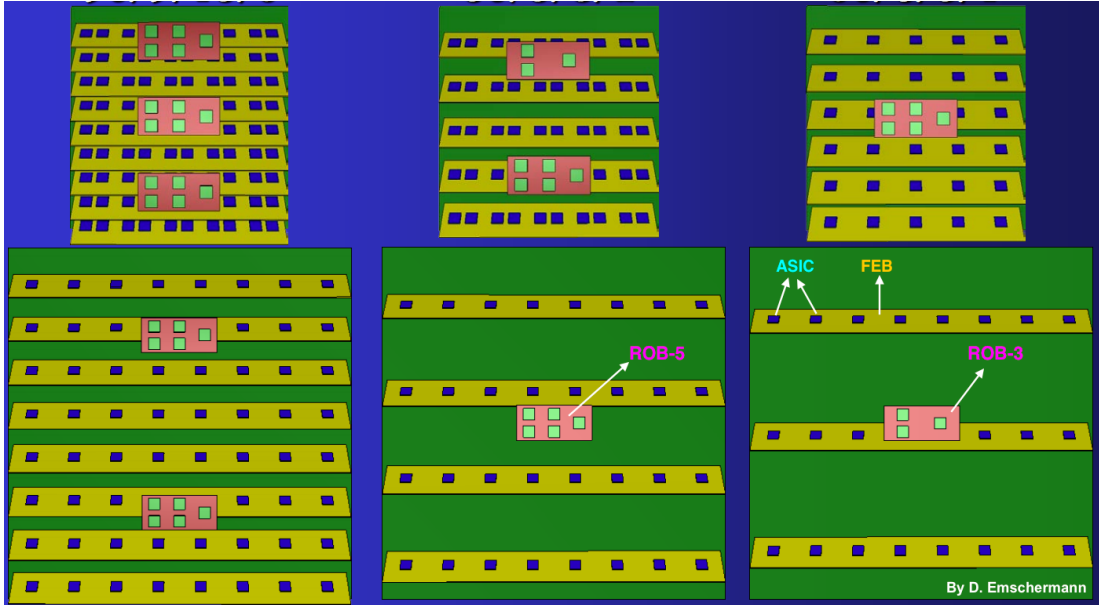


Figure 6.26: Rear view of the TRD geometry v16b [74]. Six module types, three FEB types and three ROB types will be used. Small modules in the most inner part use 3 ROB-5 and 9 FEBs ( $5 \times 2$  ASICs). The most outer part modules have 1 ROB-3 and 3 FEBs ( $8 \times 1$  ASICs).

Table 6.1: The characteristics of six types of TRD pad-plane and the types and numbers of FEB and ROB used for them.

Pad-Plane Type	1	2	3	6	7	8
# Rows - # Columns	36 - 80	20 - 80	12 - 80	8 - 128	6 - 128	16 - 128
# Pads and Channels	2880	1600	960	2048	1024	768
Pad size (cm <sup>2</sup> )	1.01	1.69	3.04	4.13	8.27	10.96
# Channel/pad	64	64	32	32	32	32
# FEBs/pad plane	9	5	6	8	4	3
# ASIC/FEB	5 × 2	5 × 2	5 × 1	8 × 1	8 × 1	8 × 1
# GBTx - ROB-#/pad plane	2 - 7	1 - 3	1 - 5	5 - 2	1 - 5	1 - 3
# Optical link/pad plane	16	10	6	12	6	4

# Chapter 7

## Readout Electronics

Figure 7.1 shows the flowchart of the readout chain used to record data in the laboratory and in the beam campaigns in 2014 and 2015.

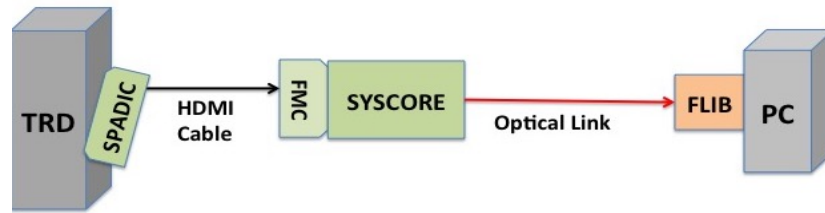


Figure 7.1: Flowchart of the readout chain used in the laboratory and in the beam campaigns in 2014 and 2015. A TRD chamber is equipped with a SPADIC readout board. The SPADIC transfers data to the SysCore readout board via a HDMI cable and FMC (FPGA Mezzanine Card). The data are then transferred to a PC via an optical link and FLIB (First-Level Event Selector) electronic board.

### 7.1 SPADIC

To amplify and detect the charge signals formed in the TRD, a SPADIC (Self-triggered Pulse Amplification and Digitization asIC) chip is directly connected to the chamber. SPADIC is designed to readout and process small electrical detector signals on a single piece of silicon and it has been improved in subsequent versions to be more compatible with the requirements of the TRD.

The first SPADIC in its revision (v0.3) was developed in 2010. It consists of an analog preamplifier and a pulse shaper combined with an 8 bit analog-digital-converter (ADC) and a pulse shaping time of 90 ns. It provides eight readout channels per chip. SPADIC v0.3 could be connected to the SUSIBO as a FPGA readout controller which served as a communication interface between the SPADIC v0.3 and the data acquisition and configuration system. SPADIC v0.3 was used in test-beam campaigns during 2010-2013. The chip on SPADIC v0.3 could be controlled and configured by *Hitclient* software which was standalone and enabled the user to configure and readout the SPADIC and set the trigger threshold for each of 8 channels individually.

SPADIC v1.0 was developed and finalized in 2013 with the ability to cancel ion tail in detector signals, correct the base line for each signal in each channel and adjust signal polarity to positive or negative. These features are explained in details in this section. The chip on SPADIC v1.0 is a mixed-signal readout ASIC (Application-Specific Integrated Circuit) with 32 input channels. SPADIC v1.0 (see Fig. 7.2) is tested and used in the laboratory and in the beam campaigns in 2014 and 2015. It provides low-noise and low-power analog pre-amplification, 8 - bit digitization, self-triggered hit detection, neighbor readout, full pulse recording, meta data generation and synchronization mechanisms [83].

The three initial physical requirements for the SPADIC were determined to be the recording of signal amplitude, arrival time and signal shape. As the deposited energy of the incident particles in the detector is proportional to the integral of the generated signals - which can be determined by the amplitude of the integrated signal - SPADIC is designed to record the amplitude of the signal with an ADC (Analog to Digital Converter) value of 8 bit. Increasing the amplitude resolution enhances the energy resolution, the spatial resolution and the input range for the TRD.

In high collision rate experiments (e.g. CBM), where no global trigger delivers time-markers, an extraction of the arrival time of the signals is essential for the complete reconstruction of collision events. As the required time resolution of all detectors in the CBM experiment is roughly determined by the maximum mean event rate of 10 MHz, the required time resolution is about 100 ns [83].

The shorter drift region in the CBM-TRD (in comparison with the ALICE-TRD) leads to a faster signal collection. An exact measurement of the whole signal shape is important for a more reliable electron/pion separation. SPADIC v1.0 is capable of providing a faster signal recording compared to its version 0.3 [83].



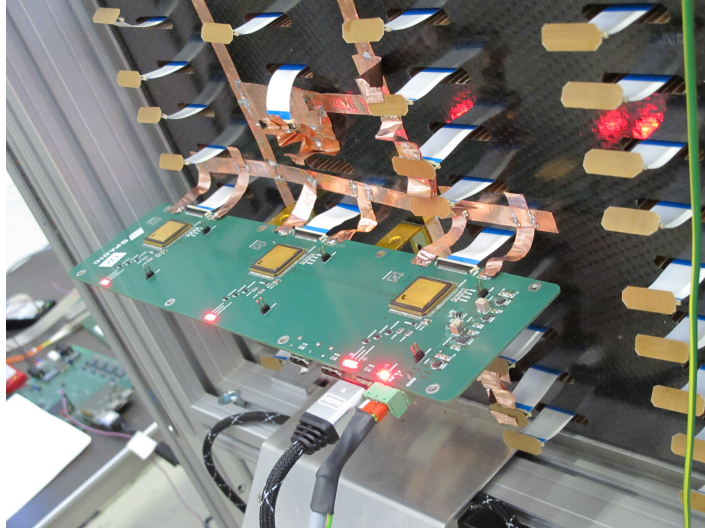


Figure 7.2: A triplet SPADIC (Self-triggered Pulse Amplification and Digitization asIC) v1.0, front-end board, connected to a pad plane on the back of a TRD chamber by three white-flat cables.

The pad plane geometries of the TRD affect some important design parameters of the SPADIC, such as the number of the channels per chip, the maximum hit rate each channel must be able to handle and the maximum load capacitance the preamplifiers have to deal with. A smaller pad size reduces the average hit rate per channel and the capacitive load, which also depends significantly on the capacities of cables and connectors. The geometry of the pad of the TRD limits the maximum average hit rate per channel to 100 kHz at the SIS100 [83].

In a MWPC, the ions drift back from the amplification region and induce a slowly decreasing tail called the ion-tail. In high-rate experiments such as CBM, it is very likely that the tail of a signal caused by a previous hit still has a significant amplitude when a new hit occurs. Therefore, the overlapping of two or more pulses becomes a common issue. This might lead to internal overflows and can cause problems for the internal hit detection logic of the SPADIC. SPADIC v1.0 can record complete pulses and an ion-tail cancellation filter (a digital filter between ADC and hit detection logic in each SPADIC channel) is used to remove slow signal components of the TRD charge signals. The digital filter can also stabilize the baseline by removing the low-frequency oscillations and slow baseline drifts [83].

In the CBM-TRD, the mean signal charge spreads over several electrodes and thus improves the spatial resolution. To allow for higher thresholds, SPADIC

forces the triggering of neighbor channels, if they have not recognized a certain weak signal component by themselves. By properly configuring neighbor channels one can set the trigger threshold such that only the charges gathered by the middle pads within an affected group are directly detected, whereas the charges induced into the border pads are readout only indirectly and due to the enforced readout by the neighbors [83].

### 7.1.1 Data Flow Through the SPADIC Chip v.1.0

In the front-end part of the SPADIC v1.0, the short current pulses from the detector electrodes charge the feedback capacity of the preamplifier. Then a proportional voltage step at the preamplifier output is produced and shaped with a characteristic time constant (80 ns) until a proportional pulse emerges. This time is increased in SPADIC v2.0 to 250 ns. After shaping, the voltage pulse is converted to a current (via a serial resistor) and fed into the current-mode pipeline ADC. Consequently, a digitized pulse is provided in the end of the ADC part (see Fig. 7.5) [94].

In the stream processing part, the digitized pulse passes through some filter stages to perform ion-tail cancellation, baseline correction/stabilization and signal inversion. The hit detection and message building logic select interesting values of the stream, combine them with lots of meta data (e.g. time-stamp, stop type, trigger type and channel-ID) and generate hit messages. In the inter-channel data transfer part, the messages which are stored in the 16 channels together with epoch messages in a dedicated 17th epoch channel are combined to one single message stream and can be accessed if the resulting message stream is ordered in terms of the initial time-stamp via an arbiter. Finally, the merged and sorted message streams are transferred into the CBMnet protocol (a transport and synchronization logic block), serialized and sent out of the chip [83].

### 7.1.2 The Detection of Hit and Trigger Concept

In the digital part of the SPADIC, the hit-detector block provides two adjustable thresholds (threshold 1 and 2) and can be configured in two modes (normal and differential mode). The advantage of two thresholds (instead of one) is to set a more conservative trigger condition in both configuring modes. However, one threshold can be disabled completely, simply by setting the other threshold to the lowest negative digital value. By choosing the normal mode in the configuration process,

two data values ( $n$  and  $n - 1$ ), where  $n$  is the time bin, are evaluated at once. If both values are greater than their respective threshold, an internal hit signal is produced (see Fig. 7.3). If the differential mode is chosen, the hit detection works similarly, but is fed with the differentiated input values  $((n) - (n - 1))$  and  $((n - 1) - (n - 2))$  instead. The differential mode allows to detect double or multi-hits much more efficiently (compared to the normal mode) as it is independent from absolute values or the baseline [83].

When a pulse is recognized by the hit detector, the generated internal hit signal will be sent to all (selected) neighbor channels as well as directly to the internal hit synchronization logic. In SPADIC v1.0 (and newer versions) each channel can be triggered by hit signals of all selected/configured channels and also by its own internal hit signal [83].

It is possible to program many different neighbor relationships, for example, triggering some of the direct neighbors (e.g. channel 8 triggers channels 6, 7, 9 and 10) or a complete readout scheme (i.e. channel 8 triggers all other channels). The hit synchronization block re-synchronizes the internal and external (coming from the neighbors) hit signals. Figure 7.3 shows the block diagram of the hit detection, neighbor triggering and hit synchronization in the digital part of SPADIC [83].

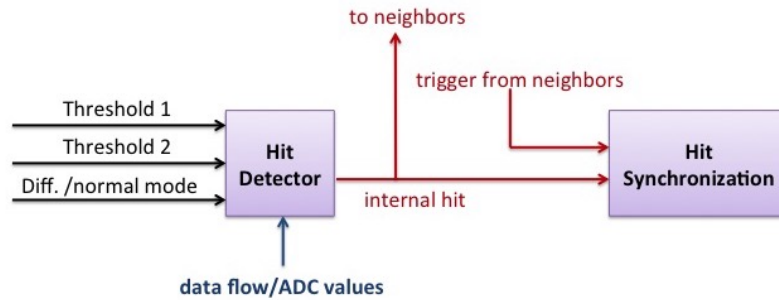


Figure 7.3: A part of the hit detection and message builder logic in the digital part of the SPADIC. The data flow/ADC values are monitored by the hit detector and if it detects the threshold-crossing of a value stored in the input buffer, an internal hit signal will be generated and optionally sent to selected neighbor channels. The hit synchronization eventually triggers the generation of a new message.

Figure 7.4 illustrates the architecture of the SPADIC v1.0. The charge pulses from a TRD pad is detected in every channel of SPADIC. The ADC converts the analog pulse into digital values (see Fig. 7.5). Then the digital pulses from all channels (in each channel group) are recorded as a single message stream (signal-

snapshot plus metadata) ordered by their time-stamps [84].

When a SPADIC is triggered by a charge pulse from the detector, a message in each enabled channel is generated with a specific time-stamp. Every channel group has 16 channels plus one epoch channel which inserts epoch markers. One epoch message is generated each time a time-stamp wraps around (see Fig. 7.6). To recognize when an event happens, the time-stamp and epoch markers should be synchronized [84].

A Charge Sensitive Amplifier (CSA) is used in each channel separately for both positive and negative signal polarities. The input signal in each channel is amplified by a CSA and then continuously digitized to 8 bits at a constant sampling rate of up to 25 MHz. The resulting stream of amplitude values (samples) is further processed by a digital filter [84].

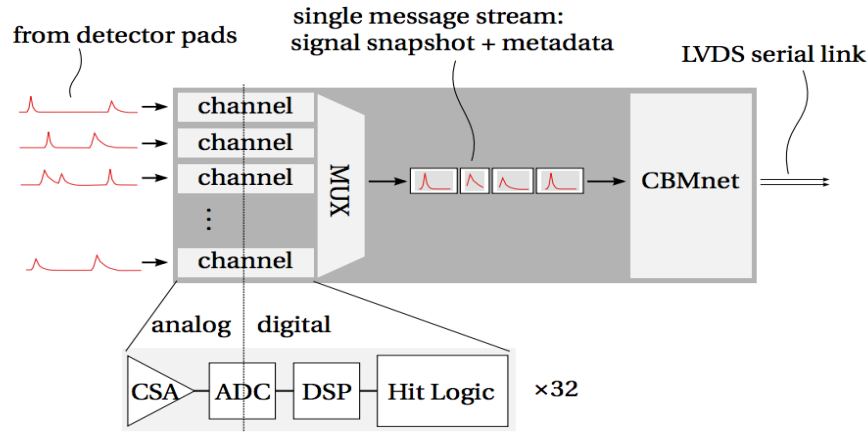


Figure 7.4: Architecture of the SPADIC v1.0. The charge pulses from the detector pads are detected by the analog part in every channel and converted to digital pulses by the ADC. The digital pulses will be synchronized and ordered according to their time-stamp as a single message stream with metadata before they are transferred to the DAQ via HDMI cable from CBMnet [93].

As mentioned, the SPADIC v1.0 can register single and multi-hit pulses. For instance, a typical pulse sequence which contains a single pulse that is followed by a double pulse is shown in Fig. 7.7. A normal hit message generated by the hit detector contains a sequence of data values, which has been configured via a selection mask in advance. In this example, the selection mask is set to 1111-0001. In this case, all of the 8 possible values except for the 5th, the 6th and the 7th are stored in the hit message. The actual selection mask of the SPADIC v1.0 has 32 entries. The second overlapping pulse can be recognized due to the virtual

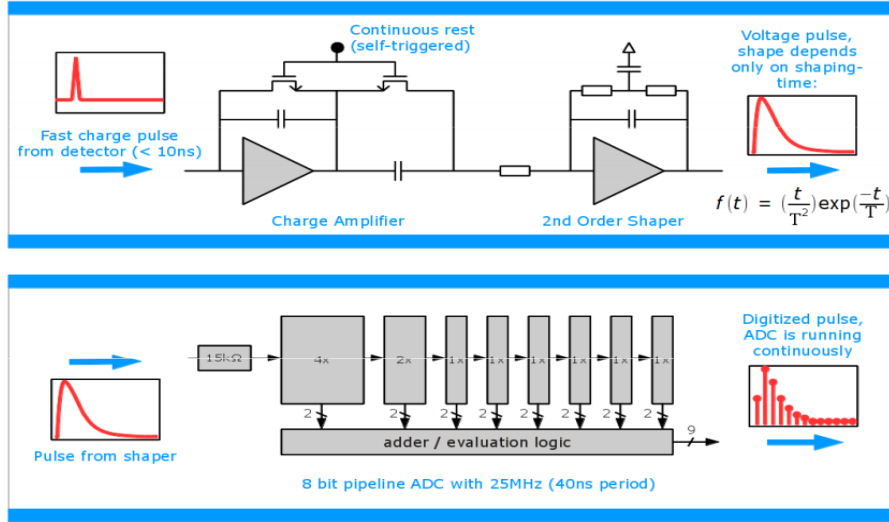


Figure 7.5: Fast charge pulse amplified and shaped as a voltage pulse. The voltage pulse is then digitized by an ADC [94].

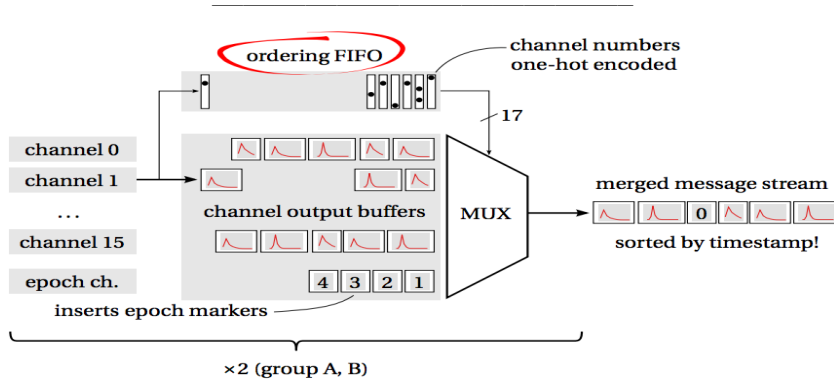


Figure 7.6: Each channel group has one epoch channel which insert epoch markers [93].

threshold. When the SPADIC is set to the differential mode, the threshold is called virtual. The double pulse (right part in Fig. 7.7) at first triggers the generation of a new normal hit message, but due to the second overlapping pulse, the generation of the normal hit message is interrupted eventually. The hit control block (not shown) finally handles a normal message and immediately generates a new multi-hit message. At the same time, the selection mask is reset and thus again only the most interesting values of the overlapping pulse are stored in the multi-hit message. If a pulse is not recognized directly by the hit detector but a neighbor channel sends a trigger signal, the same selection and generation mechanism is started [83].

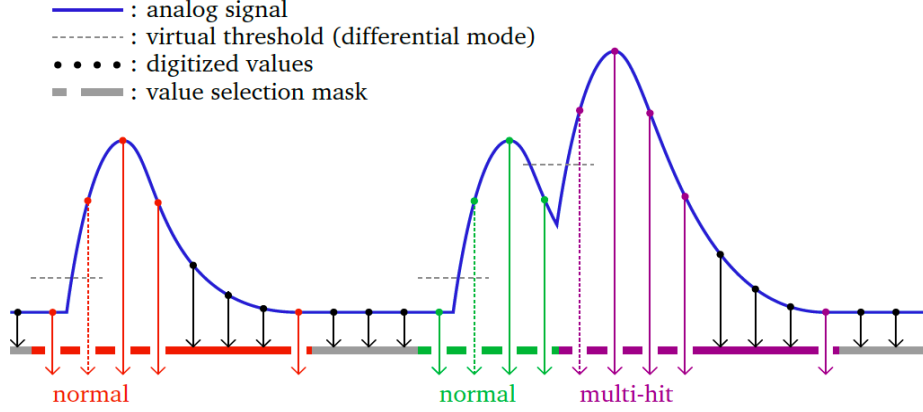
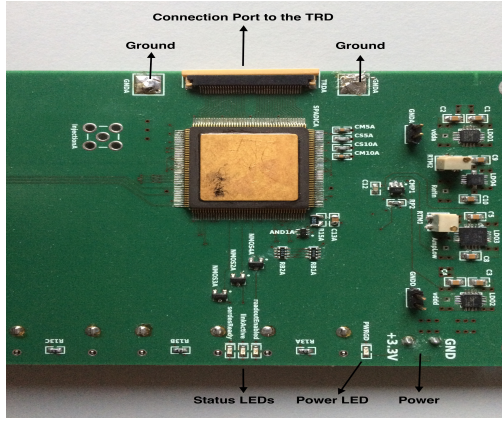


Figure 7.7: A normal pulse (left) followed by a multi-hit (right) pulse. Each time the (virtual) threshold is crossed or a neighbor sends an external hit signal (not shown), a new message is produced. The hit selection mask is reset when a multi-hit is detected. The colored vertical arrows indicate recorded data values and the dashed ones show how the recorded data values are correlated to the latched time-stamp [83].

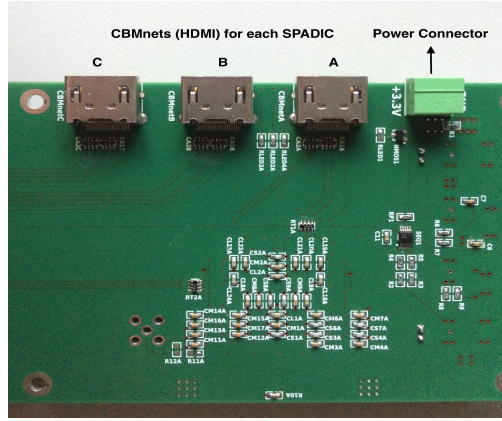
In order to assign the recorded data values to the arrival time of the pulse, a unique time-stamp must be added to each generated message. For this, each time a new hit is recognized by the hit logic, a global (and previously synchronized) counter is latched to the hit and the latched value is added as meta data in front of the hit message (colored-dashed vertical arrows in Fig. 7.7) [83].

### 7.1.3 Structure, Configuration and Recorded Data

The front and rear views of the SPADIC v1.0 are shown in Fig. 7.8. The SPADIC runs with an electric potential of 3.30 V. When it is connected to a power source, the `PWRGD` LED should be on. Each SPADIC connects to the TRD's pads via a flat cable. The connection port has 32 pins which is equivalent to the number of channels and also to the pad plane segmentation. If there is a link between SPADIC and SysCore (to be explained in next section), the `linkActive` LED on the SPADIC glows. The `readoutEnabled` LED demonstrates the existence of a link between the SPADIC and the readout. The `serdesReady` LED is referred to the serializer/deserializer-data part of the chip. For each SPADIC to be fully functional, all four LEDs must be on.



(a) Front view of the SPADIC v1.0



(b) Rear view of the SPADIC v1.0

Figure 7.8: (a) Front view of the SPADIC v1.0. The shown are chip, LEDs, 32-pin connector and ground connectors. (b) Rear view of the SPADIC v1.0. The CBMnet (HDMI) connectors and power connector are shown.

After establishing links between the electronics components (SPADIC, SysCore and DAQ), the SPADIC can be configured by a software either manually or automatically (self configured). The configuration UI (User Interface) has five pages where one can set the two thresholds and configure the SPADIC. On the first page of the UI (global digital settings), the two thresholds and differential mode can be adjusted (see Fig. 7.9). Page 2 is for the global analog settings. The channels are divided into two groups (A and B). They can be selected or turned off. Their baselines and triggering status can also be set manually on page 3 (see Fig. 7.10) and 4 (not shown).

By running the macro `spadic_do_all`, the SPADIC will be configured automatically and appropriate baselines are selected for each channel. In this case, only the two thresholds and differential mode have to be set manually. Thresholds are between -255 and +255 values. The maximum threshold value (+255) means that a threshold is not selected. The macro `spadic_do_all` resets the SPADIC, applies a default configuration, adjusts the baseline for each channel and sets the neighbor trigger matrix. However, each of these can be set arbitrarily by their own macros.

Stop type is a message which determines how a pulse is ended. If a pulse is ended without interruption, the stop type message is *normal end of message*. When a pulse is interrupted by another pulse before it ends (see Fig. 7.7), the selection mask is restarted and the stop type message is *multi hit*. When a channel buffer is full and the MUX cannot read fast enough (see Fig. 7.6), the message is



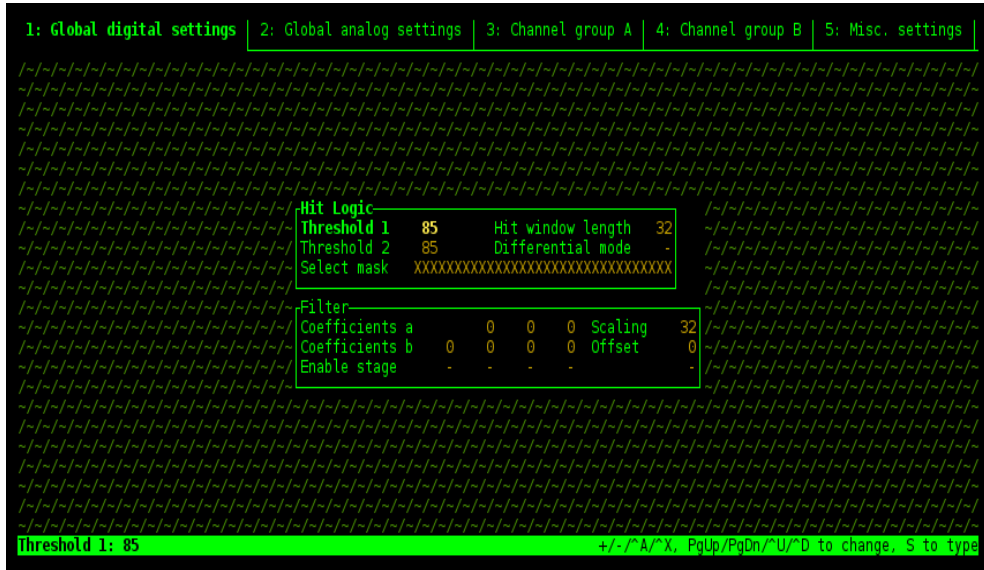


Figure 7.9: Page one of the SPADIC User Interface (UI), the software which is used to configure the SPADIC. The shown are hit logic and filter. Two values for the thresholds (1 and 2) can be chosen. Differential mode can be turned on or off. Hit window length should cover 32 channels. The selected masks should be on as it is shown. The filter is set automatically by configuration macros and does not need to change or set manually.

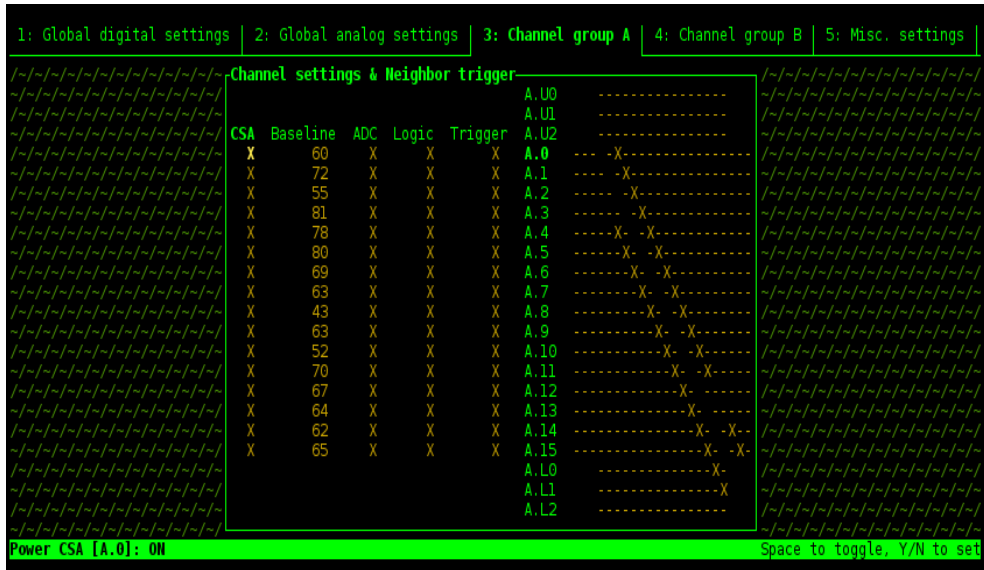


Figure 7.10: Page three (channel group A) of the SPADIC User Interface (UI). The baseline for each channel can be configured individually, however, they can be set automatically by configuration macros. CSA, ADC, Logic and Trigger can be turned on or off.



*channel buffer full.*

A sample of recorded raw data is shown in Fig. 7.11 (stream data messages) and Fig. 7.12 (signals in 32 channels). This data is obtained from a measurement with the  $^{55}\text{Fe}$  source in the laboratory, using the carbon-frame detector prototype (3.5+3.5), the SPADIC v1.0, SysCore v3.1 and FLIB as the readout chain. The color codes in the raw signal represent the yield.

In Fig.7.11, the TriggerSum histogram shows how often each FEB is triggered as a function of counts. The ClusterSize histogram indicates the distribution of the cluster in each channel. The CountRate histogram presents the number of counts in each channel. The baseline histogram shows the baseline in each channel. The Trigger Heatmap histogram shows triggered channels and the heat rate (how much a channel is hit by the detector signal) in them. In the Trigger Heatmap histogram, the lower half part indicates channel group A (16 channels), and the upper half part is channel group B (16 channels). The TriggerCounter histogram presents the time slices filled by triggering. It changes constantly as long as the data is recorded. The StopType histogram displays the type of message which is led to end a pulse. The InfoType histogram demonstrates the type of message in each channel. The TriggerType histogram displays the type of triggering (self triggered or neighbor triggered) of each channel. The Message Length histogram shows the length of each message as time bins in each channel. The TriggerType\_ClusterSize histogram shows the cluster size of each type of triggering mode.

In Fig.7.12, the ADC values are filled as a function of time bins (x-axis). Channel 1 is in the most left-bottom part of the figure and channel 2 is the next one above it and so on and so forth. Vertical variations of the signals are due to the electronics noise. Stronger signals in channels 20, 21 and 22 indicate the position of the  $^{55}\text{Fe}$  source.

#### **7.1.4 Issues with the SPADIC v1.0 and Improvements in Newer Versions**

SPADIC v1.0 is a fast readout which is compatible with the requirements of the TRD. The digitization, metadata and multi-hit detection are taken into account and worked well in the laboratory measurements and the beam campaigns 2014 and 2015. An optimal use of the available dynamic range (-255 – +255) was established during the beam campaign 2014 (baseline at -230, pulse height above +200). However, some instabilities in the amplifier were observed and it was

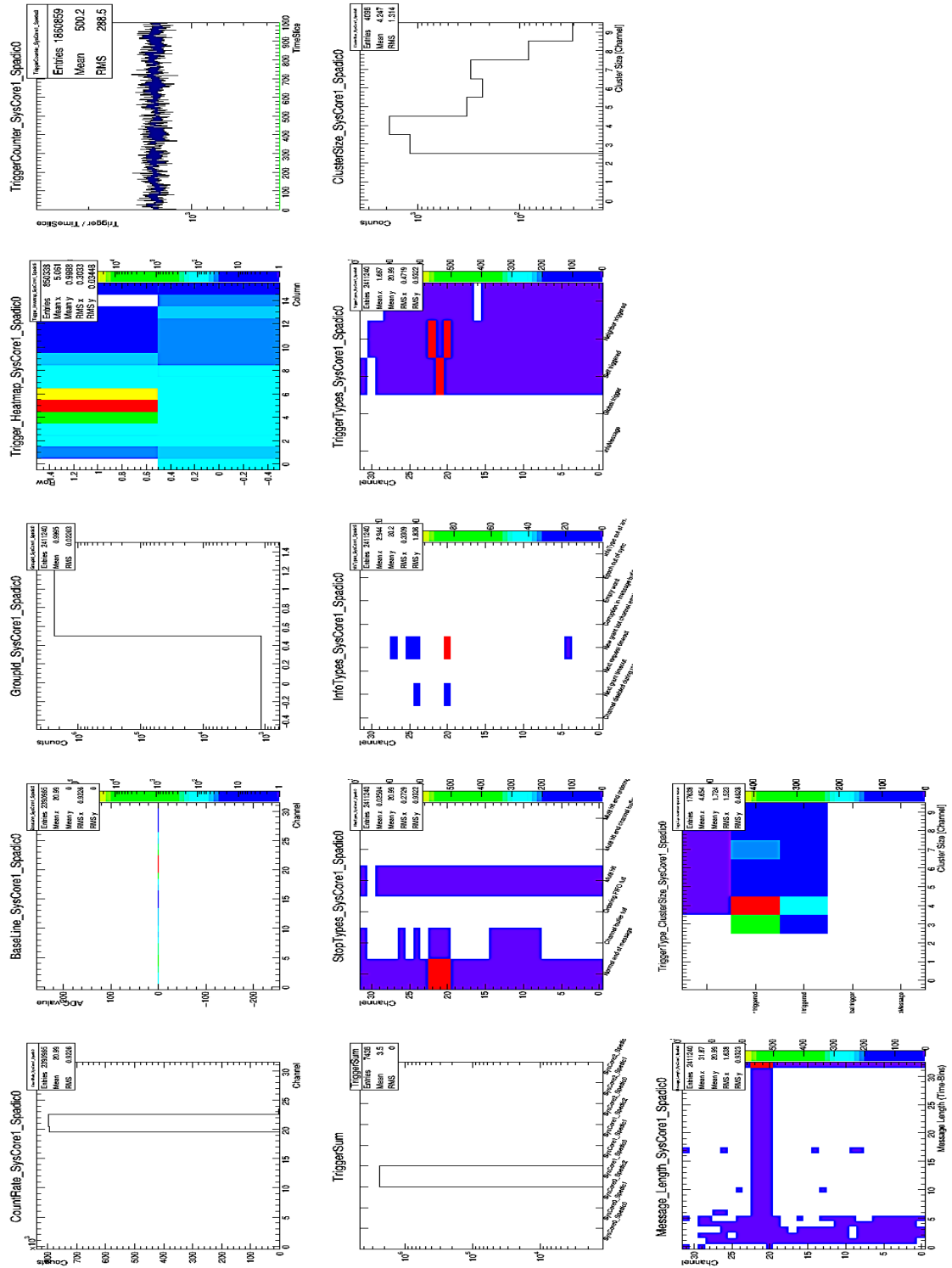


Figure 7.11: Stream data messages (e.g. channel status, triggering status, cluster size). The histograms form during data recording.

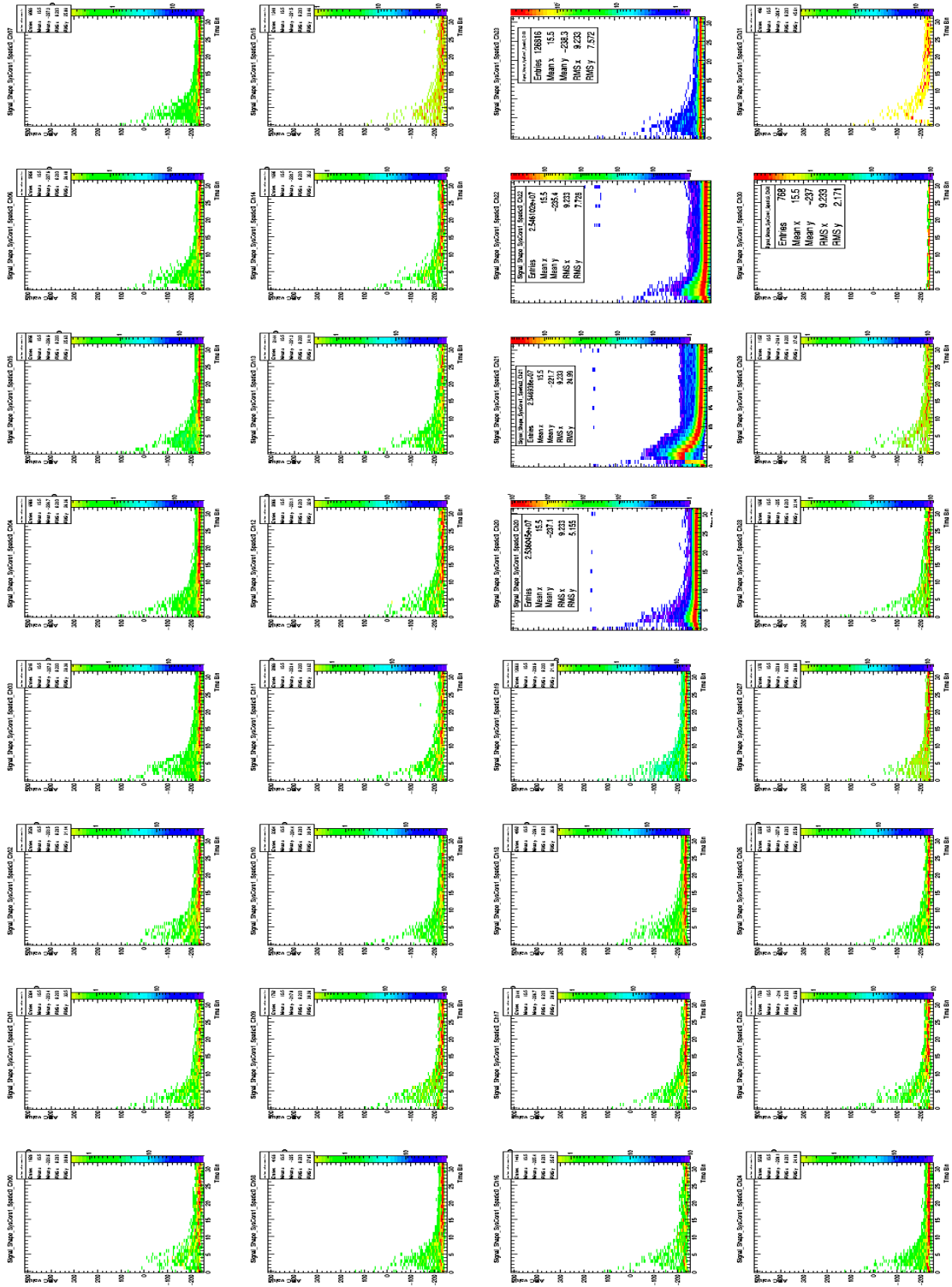


Figure 7.12: The signals in 32 channels formed by both  $^{55}\text{Fe}$  source and electronics noise in the laboratory.

difficult to establish a connection (link) between SPADIC and SysCore via HDMI cable. That means there was a glitch in the serial data output which is improved in the newer versions SPADIC v1.1 and SysCore v2.0. If the threshold is set to a negative value (in SPADIC v1.0), the positive values of a pulse ( $n > 0$ ) cannot be detected which indicated a bug in the hit detection logic. This issue is also modified in newer versions [85, 86].

If the SPADIC v1.0 is used, only positive thresholds could be chosen when one applies differential mode on the UI configuration of the SPADIC [86].

Some noises appear due to the fluctuating voltage or current at the detector output and is always present whether there is radiation or not. Another electronics (e.g. power supply, MPOD, etc.) may affect the SPADIC and generate noise into the output data. To decrease the noise an appropriate grounding should be applied. Figure 7.13 shows a sketch of the grounding we applied during the beam campaign 2015. To make the differential potential between two components (e.g. beam table and SPADIC or between two SPADICs) as low as possible, we connected all of them to the main ground cable in the hall. The neighbor pad sections (around the SPADIC) were also connected to each other (see Fig. 7.2). Figure 7.14 depicts a noisy (a) and a good (b) signal from one channel of SPADIC v1.0 [85, 86].

The chip on the SPADIC v1.0 sometimes showed a sensitivity to high temperatures. The temperature of the chip can be decreased by pasting a small aluminum or copper heat sink radiator on it (an example is shown on Fig. 7.15) [85, 86].

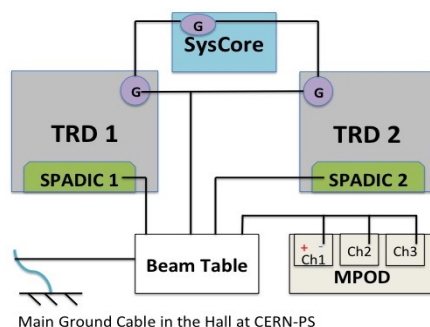
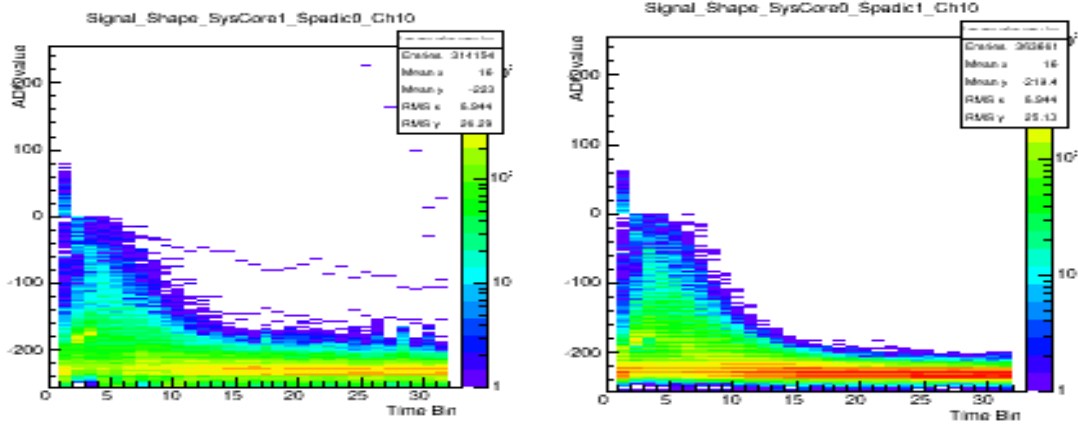


Figure 7.13: Grounding scheme of the TRD setup (Frankfurt and Münster) applied during the beam campaign 2015.

The SPADIC v2.0 is supposed to provide information from neighbor-triggered channels and combine them in one-hit message and record the peak of a pulse. The CBMnet in SPADIC v1.0 and 1.1 is replaced by a custom SPADIC-e-link protocol via GBTX (set of electrical signals between ASIC and GBTX). The GBTX will



(a) A noisy SPADIC signal

(b) A good signal

Figure 7.14: A good and a noisy signal of one channel of SPADIC. The noise level can be decreased by applying an appropriate grounding and a good configuration of the SPADIC.

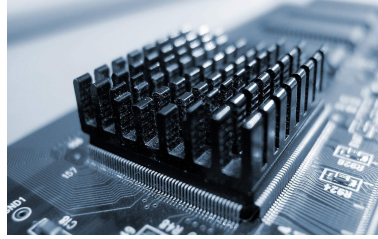


Figure 7.15: A heat sink radiator is pasted on an electronic chip [88].

be used instead of SysCore as an interface between FEB and DAQ. The triggering of epoch markers are not needed in SPADIC v2.0 any more as the clock signal is generated by the chip of the GBTX. The ADC sampling rate is reduced from 25 to 16 MHz in SPADIC v2.0 due to the clock frequency restrictions of GBTX [87].

## 7.2 SysCore v3.1

SysCore v3.1 is a universal Read-Out Controller (ROC) and a data processing board which is used as an interface between the Front-End Boards (FEBs) and the DAQ (FLIB and FLES) system. The Field-Programmable Gate Array (FPGA) used in the SysCore v3.1 board is a Xilinx Spartan-6 SRAM. Two partially popu-

lated FPGA-Mezzanin Card (FMC) connectors are implemented for efficient FEE data acquisition and three single-port Small Form-factor Pluggable (SFP) connectors are embedded for up to 3.2 Gbps communication. A jitter cleaner for the clock distribution across multiple boards, a mini USB interface for programming and data transfer, 12V/48V power supply, two Pmod connectors for quick module plugging, a JTAG connector as well as plenty of LVDS I/O pins are integrated on the board. The SysCore v3.1 can be reset by short-circuiting the two pins 1+2 on the LVDS\_ IN header for laboratory usage. It is also possible to reset it remotely. Figure 7.16 shows the SysCore v3.1 and its different components [89].

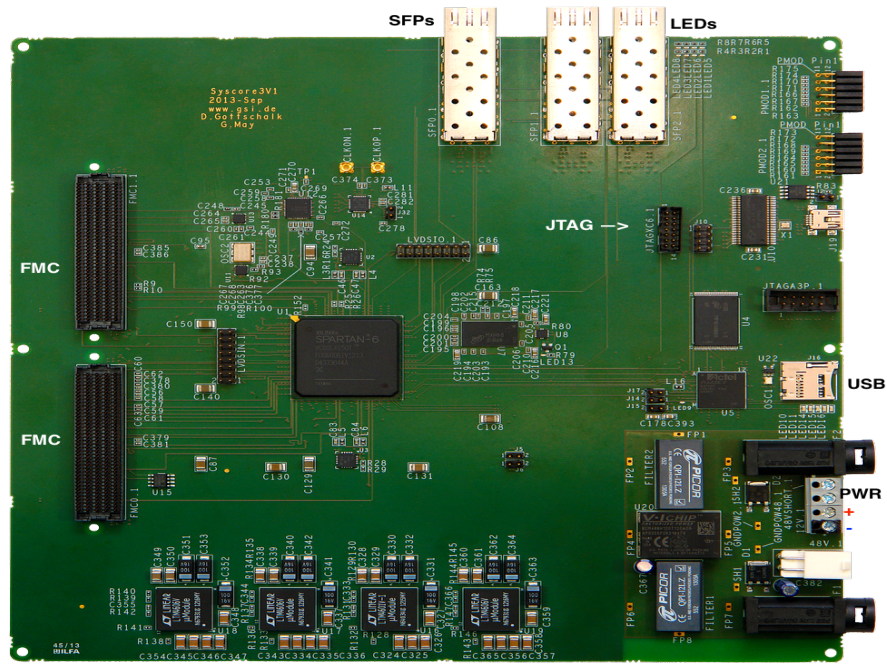


Figure 7.16: The SysCore v3.1 is used as an interface between the FEBs and the DAQ in laboratory and beam tests 2014 and 2015.

After each time the SysCore v3.1 has been reset or power-cycled, the FPGA should be programmed. Programming is possible via a Xilinx Programmer or via USB. For this, a local installation of Xilinx tools or LabTools is required.

When the SysCore v3.1 is powered on, the LED No. 13 (in the middle of the board) should be on. The meaning of the LEDs on the board is as follows:

- LED 1: PLL from optical link to FLIB has locked
- LED 2: cPLL for the Frontend Links has locked



- LED 3: daq\_active
- LED 4: Reset active
- LED 5: Link to the SPADIC No.1 active
- LED 6: Link to the SPADIC No.2 active
- LED 7: Link to the SPADIC No.3 active
- LED 8: optical Link to the FLIB active

For the TRD purposes, the LED No.1, 2, 5, and 8 must be on. If more than one SPADIC are connected, the LED No. 6 and 7 should be on per additional SPADIC. Figure 7.17 presents the LEDs on SysCore v3.1 which is connected to the three SPADIC FEBs.

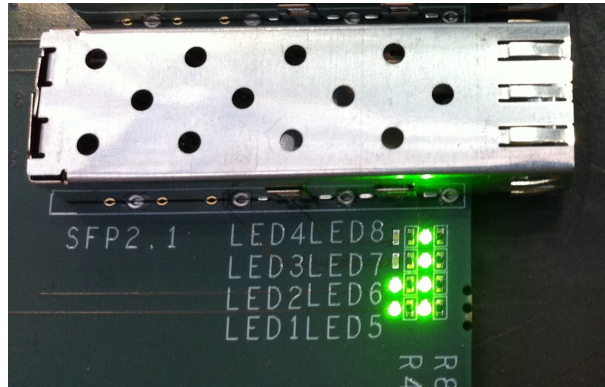


Figure 7.17: The 8 LEDs on the SysCore v3.1. Three SPADIC boards are connected to the SysCore v3.1, which relate to LED numbers 5, 6 and 7. For a readout-chain setup to be fully operated, the LED numbers 1, 2, (5 and/or 6 and/or 7) and 8 should be on.

## 7.3 FLIB

The FLES (First-Level Event Selector) is the central event selection system in the CBM experiment. It selects data for storage based on online analyses, including a complete event reconstruction. Time-slice building is part of FLES tasks and for this, detector data streams are partitioned into micro-slices and then data from all input links are combined (by time-slice building) to time intervals and distributed to the compute nodes. The partitioning will be done by the Data Processing Boards (DPB) as they are the last stage of the readout tree which has to contain subsystem specific components. Micro-slices are specialized containers covering a constant time frame of real time, which is the same for all subsystems [91].

FLIB is the FLES Interface Board which provides the optical interface to the DPBs as well as the interface to the FLES input nodes. The FLIB board is based on the commercial HTG-K7-PCIE from *Hitech Global*. It features a Xilinx Kintex-7 FPGA, a 8x PCIe 2.0 interface, up to eight 10 GBit/s links and optionally 8 GB of DDR3 memory. The FLIB receives micro-slices via optical links, prepares them for subsequent time-slice building and transfers the data via DMA (Direct Memory Access) to the host memory. Figure 7.18 shows the front view of the FLIB board. For installation and programming see [90].

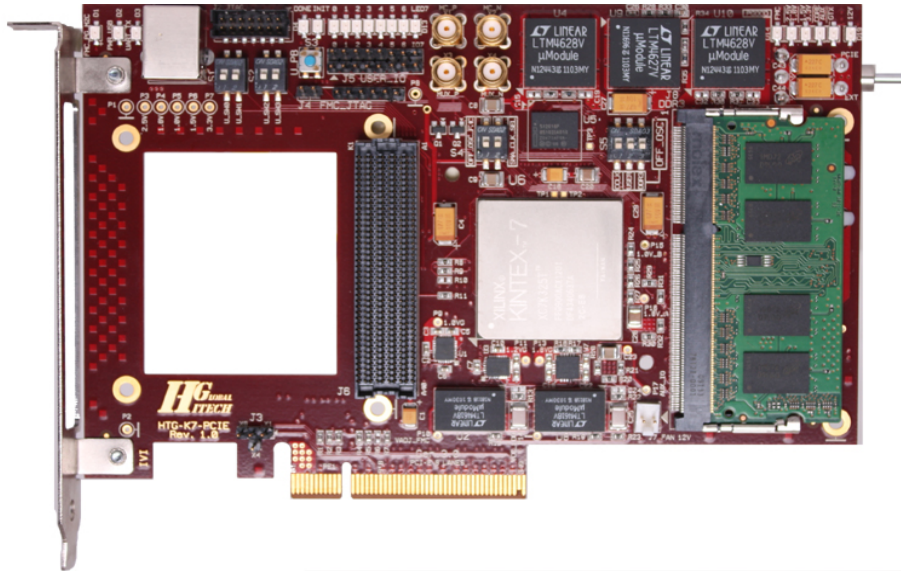


Figure 7.18: The FLIB is a FLES interface board which is connected directly to the PCIe (Peripheral Component Interconnect express). The FLIB connects to the SysCore via an optical link.



# Chapter 8

## Test-Beam Campaigns

### 8.1 The Test-Beam Campaign in 2014

Two carbon frame prototypes of TRD (from IKF) with amplification region thicknesses of (3.5+3.5 and 4+4 mm) were used in the test-beam campaign at the CERN-PS in 2014. The aim was to test new prototypes developed in 2014 at the IKF with the real-size dimensions of  $58 \times 58 \text{ cm}^2$ , thin amplification regions and alternating wire plane. Analyzing the gain stability,  $e/\pi$  separation and position resolution for momenta up to  $p = 6 \text{ GeV}/c$  were part of the plan.

The test-beam campaign was performed in the experimental area T9 of the CERN-PS. Coming from the PS accelerator the incoming proton beam hits a target which then produces the particles for the T9 beam line (see Fig. 8.1). Proton-beam collisions with the target can provide a variety of particles, e.g. electrons, positrons, muons, pions, kaons and anti-protons. The T9 beam line used for the experiment is therefore, a mixed hadron and electron beam which can deliver either positively or negatively charged particles with momenta between  $0.5 \text{ GeV}/c$  and  $10 \text{ GeV}/c$ . The beam is delivered uniformly in time over a burst of 0.4 seconds. For a positively charged beam at a momentum of  $10 \text{ GeV}/c$  a maximum particle rate per burst of  $10^6$  is achieved, however, it decreases for lower energies. The rate is lower for the negative beams. The characteristics of the beam then, in principle, allows a measurement of the  $e/\pi$  separation.

As shown in Fig 8.1, the primary beam collides with the target before it enters the secondary T9 beam line area. This target has always a core of light material, for example aluminium, beryllium or tungsten, allowing for different

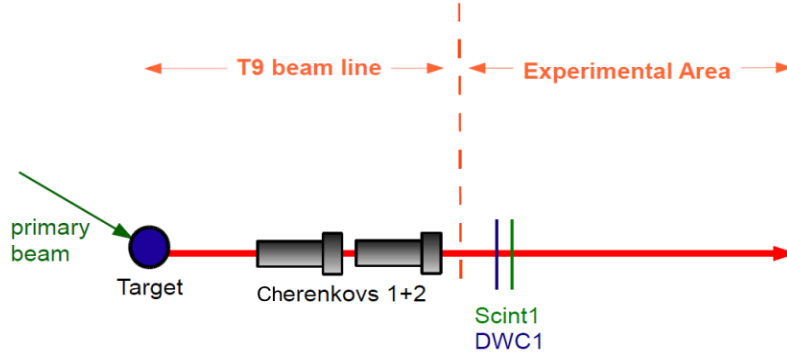


Figure 8.1: The setup of the T9 beam line [96]. The incoming proton beam (green arrow) from the PS accelerator hits on a target and thus produces the particles for the T9 beam line. Two Cherenkov counters, one Delay Wire Chamber (DWC) and one Scintillator counter (Scint) are part of the setup of the beam line.

electron components in the beam. Two Cherenkov counters are part of the setup, but can be left empty (i.e. without gas) if it is requested. In this case, they would not interfere with the properties of the beam. Each Cherenkov counter consists of a Cherenkov threshold selector and a photomultiplier. The Delay Wire Chamber (DWC) is a MWPC tracking device which is part of the setup of the beam line. The DWC provides a determination of the beam position by measuring the time between the particle passage and delay of the chamber signal which is measured via a delay line. The delay measures the distance between the particle and the wire. When charged particles pass through certain materials, e.g. certain plastics with specific additives, they produce scintillation light. By setting up two or more scintillator counters in a row, one can measure the time it takes the particles to travel from one scintillator to another or simply count the arriving particles (by only one scintillator counter) [96].

The CBM CERN-PS test-beam at T9 was scheduled from Nov. 12th until Nov. 26th (14 days) 2014. In total, 888 GB of raw data in 84 successful runs at different beam energies up to 6 GeV were saved by the TRD groups. The beam test was performed together with prototypes for the RICH and the TOF CBM detector subsystem, and with three TRD prototypes developed by the Münster group, as well as two TRD modules from Bucharest. All TRD prototypes from Frankfurt and Münster were equipped with SPADIC v1.0 and used SysCore v3.1 and FLIB as the DAQ system, while the Bucharest group used FASP as the readout for their TRD prototypes. A radiator made of polyethylene foam foil was used for both Frankfurt prototypes in the test-beam in 2014. Figure 8.2 shows a sketch of the CBM test-beam setup in 2014, and Fig. 8.3 represents the corresponding setup in

the cave.

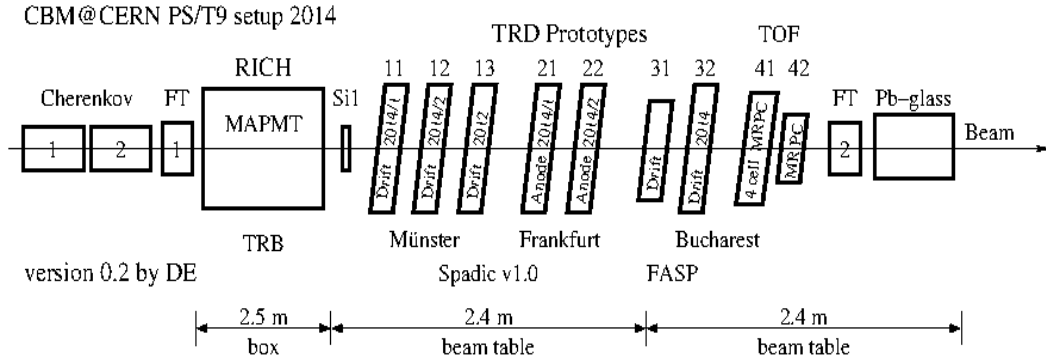


Figure 8.2: Sketch of the test-beam setup in 2014. The two prototypes from Frankfurt are between the three prototypes from Münster and the two prototypes from Bucharest. Frankfurt and Münster prototypes were equipped with SPADIC v.1.0 FEB and the Bucharest group used the FASP readout. The beam passes from left to right through two Cherenkov counters, the RICH detector, TRD prototypes, TOF detectors and the lead glass. Two Fiber Tracker (FT) and a Sintillator (Si) are also placed in the setup.

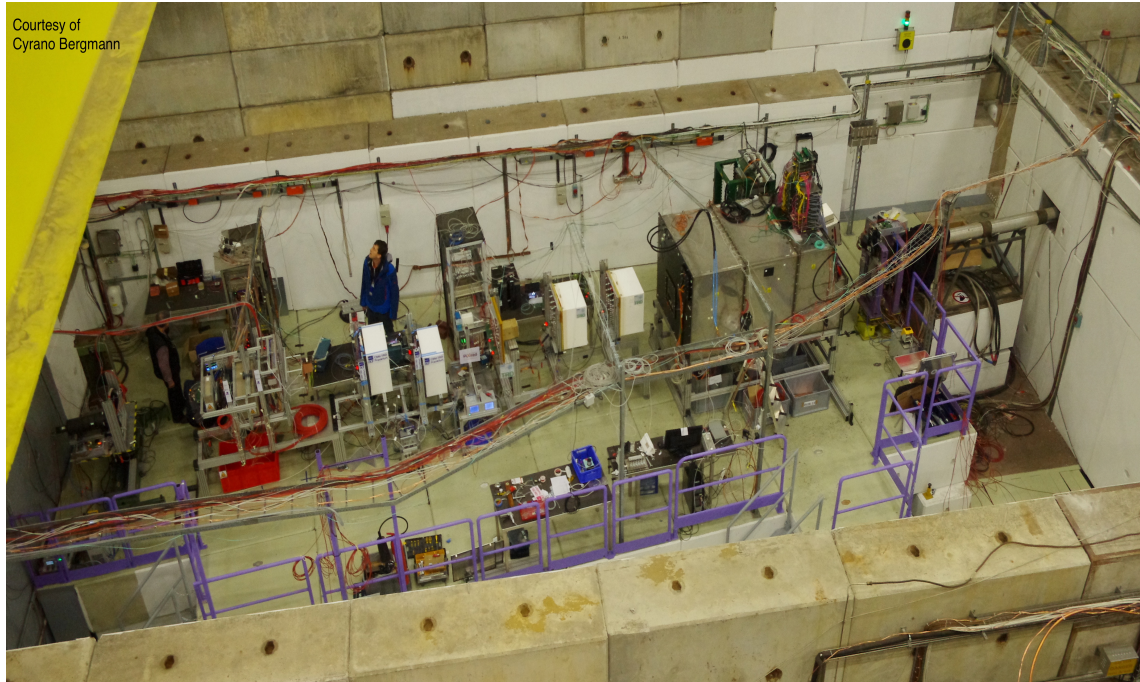


Figure 8.3: The view in the cave with the setup at the CERN-PS-T9 in 2014. The beam direction and the order of the setup in this figure are in the opposite direction ( $180^\circ$ ) to the Fig. 8.2.

The beam goes through the RICH detector after passing two Cherenkov counters and a Fiber Tracker (FT). The Cherenkov counters, together with Pb-glass calorimeter, are used as reference particle identification subsystems, which still are not included in the FLES readout. The Pb-glass calorimeter is a detector that measures the energies and positions of the particles. The FT and the Scintillator (Si) are used as the trigger detectors. The TRD prototypes were placed between the TOF and the RICH detector followed by a scintillator. The two-digit numbers on top of the detectors in Fig. 8.2 are used to distinguish the FEBs for each detector and to separate the data collected by each of them. The first digit indicates the detector group and the second digit specifies the number of the corresponding detector. The Münster group participated with two prototypes developed at the IKP in 2014 and one prototype developed in 2012. The TRD prototypes from Münster and Bucharest all included a drift region and normal wire planes. Both prototypes from Frankfurt included an alternating wire plane without drift region, as developed at the IKF in 2014. Figure 8.4 shows a close-up view of the Frankfurt prototypes.

The readout chain shown in Fig. 7.1 was used for both Frankfurt and Münster prototypes. One single-FEB SPADIC v1.0 was used for each Frankfurt prototype (see Fig. 8.5 left). The SPADICs were then connected to the SysCore v.3.1 and consequently, to the FLIB-DAQ. All TRD prototypes were supplied by a WIENER<sup>®</sup> Mpod HV/LV power supply (see Fig. 8.5 right). The HV for the Frankfurt prototypes was adjusted between  $V = 1300$  V and  $V = 1450$  V, which were set specifically for each run. All TRD prototypes were served with a gas mixture of Xe/CO<sub>2</sub> (80/20). The front-end board of one of the Frankfurt prototypes (No. 22 in Fig. 8.2) was problematic during the whole beam time. Therefore, no useful data was available for prototype 22. Consequently, the data were collected only for one prototype (no. 21). The prototype (no. 21) has a 3.5+3.5 mm amplification region and a pad plane as shown in Fig. 6.9.

An online monitoring system (see Figs. 7.11 and 7.12) based on ROOT<sup>1</sup> was used. The SPADIC software package (see Fig. 7.9 and Fig. 7.10) was applied to configure the FEBs and to adjust the baseline of the signal in each channel of the SPADIC v1.0. A self-trigger (no global trigger) mode was selected for all runs and adjusted to different values for the two thresholds (Th1 and Th2).

---

<sup>1</sup>An object-oriented framework based on C++





Figure 8.4: The two Frankfurt TRD prototypes used in the CERN-PS test-beam in 2014. A polyethylene foam foil radiator was used for both Frankfurt prototypes.

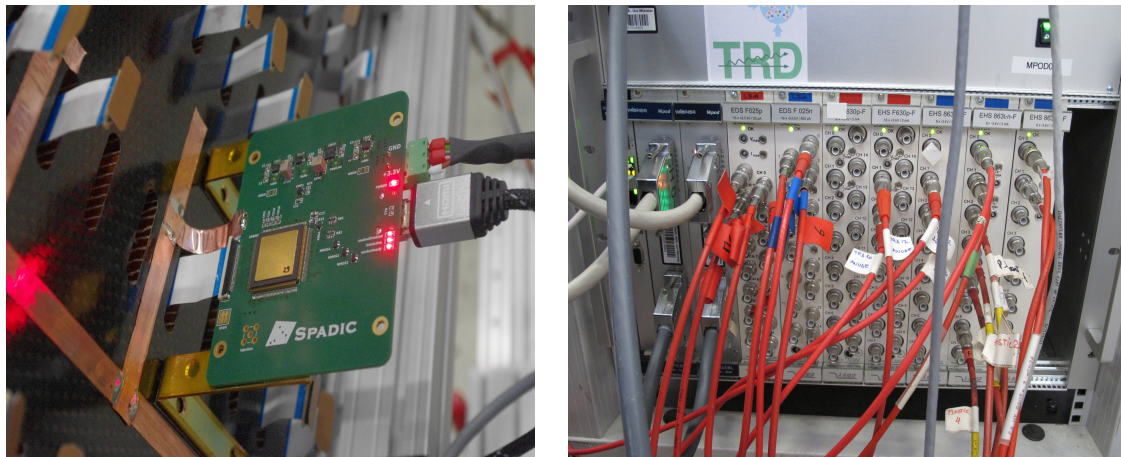


Figure 8.5: Left: Each Frankfurt TRD prototype was equipped with one single-FEB SPADIC v1.0. The SPADIC used for one prototype (no. 22) was problematic during the beam time making the prototype inefficient for data collection. Right: The WIENER® Mpod HV/LV supply used in the CERN-PS test-beam in 2014 to supply all TRD prototypes.

## 8.2 The Test-Beam Campaign in 2015

The test-beam campaign in 2015 took place at the CERN-Super Proton Synchrotron (SPS). The test-beam was scheduled for 6 days between November, 25th and December 1st. The aim was to test a TRD prototype (see Fig. 6.11) with alternating wire plane in an high-rate beam and analyze the stability of the prototype when different high voltages were applied and also to test the modified SPADIC v1.0 and analyze the collected detector signals. The beam campaign was performed at the H4 beamline (North area) of CERN, where a Pb-beam is delivered and impinged on a Pb target. This accelerator has the capability to deliver secondary beams with momenta from 10 to 400 GeV/ $c$ . The beam intensity reaches values up to  $1 \times 10^7$  Pb.

The TRD prototype developed at the IKF in 2012 was amended and segmented into 13 HV inputs to tolerate the high-rate beam at the CERN-SPS. The prototype has an amplification region of  $3.5+3.5$  mm and outer dimensions of  $59 \times 59$  cm<sup>2</sup>. The Münster group participated with one TRD prototype ( $3.5+3.5$  mm amplification region and 5 mm drift region, applying  $U_a=1850$  V on the anode wires) and the Bucharest group with three TRD prototypes. One TOF detector system was included in the test-beam setup. Figure 8.6 shows a sketch of the test-beam setup and Fig. 8.7 presents a photograph of the test-beam setup in the cave at the CERN-SPS.

The Frankfurt and Münster prototypes (position 4 in Fig. 8.6) were placed beside the beam line direction and behind the TOF detector system (position 1 in Fig. 8.6). Three TRD prototypes from Bucharest were located diagonal to the beam line direction (position 2 in Fig. 8.6). The Pb target is shown at position 8. The distance between the target and the Frankfurt prototype was 6 m and the distance between the Frankfurt and Münster prototypes was 0.5 m. The Frankfurt and Münster groups used the modified SPADIC v1.0 as FEB (left panel in Fig. 8.8), and SysCore v3.1 and FLIB as the readout chain, while the Bucharest group used the SPADIC v.1.0 only for one prototype and the FASP ASIC as a readout for the others. A gas mixture of Ar/CO<sub>2</sub> (80/20) was used for all TRD prototypes. In total, 41 GB of data in 57 runs was registered. The right panel in Fig 8.8 shows the front view of the TRD prototype from Frankfurt.

A WIENER<sup>®</sup> Mpod was used for HV/LV supply. Different high voltages from  $V = 1350$  V up to  $V = 1500$  V were applied to the 13 HV anode channels of the Frankfurt TRD prototype. Figure 8.9 shows the monitoring system of the Mpod power supply which was used to adjust the HV and currents for the 13 anode HV

channels of the Frankfurt (IKF) prototype, as well as the drift and anode voltages and currents for the Münster (IKP) prototype.

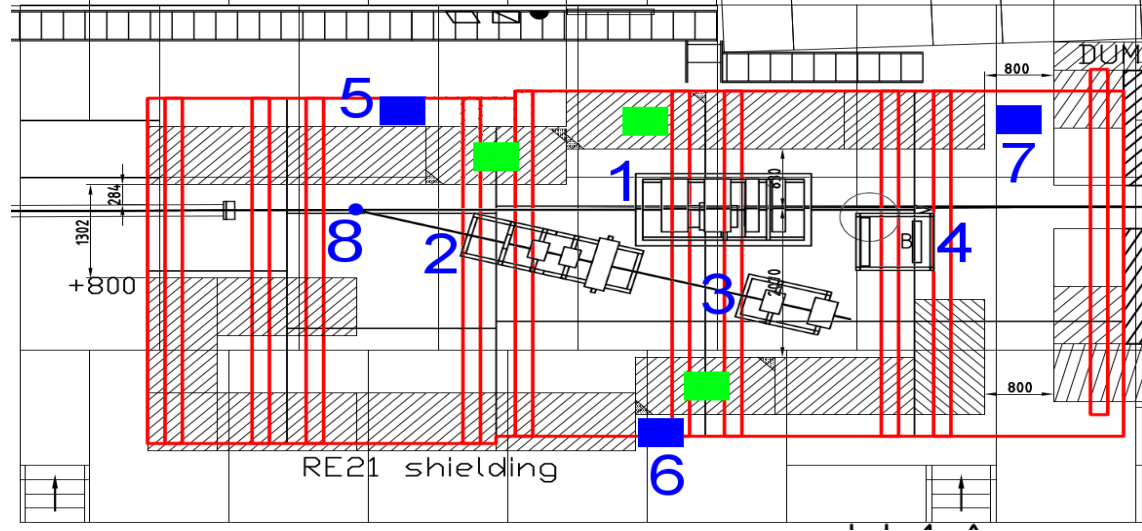


Figure 8.6: Schetch of the test-beam setup at the CERN-SPS in 2015. The beam impinges on the Pb target (8) from the left side of the figure. The Münster and Frankfurt prototypes (4) are behind the TOF detector system (1). The Bucharest prototypes (2) are diagonal to the beam line direction. Positions 5, 6 and 7 are the places where the electronics and power suppliers are placed for each detector system and 3 is another TOF system.

The TRD prototypes from Frankfurt and Münster were aligned with the height of the beam. SPADIC v1.0 showed some instabilities, however, after improving the grounding scheme of the chambers, FEBs, beam table, SysCore and power supply, it stayed stable in most of the runs during the beam test.

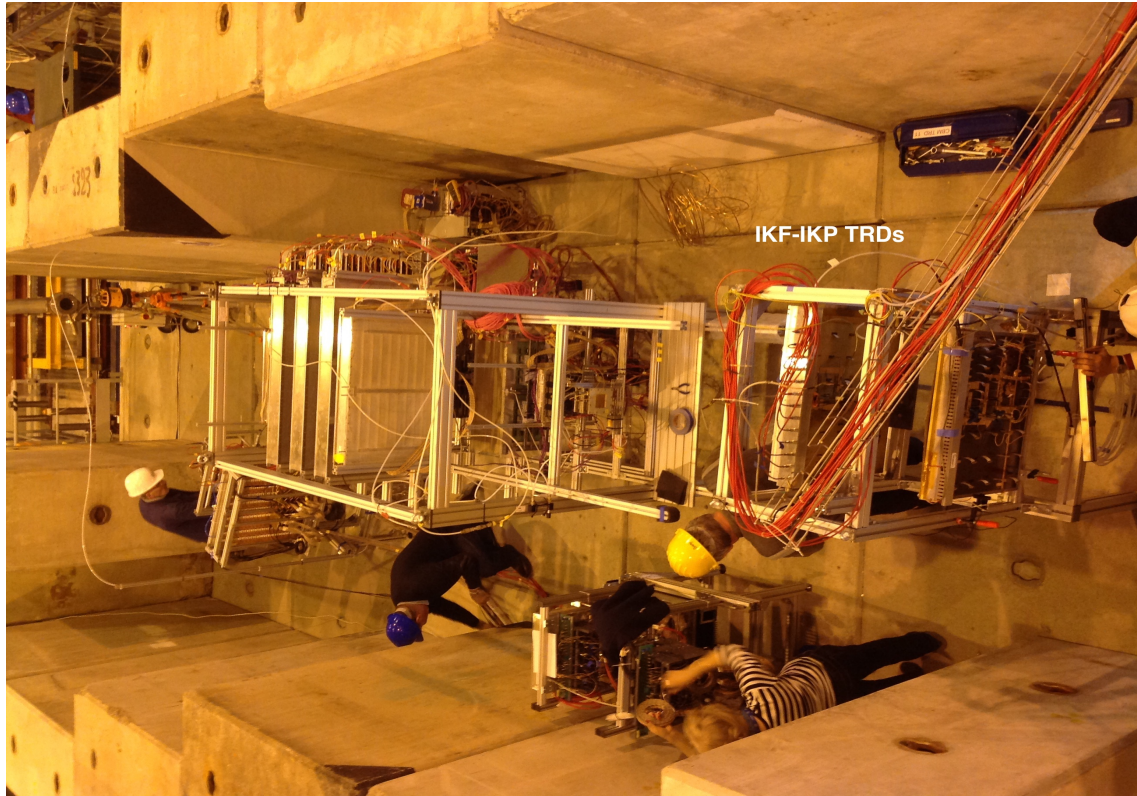


Figure 8.7: The upper view of the cave and the setup of the test-beam at the CERN-SPS in 2015. A TRD prototype with alternating wire plane and 13 HV channels from Frankfurt was tested. The Münster prototype is behind the Frankfurt prototype in 0.5 m distance and both are shown in the most right part of the figure. The direction of the beam is as the same as it is shown in Fig. 8.6.



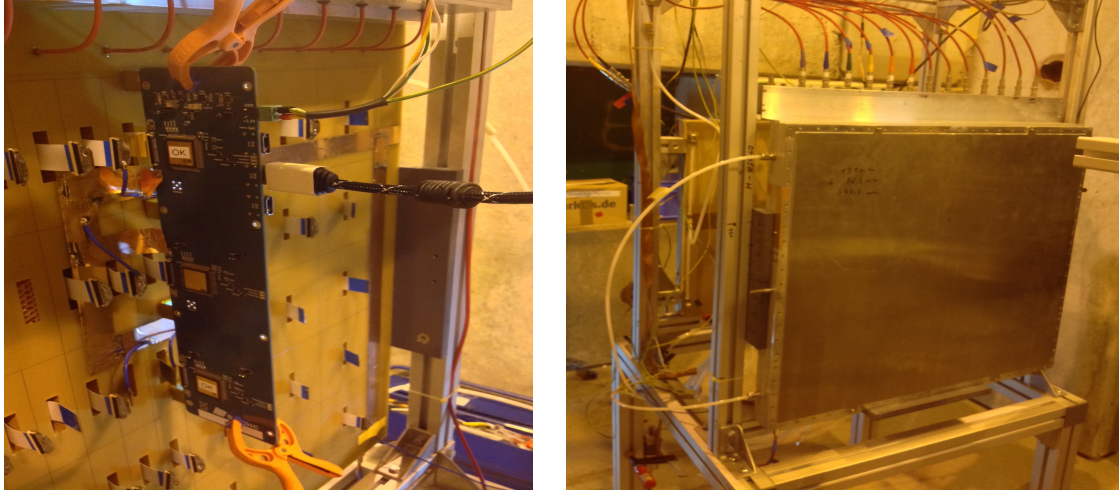


Figure 8.8: Left: A triplet SPADIC v.1.0 FEB connected to the IKF prototype. Right: The front view of the TRD prototype from Frankfurt with 13 HV cables.

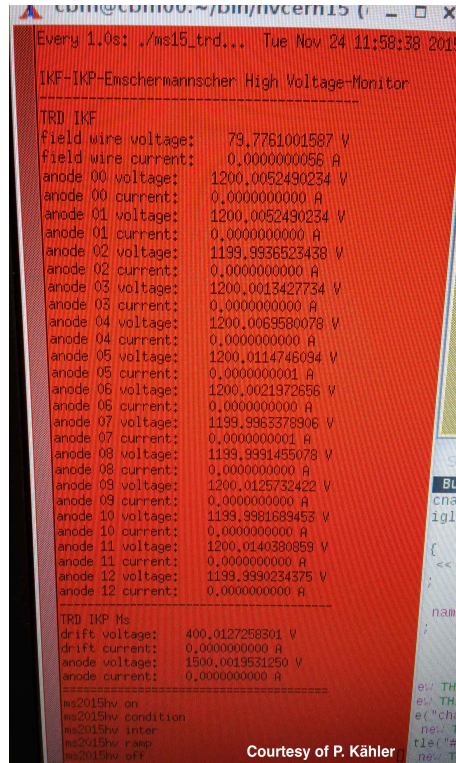


Figure 8.9: The monitoring system of the Mpod power supply used to adjust the HV and current on the 13 anode HV channels for the Frankfurt prototype.

# Chapter 9

## Performance Studies

### 9.1 SPADIC Data Analysis

The simulations, including detector responses, and physics analysis are being performed using FairRoot and CbmRoot framework. FairRoot and CbmRoot are fully based upon the ROOT system. Root is an object-oriented framework based on C++ that offers many features, which can be used in data analysis, data acquisition, event reconstruction, detector simulation and event generation.

To analyze the raw data registered by the SPADIC v1.0 (e.g to determine the position resolution and the energy resolution, see Sect. 5.3.1), the raw data and signals collected by the SPADIC v1.0 have to be modified and analyzed through a series of algorithms. The first two steps are pedestal compensation and clusterization.

The baselines (pedestals) of the signals in the 32 channels of the SPADIC v1.0 are not at the same pedestal (ADC value). To do the baseline correction (pedestal compensation), runs with the *Normal end message*, and *Self, Forced Neighbor (FN) and Self+FN triggered* were considered (runs with other *StopType* messages and Global trigger were excluded). In a first step, the first 1-3 time-bins in the raw SPADIC v1.0 signal, which do not contain any signal contribution yet were selected. The average over the ADC values of these three time-bins in each channel of the SPADIC v1.0 was calculated and then subtracted from the ADC values of all time-bins (time-bins 0,...,31) in a signal channel. This way the pedestal compensation was done channel by channel [99].

The clusterization algorithm determines clusters generated by the charged in adjacent pads in a row (one-dimensional clusterization). The clusterizaion is an essential first step to reach reconstruction and particle identification. The clusterization is done step by step as outlined in the following [99]:

- Determination of the time-stamp structure
- (Pre) clusterization
- Noise determination and reduction
- Signal integration

The first step is to find the time window for clusterization. For this, three pads (one self- and two neighbor triggered pads) are considered. To investigate the time-stamp structure, the time distances  $\Delta t$  between each message and the next two following or simultaneous messages from adjacent channels were determined. Then, the time distance distribution between each message with Self trigger and the next two following or simultaneous messages from adjacent channels with FN or Self+FN trigger flag is determined (see Fig. 9.1) [98, 99].

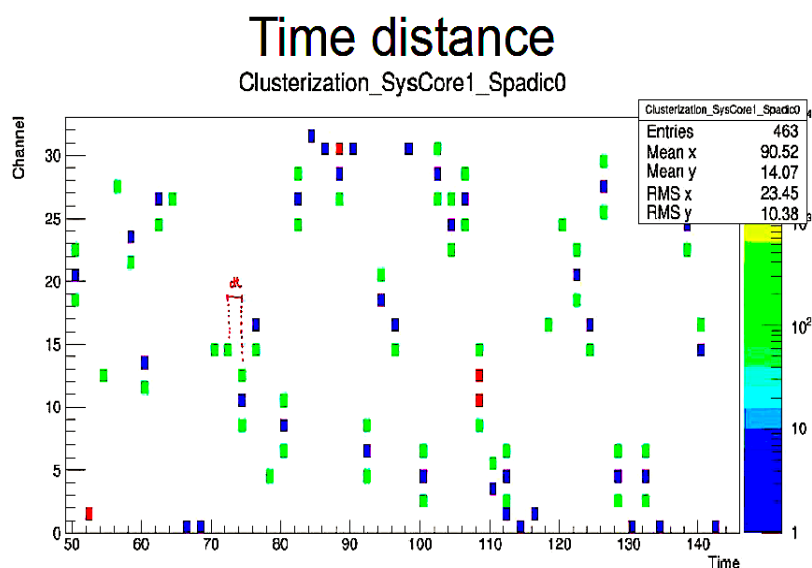


Figure 9.1: The time distance between the SPADIC v1.0 messages [98]. Blue, green and red dots correspond to Self, FN and Self+FN trigger channels, respectively. The time distance between two FN triggered in between 72 and 74 time-bin is shown as  $dt$ .

The SPADIC v1.0 signals can be distorted by noise. The signal has to be separated from the noise. This can be done by determining the noise level and

calculating its amplitude and subtracting the amplitude from the full event base. A detailed determination and subtraction of the noise in the SPADIC v1.0 signals is discussed in Sect. 9.2.

After subtracting the noise from the SPADIC v1.0 signals, a clean signal in each SPADIC channel can be obtained. The total energy of a cluster can then be obtained by integrating the amplitudes over all time-bins in all SPADIC channels that belong to a cluster (see Fig. 6.12).

The size of the cluster is determined by the number of different pads contributing to a cluster (see Fig. 9.6). Clusters are formed by the charges measured on several pads in a row on the pad plane. One pad can be triggered either by itself (self-triggered) or by its neighbor pads (neighbor-triggered). We called the self triggered Primary (P) and neighbor triggered as Forced Neighbor (FN) triggered pad. Some clusters showed only a P-triggered and one FN-triggered pad, which means that the two pads are at the edge of the pad plane and therefore, there is no neighbor pad on the other side of them. Clusters containing only P-triggered or only FN-triggered pads were recognized and removed as they were not efficient for data analysis (they are generated either by one pad in the edge of the pad plane or in the latter case by artifacts of the electronics).

## 9.2 Performance Studies with the Test-Beam at the CERN-PS in 2014

### 9.2.1 Pad Response Function

The measurement of the pad response function is performed by applying the baseline correction method mentioned in Sect. 9.2 and by using the cluster finder. The baseline was corrected in signals from both, self-triggered and neighbor-triggered, pads (see Figs. 9.2 and 9.3). The signals measured at higher beam momenta are larger, although their spectras show correlated noise. The measured signals at lower beam momenta are shorter, however, approximately the same noise magnitude ( $\sim 5$  ADC values) is observed. The noise generated by the electronics is added to the pure signal generated by a charged particle inside the detector and therefore it is important to identify the noise and subtract it from the pure signal. To detect how often the noise occurs and to have a better comprehension of the noise level, the noise correlated signal is divided into two time-bin groups (0-15 and 16-31). To determine the noise level, the difference between the two maxi-

imum ADC values in each group was calculated (see Fig. 9.4). A smaller difference between two maximum ADC values indicates a more noisy signal. The condition for a noise event is:

$$|\text{ADC}_{\text{max1}} - \text{ADC}_{\text{max2}}| < 3 \quad (9.1)$$

For a better comparison with the noise amplitude level, the noise signals of the two runs which are recorded at the lowest and the highest beam momenta (run 1045 at 0.5 GeV/ $c$  and run 1079 at 3 GeV/ $c$ ) were plotted (see Fig. 9.5). While in run 1045, a small rate of fluctuation is seen, run 1079 shows a sinusoidal larger fluctuation, which indicates a significant amount of noise level with a highest amplitude of 25 ADC values. After detecting the noise level and its amplitude, one can subtract it from the full event base [98, 99].

Equations 5.11 and 5.12 can be used to reconstruct the hit (track) position of a measured charge distribution. After clusterization, the position of the original hit was reconstructed and then the total charged seen by one primary pad and two neighboring pads was calculated. The integral of the ADC values was calculated to yield the total charges  $Q_i$  (see *Pad Response Function* and *Track Position* section in Chap. 5). Consequently, the Pad Response Function (PRF) is calculated after taking the clusterization into account. Figure 9.7 shows the PRF for the pad plane of  $w = 6.75$  mm of the prototype used in the CERN-PS test-beam in 2014.

The Pb-glass calorimeter and the two Cherenkov sub-detectors are important for the Particle IDentification (PID) performance analysis. As they have not been integrated in the FLIB/FLES DAQ, a further data analysis of the test-beam in 2014 was not feasible.

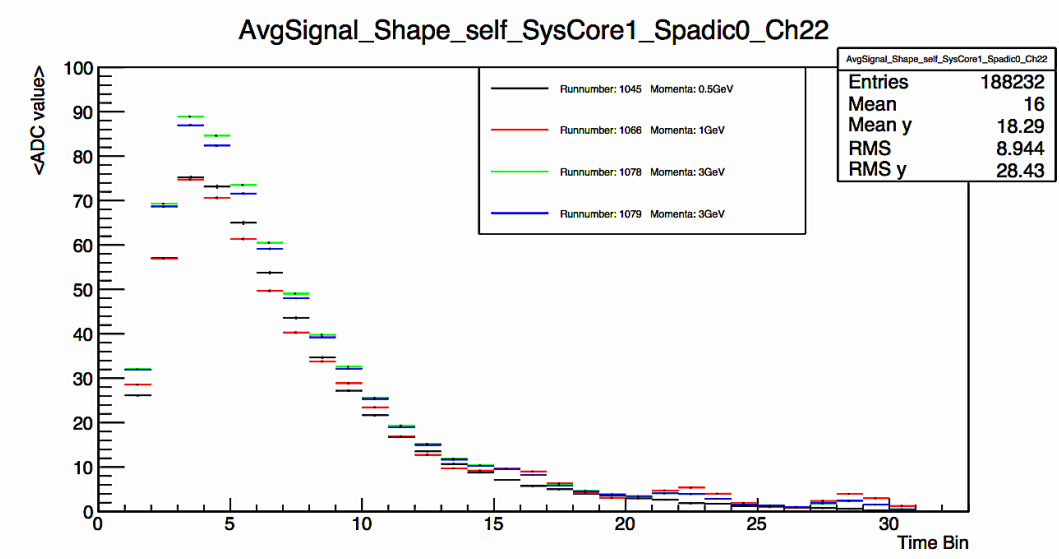


Figure 9.2: The baseline corrected signals for self-triggered pads measured at four different beam energies [98]. The signals from higher beam energies are larger but correlated with noise.

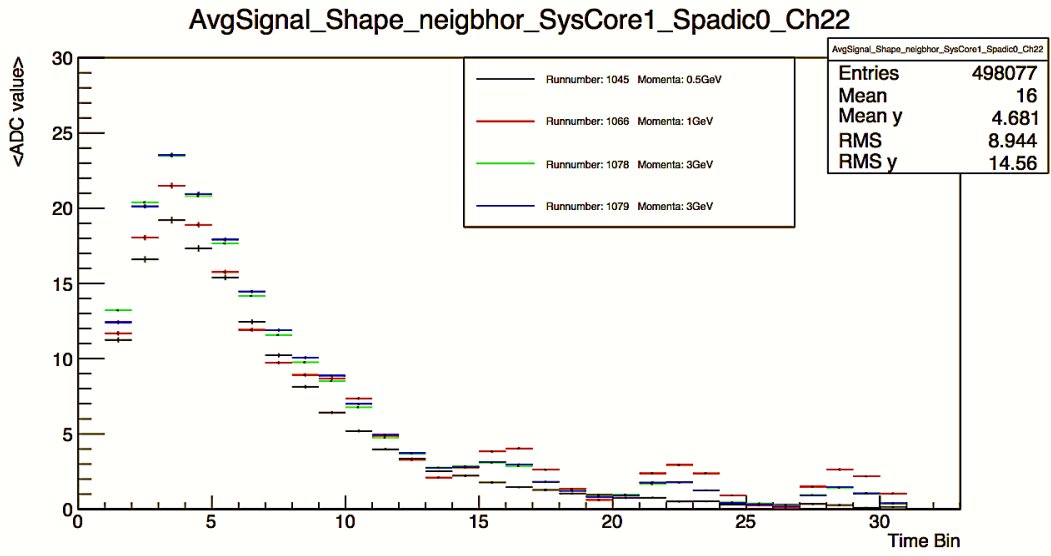


Figure 9.3: The baseline corrected signals for the neighbor-triggered pads at four different beam energies [98]. The signals are shorter in time compared to those of the self-triggered pads, however, the same magnitude of noise (approx. 5 ADC values) is visible.

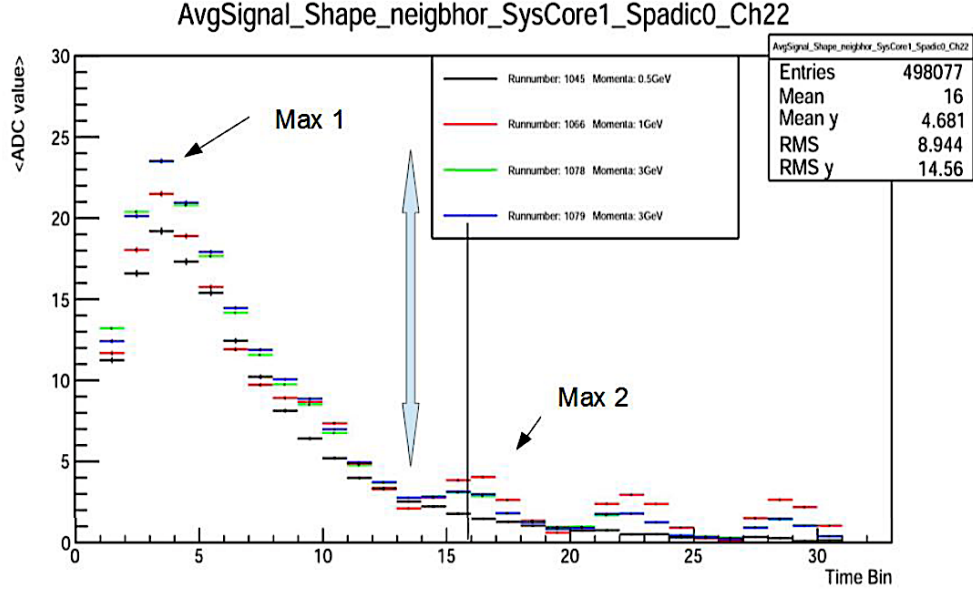


Figure 9.4: The signals were divided into two time-bin groups (0-15 and 16-31). The difference between two maximum ADCs in two groups was determined to have a better comprehension of the noise level and its occurrence frequency [98]. The lower difference between two maximum ADC values indicates a more noisy signal. A noise level with a maximum amplitude of 5 ADC value is observed.

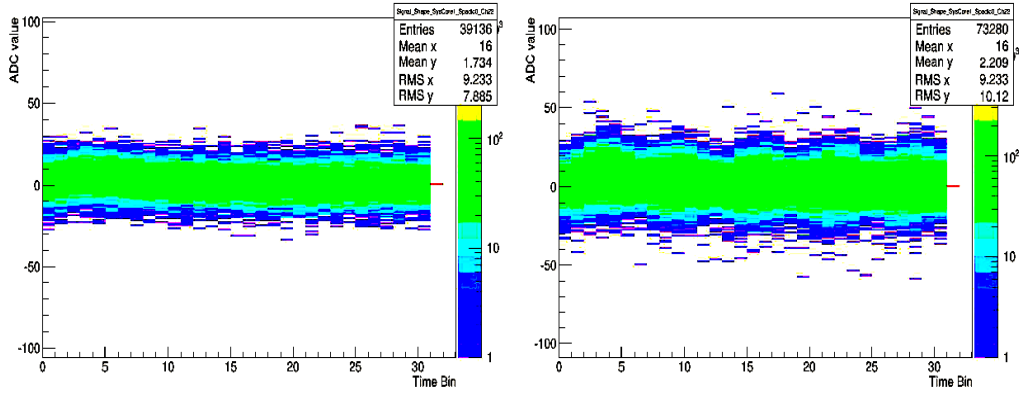


Figure 9.5: The noise signal of the two runs recorded in two different beam momenta [98]. Left: run 1045 at a beam momentum of 0.5 GeV/c shows a small fluctuation. Right: run 1079 at a beam momentum of 3 GeV/c shows a considerable sinusoidal fluctuation with a maximum amplitude of 25 ADC values.

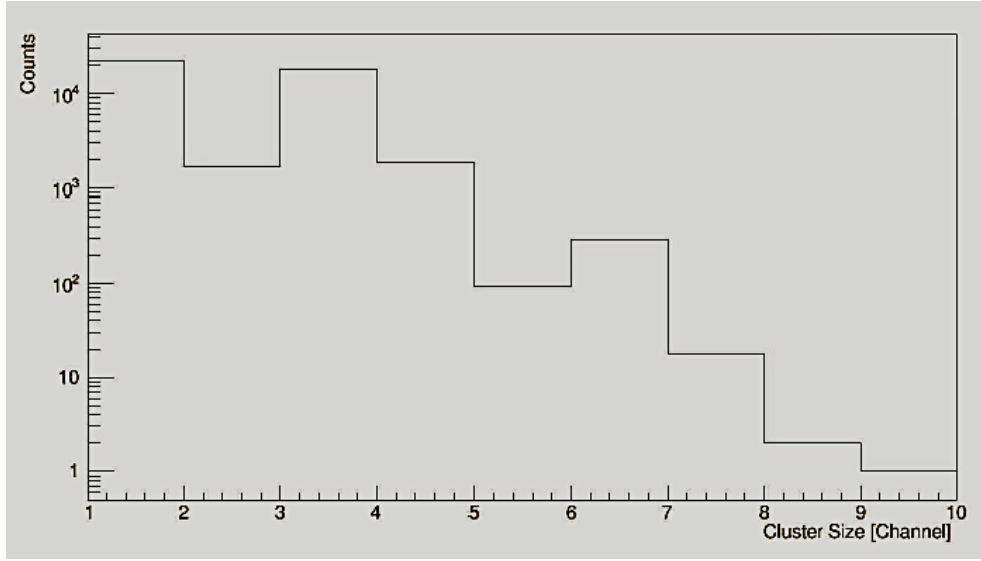


Figure 9.6: Histogram of the cluster size. It shows the number of triggered pads in one cluster in run 1045 [98]. The size of the cluster is defined by the number of pads contributing to a given cluster.

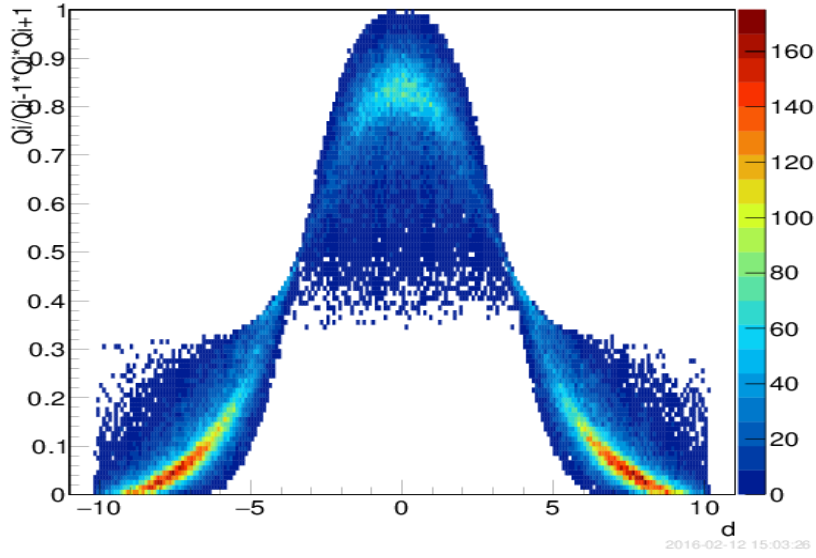


Figure 9.7: The pad response function for the pad size of  $w = 6.75$  mm of the prototype as determined in the test-beam 2014 at the CERN-PS [98].



## 9.3 Performance Studies with the Test-Beam at CERN-SPS in 2015

### 9.3.1 Current Measurements

A HV between  $U = 1350$  V and  $U = 1500$  V was applied to 13 HV-anode channels of the Frankfurt prototype. The stability of the 13 HV channels was monitored at different beam rates. Applying up to  $U = 1400$  V on the anode channels at a trigger rate up to  $10^3$  Hz/cm<sup>2</sup> and beam energy of 30A GeV all channels stayed stable. Figure 9.8 shows the current distribution in the 13 HV channels (channel no. 300-312) [100]. Channel no. 300 was the farthest channel away from the beam line, and channel no. 312 was the closest one, which explains a higher current level in the channels closer to the beam line.

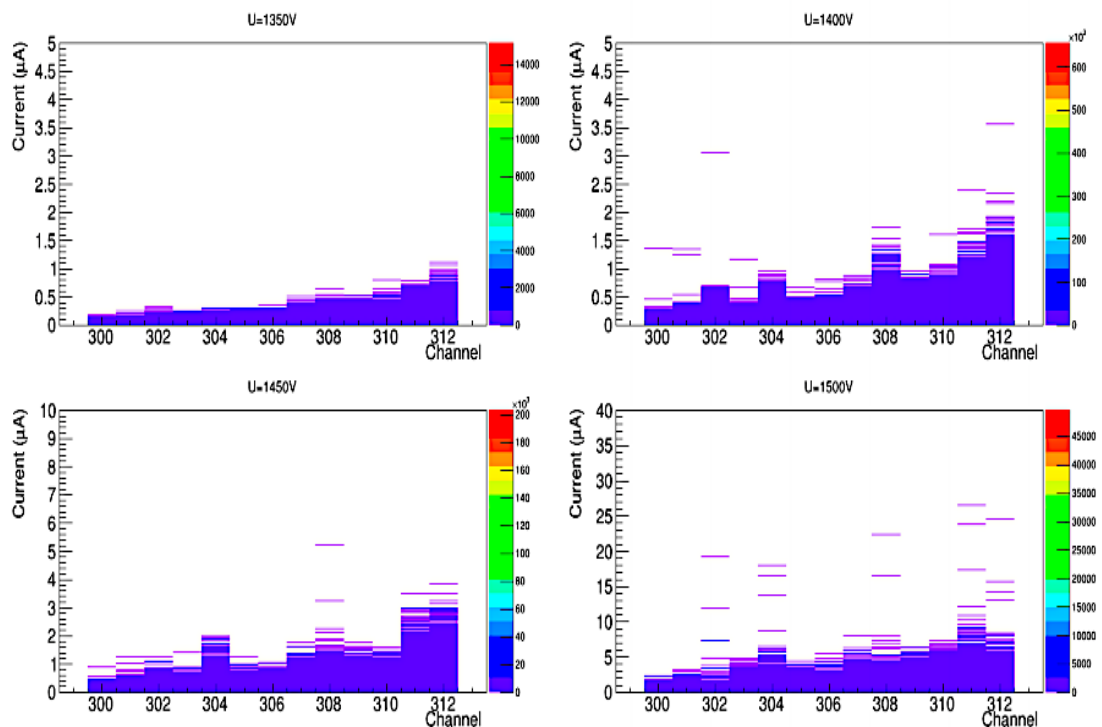


Figure 9.8: Current distribution in 13 HV channels in Frankfurt prototype applying 4 different high voltages [100]. Applying up to  $V=1400$  V all channels were stable.

The current of the channels also varied with the hit rates. Figure 9.9 shows

the dependence of the sum of the currents in the 13 HV channels on the hit rate [100]. The graph shows the integrated current of the 13 HV channels as a function of the number of 3 and 4-pad clusters, here denoted as the hit rate per  $\text{cm}^2$  of the active surface of the detector. To obtain the hit rate these numbers have to be divided by 3.5 (the average of 3 and 4-pad clusters). The graph shows that the current increases only moderately with increasing the hit rates.

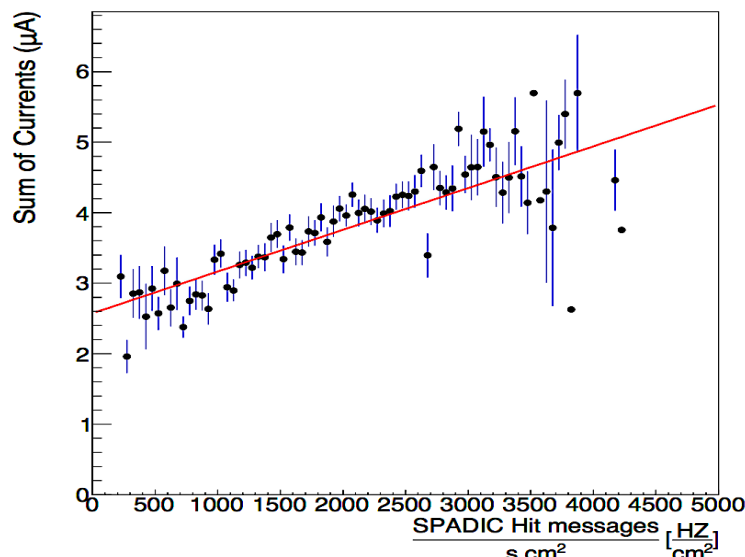


Figure 9.9: Sum of the current as a function of the cluster rate [100]. The current increases with increasing cluster rate.

The same pad plane was used in the Frankfurt and Münster chambers, which allows to correlate hits passing through the two detectors. The 3- and 4-pad clusters were used to analyze the coincidence of a hit in both prototypes. As both TRD prototypes were aligned to the target (see Fig. 9.10), the probability for a hit to fire the same pad rows in both prototypes (arrows 1 and 2 in Fig 9.10) is higher than the probability for a hit to fire different pad rows on two prototype pad-planes (arrow 3 in Fig. 9.10). This explains the higher hit coincidences shown in Fig. 9.11 compared to the hit coincidences shown in Fig. 9.12. Figures 9.11 illustrates a hit passing through the Frankfurt and Münster prototypes when it fires the same pad row in both prototypes and Fig. 9.12 presents a hit fires two different pad rows. If a hit fires a pad in the edge of the pad plane, it creates a 2-pad cluster as there is only one neighbor pad on one side of the triggered pad. Since the SPADIC v1.0 does not record 2-pad clusters, there are no hit coincidences in the position no. 16 of both prototypes in Figs. 9.11 and 9.12. The weak hits on the top of the Figs. 9.11 and 9.12 are due to the broken channels in the SPADIC v1.0.

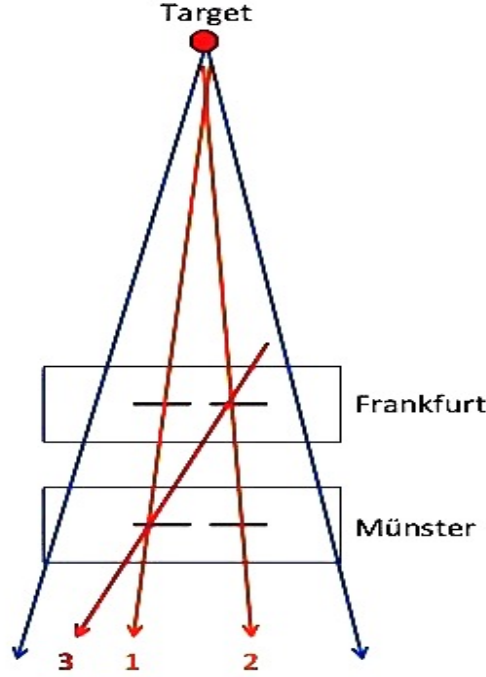


Figure 9.10: The two prototypes were aligned with the target. Therefore, the probability for the hits to fire the same pad rows in both prototypes (arrows 1 and 2) is higher than the probability for the hits to fire two different pad rows (arrow 3).

The hit coincidences were calculated using the cluster position on the pad. For this analysis, run no. 136 was selected. Figure 9.13 presents hits, which fire the same pad rows in both prototypes. This track hits the pad rows diagonally, which explains the small shift of the hit coincidences away from the diagonal in the right-top panel of Fig. 9.13 and makes the spectra shown in the lower panel of Fig. 9.13 wider. The lower panel in Fig. 9.13 shows the analysis to perform position resolution. They show the hit coincidences as a function of the pad width  $\Delta x$ , with (right) and without (left) correction. The correction has done to compensate for the effect of hits that fire the 2-pads in two prototypes not at the right angle (as already explained for the upper-right panel of Fig. 9.13). However, the width of the Gaussian distribution is dominated by the size of the beam spot (the beam had a diameter in mm) and the multiple scatterings in the detector material. As long as no reference detector was used in the test-beam in 2015, further position resolution analysis was not feasible and the calculated  $\sigma$  does not reflect a real position resolution of the detector.

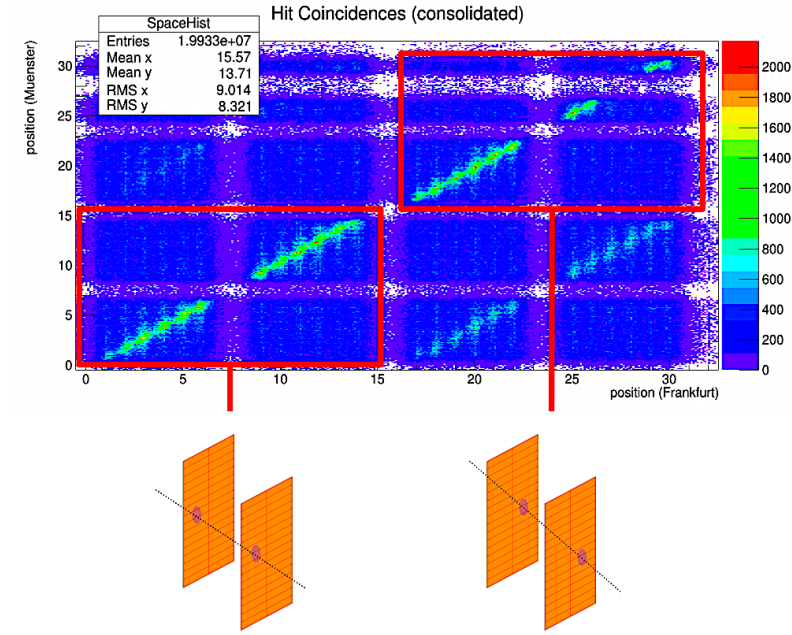


Figure 9.11: Position coincidence of hits in the Frankfurt and Münster prototypes [101]. The hit fires the same pad row in both prototypes.

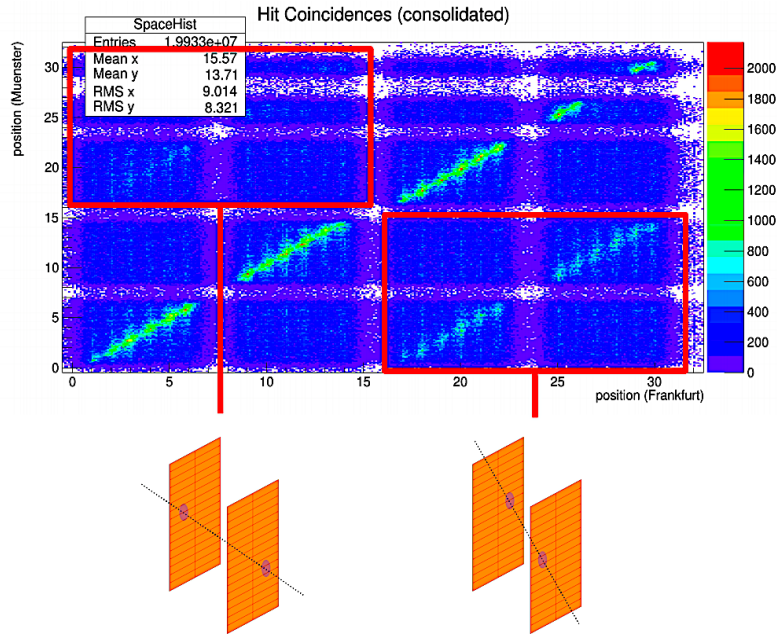


Figure 9.12: Position coincidence of a hit when it fires two different pad rows [101].

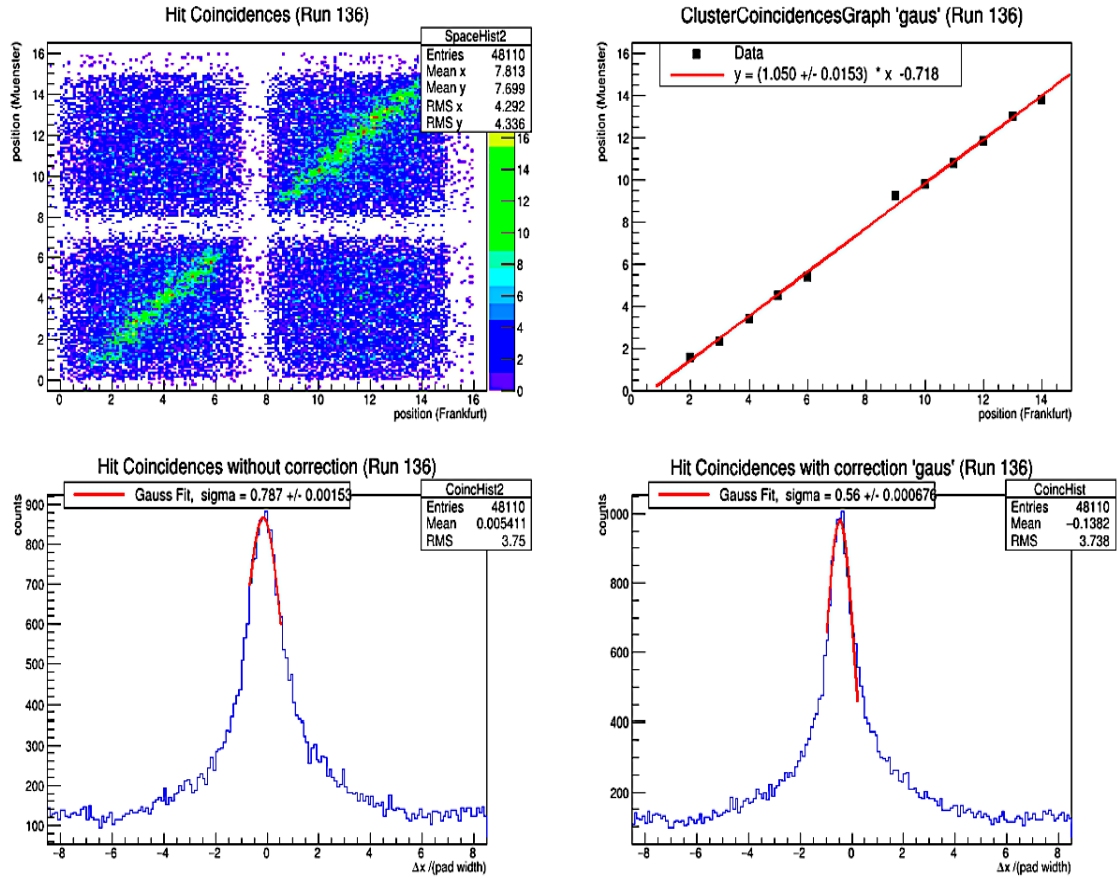


Figure 9.13: Hit coincidences [100]. Upper panel: a hit coincidence (left) and its mean position (right). The hit fired the same pad rows in both prototypes diagonally. Lower panel: analysis to perform the position resolution. Hit coincidence with a Gaussian fit and without correction as a function of pad width (left), and hit coincidences with a Gaussian fit and correction (right). Since the width of the Gaussian shape is dominated by the size of the beam spot and the multiple scatterings in the detector material and no reference detector was used, the calculated  $\sigma$  does not indicate the real position resolution of the detector.

# Chapter 10

## Further Developments

A standard full-size detector ( $95 \times 95 \text{ cm}^2$ ) with normal anode wire plane,  $3.5+3.5$  mm amplification region and 5 mm drift region has been developed in a cooperation between the IKF and the IKP. The prototype was tested in the test-beam campaign 2016 at CERN-SPS. Figure 10.1 shows a drawing (top view) of the full-size prototype and a photograph of the back panel is shown in Fig. 10.2. The production of 200 large and small modules ( $95 \times 95$  and  $57 \times 57 \text{ cm}^2$ ) of the TRD with the same characteristics (e.g. drift and amplification region, anode wire plane and the pitch between wires, etc.) is planned for the CBM experiment in SIS100 until the end of 2022. The installation of four layers of TRD is planned to start in the mid of 2023.

The newer version of the FEBs (for SPADIC v1.1 and SPADIC v2.0) are produced and tested in the laboratories and in the CERN-SPS beam-test in 2016. The SPADIC v1.1 is a debugged and improved version of SPADIC v1.0, but the firmware and the packaging are the same. The Charge Sensitive Amplifier (CSA), as well as the link and hit detector were improved in SPADIC v1.1. The SPADIC v2.0 is close to the ideal final version of the readout ASIC (SPADIC v2.1) for the TRD. The CBMnet (HDMI connector) is replaced by the STS-XYTER protocol (E-Link Interface), and the shaping time and sampling frequency are changed in SPADIC v2.0. The E-Link defines the data-transfer protocol between ASIC and GBTX. The sampling rate (shaping time) in SPADIC v1.0 was 25 MHz (80 ns), which is changed to 16 MHz (250 ns) for the SPADIC v2.0. There is no need for DLM for synchronization as buffering is not required any more in SPADIC v2.0. The configuration is unified and synchronized and also there is no need for the triggering of epoch markers. The absolute or differential threshold mode is still an option for the hit finder in SPADIC v2.0. Figure 10.3 shows a comparison between

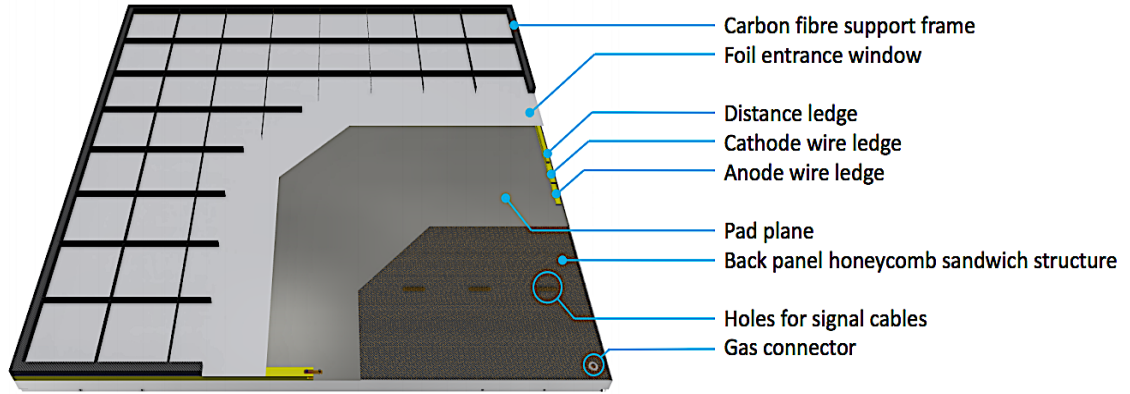


Figure 10.1: Drawing of the front view of the full-size TRD prototype with normal cathode wire plane, 3.5+3.5 mm amplification region and 5 mm drift region as planned for the outer parts of each layer of the CBM-TRD [102].

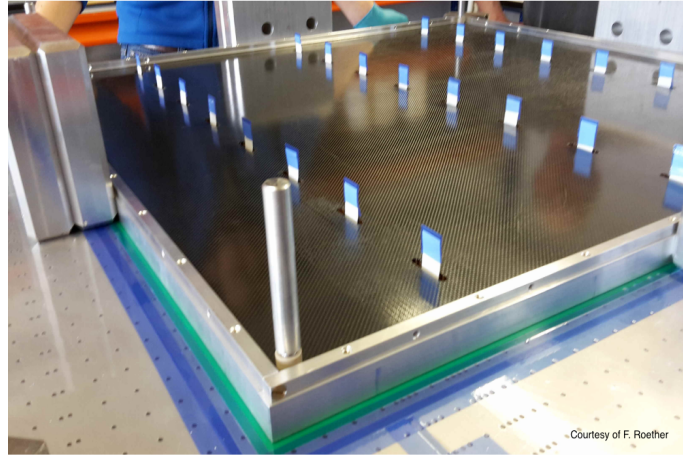


Figure 10.2: Rear view and the back panel of the full-size TRD prototype.

SPADIC v1.0 (left) and SPADIC v2.0 (right) [103].

The pad plane layout of the TRD was optimized to a minimum number of six module types. The TRD module type 3 will be further modified to reduce the FEB diversity. A readout chain, including FEB, GBTx, FLIB and electrical and optical interfaces will be used for CBM-TRD [104]. Figure 10.4 depicts the diagram of the CBM-TRD readout chain.



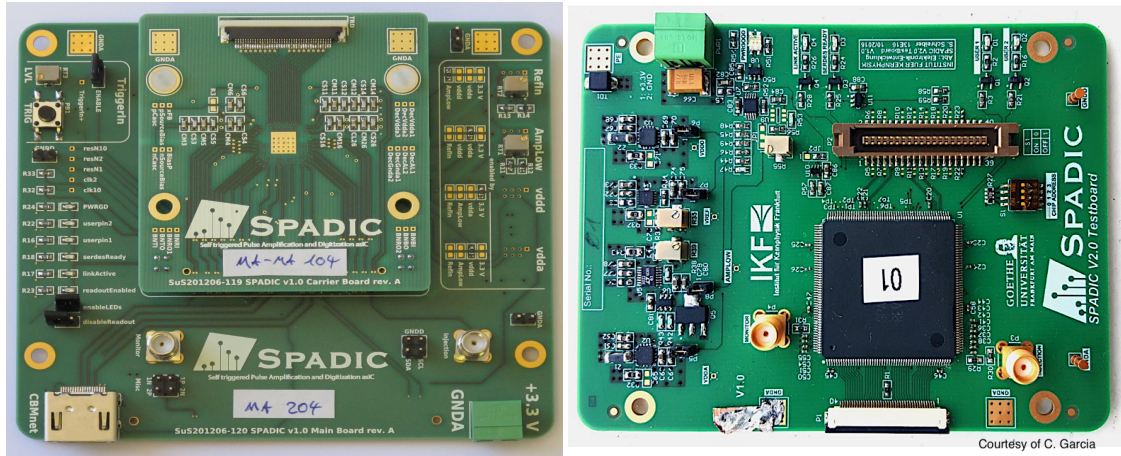


Figure 10.3: Right: SPADIC v.2.0. The CBMnet is replaced by E-Link as transfer protocol between ASIC and GBTx. Left: Double-FEB SPADIC v1.0 (2013 FEB version).

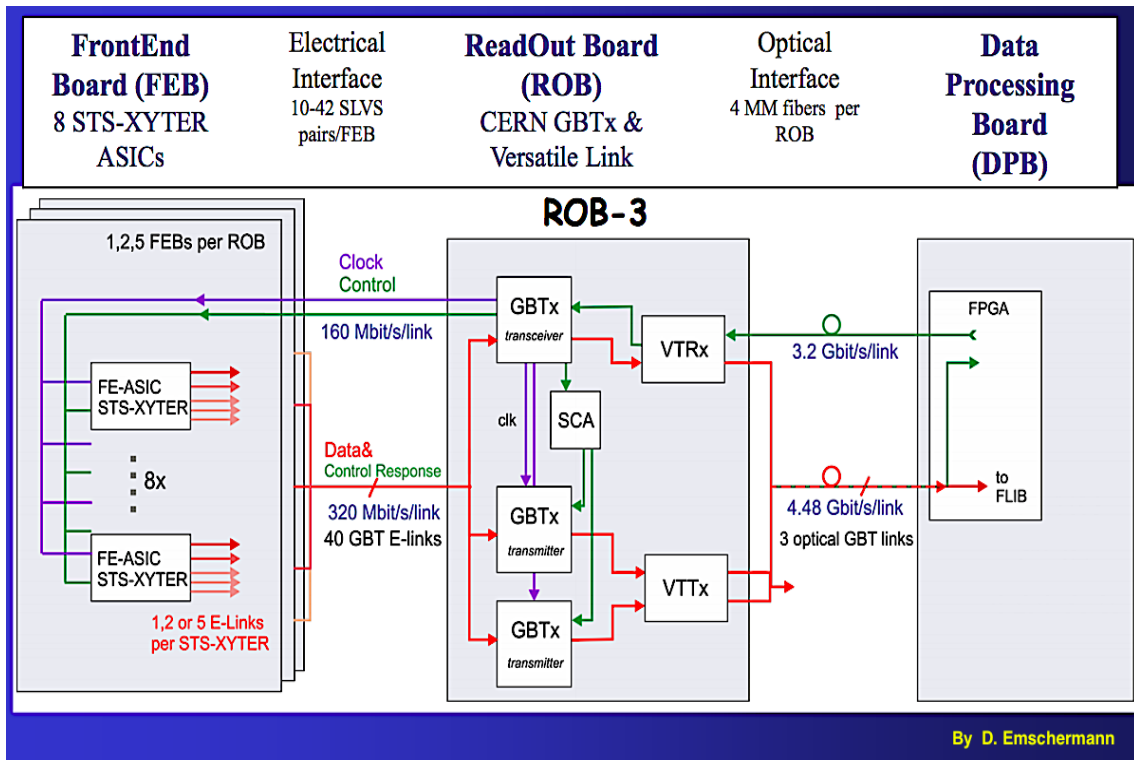


Figure 10.4: The readout chain diagram of the CBM-TRD. The readout is composed of three main parts (FEB, Read Out Board and Data Processing Board), which will be connected to each other with electrical and optical interfaces.



# Summary

Quarks and gluons as the basic constituents of QCD are confined in hadronic matter, which means they are bound together. The simplest examples are the mesons (quark-anti quark) and the baryons (3 quarks). QCD predicts a phase transition of hadronic matter into a hot and dense deconfined quark-gluon matter known as Quark-Gluon Plasma (QGP). The CBM experiment as part of the FAIR program will explore the QCD phase diagram in the region of high net-baryon densities using high-energy nucleus-nucleus collisions. TRD is part of the detector setup of the CBM experiment.

To fulfill the CBM physics objectives in the SIS100 beam energy range, a transition radiation detector is needed. It is crucial to study intermediate mass dileptons (dileptons in the mass range between  $m(\phi)$  and  $m(J/\psi)$ ), and  $J/\psi$  production. The TRD identifies electrons via their energy loss inside the detector gas volume and the detection of TR photons. It is also important for particle tracking in combination with the STS and the TOF. The TRD design parameters are defined by its pion rejection capability, charged particle identification, stability at high interaction rates and tracking capabilities. A pion suppression factor of 10-20 at 90% electron efficiency for  $p > 6$  GeV/ $c$  is required. The TRD for the CBM experiment at SIS100 has to be stable at interaction rates up to 10 MHz. For PID purposes, the TRD has to be able to distinguish fragments heavier than the proton. The gas volume inside the detector has to be short enough so that the charged particles drift faster towards the wires and generate signals (signal collection times below 0.3  $\mu$ s are required), and long enough to allow for a better TR absorption. The arrangement of the TRD between the STS and the TOF helps in the track matching. To keep the data rate and occupancy as low as possible, the pad granularity should be small enough. TRD will be used in both, electron and muon setups of the CBM experiment at SIS100. In the muon setup, the TRD will be used only for tracking and not for PID purposes.

To meet the requirements of the CBM physics objectives, several TRD prototypes with different design structures have been developed at the Institute for Kernphysik in Frankfurt (IKF). To develop a fast detector, a prototype with short amplification region and without drift region has been constructed. The detector was fast compared to a corresponding prototype with drift region, however, pressure differences between inside and outside of the detector led to deformations of the entrance window (cathode plane) and eventually deteriorated the electric field inside the detector and distorted the gas gain. To overcome this problem, an alternating wire geometry has been introduced. A wire plane of sense (anode) and field (cathode) wires in a row with a 2.5 mm pitch between them is placed between the entrance window (aluminum Mylar foil) and the pad plane. The alternating wire geometry was used in a small-size ( $58 \times 58 \text{ cm}^2$ ) prototype with the 3.5+3.5 mm amplification region. This prototype was tested in test-beam 2014 at the CERN-PS with a mixed beam composed of hadrons and electrons of momenta up to 6 GeV/ $c$  and a signal collection time below 0.1  $\mu\text{s}$  was achieved, while the gas gain remained stable. This prototype would be ideal for the inner parts of the TRD layers in a high-rate beam experiment, e.g. at the SIS300.

A large-size prototype (developed in 2012 at the IKF) was improved and segmented into 13 HV channels to sustain the high load at the CERN-SPS beam test in 2015. The current along the anode wires was measured during the test-beam 2015 and the stability of the prototype was analyzed. This prototype was stable when applying up to HV=1400 V on the 13 anode channels at a beam energy of 30A GeV and hit rate of up to  $10^3 \text{ Hz/cm}^2$ .

As a signal collection time below 0.3  $\mu\text{s}$  is sufficient for the SIS100 rates and since adequate TR absorption is desired, the final design of a 3.5+3.5 mm amplification region plus 5 mm drift region with the normal anode wire plane is planned for the TRD at SIS100. For this, a final large size ( $95 \times 95 \text{ cm}^2$ ) prototype with the planned design was developed and tested in a test-beam at the CERN-SPS in 2016.

Argon and Xenon are the optional choices as counting gas since they are not electronegative (they do not combine with electrons) and are dense (high Z elements), thus the energy loss of charged particles and the TR absorption are high.  $\text{CO}_2$  is used as a quencher with the mixture ratio of 15 - 20%. For the detector test in the laboratory and in the test-beams, argon is used due to its lower cost compared to Xenon. However, for the TRD at SIS100, a mixture of Xe/ $\text{CO}_2$  (85/15) is foreseen.

The pad plane layout of the TRD was optimized to a minimum number of six

module types in two geometries. Three types of FEBs (according to the number of ASICs on each one) and three types of Read-Out Board (ROB) are planned for the TRD at SIS100.

The first ASIC for the TRD (SPADIC v0.3) was developed in 2010 and was used in a test-beam at CERN during 2010-2013, together with an interface FPGA readout controller called SUSIBO. SPADIC v0.3 has 8 channels per chip and is able to shape a signal in 90 ns. SPADIC v1.0 has 32 channels per chip and has the capability of ion tail cancelation, base line correction, switchable polarity and neighbor channel triggering. The pulse shaping time in SPADIC v1.0 is 80 ns, which is faster compared to previous version. SPADIC v1.0 can be connected to a universal Read-Out Controller (ROC) and data processing board, which is an interface electronics between SPADIC v1.0 and DAQ. The amplifier instability, serializer glitch, comparator bug that caused problems when using negative thresholds and the CBMnet core are modified in a newer version (SPADIC v1.1). SPADIC v2.0 has 32 channels per chip and a sampling rate of 16 MHz (compared to v1.0 and v1.1 with a sampling rate of 25 MHz) and a signal shaping time of 250 ns. It can be connected to the readout board (GBTx<sup>1</sup>) via E-Link (a STS-XYTER protocol) instead of CBMnet, which is planned for a final readout chain for the TRD at SIS100. It is assumed that SPADIC v2.1 provides all features required for the TRD at SIS100.

Several detector prototypes with different readout chain were tested in the laboratory and the test-beam campaigns during 2013 - 2015 and the detector characteristics and the features of the electronics and the readouts were assessed. The detector prototypes were studied, and the issues with electronics and readouts scrutinized and the data accumulated from the beam tests analyzed and summarized in this work.

---

<sup>1</sup>An interface readout electronics between FEB and DAQ

# Zusammenfassung

Das Standardmodell der Elementarteilchenphysik befasst sich mit dem fundamentalen Aufbau der Materie. Es basiert auf der Annahme, dass das gesamte Universum aus ein paar wenigen grundlegenden Bausteinen, den Quarks und Leptonen, aufgebaut ist. Diese Teilchen werden von fundamentalen Kräften bestimmt. Diese Kräfte sind die elektromagnetische, starke und schwache Kraft<sup>2</sup>. Die starke Kraft ist der Grund für die Bindung der Bestandteile eines Kernes, die Generierung komplexer Materiestrukturen und Phasen auf subatomarer Ebene. Die grundlegende Theorie der starken Wechselwirkung, die Quantenchromodynamik (QCD), beschreibt die Interaktion zwischen Quarks und Gluonen, welche wiederum bei normaler Grundzustandsdichte gebunden in sogenannten Hadronen, wie Protonen, Neutronen und Pionen, vorliegen. Bei hohen Temperaturen und/oder Dichten der nuklearen Materie ist von QCD Rechnungen ein Phasenübergang der gebundenen, hadronischen Materie in den Zustand des Quark-Gluon Plasmas (QGP), in dem die Quarks und Gluonen frei und nicht gebunden vorliegen, vorhergesagt<sup>3</sup>. Die verschiedenen Phasen hadronischer Materie werden in einem Phasendiagramm meist als Funktion des baryochemischen Potentials  $\mu_B$  und der Temperatur  $T$  zusammengefasst. Bei sehr hohen Temperaturen und  $\mu_B = 0$  wird der Zustand des frühen Universums erreicht. Bei sehr niedrigen Temperaturen jedoch hohen Dichten werden Zustände erreicht die in kompakten Sternen vorliegen. Eines der Hauptziele von Schwerionenexperimenten ist die Untersuchung des QCD Phasendiagramms.

Das Compressed Baryonic Matter Experiment (CBM) wird als Teil der Facility for Antiproton and Ion Research (FAIR) am Helmholtzzentrum für Schwerionenforschung GSI den Bereich hoher Baryondichten mithilfe von hochenergetischen Kern-Kern Kollisionen untersuchen. Die physikalischen Hauptobservablen, die von dem CBM Experiment hierfür untersucht werden, sind Hadronen, Hypero-

---

<sup>2</sup>Die vierte fundamentale Kraft, die Gravitation, ist im Standardmodell nicht berücksichtigt.

<sup>3</sup>Streng genommen ist für hohe Temperaturen bei baryochemischen Potentialen  $\mu_B$  nahe null eher ein weicher, statt eines diskreten Phasenübergangs vorhergesagt.

nen mit mehrfachem Seltsamkeitsinhalt, leichte Vektormesonen ( $\omega, \rho, \phi$ ), Mesonen mit offenem Charminhalt ( $D^0, D^\pm, \Lambda_c$ ) und Charmonia ( $J/\psi, \psi'$ ).

Quarks und Gluonen, die Grundbausteine des Standardmodells der Elementarteilchenphysik, liegen unter normalen Bedingungen gebunden in hadronischer Materie vor. Beispiele für diese gebundenen Zustände sind Mesonen, bestehend aus Quark und Antiquark, und Baryonen, bestehend aus drei Quarks. Die fundamentale Theorie der starken Wechselwirkung, Quantenchromodynamik QCD, sagt einen Phasenübergang der hadronischen Materie zu einem heißen und dichten Zustand, dem Quark-Gluon Plasma QGP, vorher, wenn hadronische Materie in Schwerionenkollisionen erhitzt oder komprimiert wird.

Das CBM Experiment wird als Teil des FAIR Programms den Bereich höchster Baryonendichten im Phasendiagramm hadronischer Materie untersuchen. Ein wichtiger Subdetektor, um die physikalischen Ziele von CBM im Energiebereich des SIS100 Beschleunigers zu erfüllen, ist der Transition Radiation Detektor (TRD). Eines der Hauptziele ist die Erforschung des mittleren Massenbereiches im Dileptonenspektrum (Bereich zwischen der Masse von  $\phi$  und  $J/\psi$ ) und von Charmonium Produktion.

Die Identifizierung von Elektronen erfolgt im TRD mithilfe ihres spezifischen Energieverlustes im Gasvolumen des Detektors und zusätzlicher Detektion von Übergangsstrahlungsphotonen (Transition Radiation TR). Desweiteren liefert der TRD zusätzliche Ortsinformationen der Teilchen und verbessert somit die Spurrekonstruktion, welche mithilfe des STS und TOF Detektors durchgeführt wird und kann durch die Energieverlustinformation dazu beitragen zwischen schweren Fragmenten mit gleichem Verhältnis von Masse über Ladung zu differenzieren. Die Anforderungen an den TRD werden von der Fähigkeit Pionen zu unterdrücken und geladene Teilchen zu identifizieren, sowie der Stabilität unter hohen Raten bestimmt. Die Grundanforderung ist ein Pionenunterdrückungsfaktor von 10-20 bei einer Elektroneneffizienz von 90% ab einem Impuls von  $p > 6 \text{ GeV}/c$ . Die Interaktionsraten unter denen der TRD des CBM Experimentes am SIS100 Beschleuniger stabil operieren muss liegen bei 10 MHz. Das Gasvolumen innerhalb des Detektors muss klein genug sein, dass die geladenen Teilchen schnell genug zu den Drähten driften und dort Signale generieren (Signal sammelzeiten unter  $0,3 \mu\text{s}$  werden benötigt) und groß genug, um und signal dichte so eine bessere TR-Absorption zu bewerkstelligen. Durch die Positionierung des TRD zwischen STS und TOF hilft der Detektor bei der Spurrekonstruktion. Um die Datenrate niedrig wie möglich zu halten sollte die Granularität der Pads klein genug sein.

Der TRD wird sowohl im Elektronen-, als auch im Muon aufbau des CBM

Experimentes am SIS100 vorhanden sein. Jedoch wird seine Aufgabe im Mounmaufbau nur die Spurrekonstruktion und nicht die Teilchenidentifizierung sein.

Um die physikalischen Anforderungen an CBM zu erfüllen wurden verschiedene TRD Prototypen mit unterschiedlichen Designstrukturen am Institut für Kernphysik in Frankfurt (IKF) entwickelt. Um einen sehr schnellen Detektor zu entwickeln wurde ein Prototyp mit einer kurzen Verstärkungs- und ohne Driftregion konstruiert. Eine Skizze ist auf der linken Seite von Fig. 11.1 zu sehen. Dieser

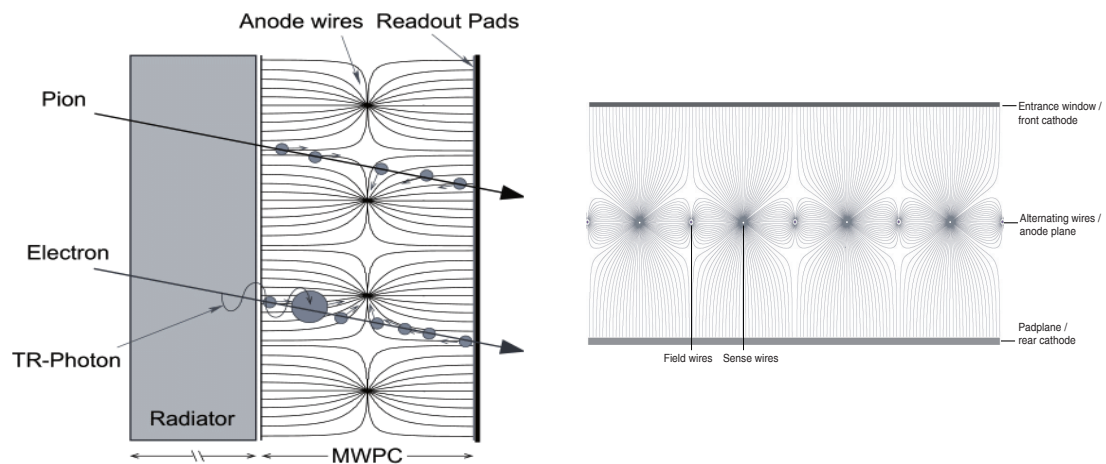


Figure 10.5: **Links:** Skizze des schnellen TRD Prototypen ohne Driftregion. **Rechts:** Aufbau des kleinen TRD Prototypen  $59 \times 59 \text{ cm}^2$ , welcher in während der Teststrahlzeit am CERN-PS im Jahr 2012 benutzt wurde. Diese Dimensionen sind für den inneren TRD am SIS100 und SIS300 vorgesehen [68]. Aufbau der alternativen Drahtgeometrie zusammen mit dem erzeugten elektrischen Feld. Signal- (Anoden) und Felddrähte (Kathoden) befinden sich alternierend in einer Reihe mit 2,5 mm Abstand voneinander, zwischen dem Eintrittsfenster (Aluminium-Mylar-Folie) und der Pad-Ebene.

Detektor war zwar schneller als ein vergleichbarer Prototyp mit Driftregion, jedoch haben Druckunterschiede zwischen der Innen- und Außenseite des Detektors zu Verformungen des Eintrittsfensters (Kathodenebene) und eventuellen Verschlechterungen des elektrischen Feldes innerhalb des Detektors, sowie einer Verzerrung der Gasverstärkung geführt. Um diese Probleme zu umgehen wurde eine alternative Drahtgeometrie entwickelt. Eine Ebene von Signal- (Anoden) und Felddrähten (Kathoden) in einer Reihe mit 2,5 mm Abstand voneinander ist zwischen das Eintrittsfenster (Aluminium-Mylar-Folie) und die Pad-Ebene platziert, siehe rechte Seite von Fig. 11.1. Diese alternierende Drahtgeometrie wurde in einem kleinen Prototypen ( $58 \times 58 \text{ cm}^2$ ) mit einer  $3,5 + 3,5 \text{ mm}$  Verstärkungsregion eingebaut. Dieser Prototyp wurde bei einer Teststrahlzeit mit einem gemischten Strahl aus Hadronen und Elektronen mit Impulsen bis zu  $6 \text{ GeV}/c$  am CERN-

PS im Jahr 2014 getestet. Es wurde eine Signal sammelzeit unter  $0,1 \mu\text{s}$  erreicht während die Gasverstärkung stabil blieb. Somit wäre dieser Aufbau ideal für den inneren Bereich der TRD Ebenen in Experimenten mit hohen Raten, z.B. am SIS300.

Ein großer Prototyp (entwickelt im Jahr 2012 am IKF) wurde verbessert und in 13 HV Kanäle segmentiert um den hohen Ladungen während der CERN-SPS Teststrahlzeit im Jahr 2015 standzuhalten. Der Strom der Anodendrahte wurde gemessen und die Stabilität des Prototypen analysiert. Der Prototyp verhielt sich stabil bei einer Hochspannung von  $HV = 1400 \text{ V}$  auf den 13 Anodenkanälen bei einer Strahlenergie von  $30,4 \text{ GeV}$  und einer Trefferrate von bis zu  $10^3 \text{ Hz/cm}^2$ . Da eine Signal sammelzeit unter  $0,3 \mu\text{s}$  für die Raten, die beim SIS100 Beschleuniger erreicht werden, ausreichend und eine ausreichende TR-Absorption erwünscht ist, ist als finales Design für den TRD am SIS100 eine  $3,5 + 3,5 \text{ mm}$  Verstärkungsregion und zusätzlicher  $5 \text{ mm}$  Driftregion mit normaler Anodendrahtebene geplant. Hierfür wurde ein großer ( $95 \times 95 \text{ cm}^2$ ) Prototyp mit dem geplanten Design entwickelt und bei einer Teststrahlzeit am CERN-SPS im Jahr 2016 getestet.

Argon und Xenon sind die optimale Wahl als Zählgas, da sie nicht elektronegativ (sie rekombinieren nicht mit Elektronen) und sehr dicht (hohe Ladungszahl  $Z$ ) sind und somit der Energieverlust der geladenen Teilchen und die TR-Absorption hoch sind. Als Löschgas wird  $\text{CO}_2$  mit einem Mischungsverhältnis von 15 - 20% hinzugemischt. Für die Detektortest im Labor und während Teststrahlzeiten wird Argon genutzt, da es kostengünstiger als Xenon ist. Für den TRD am SIS100 ist jedoch die Gasmischung  $\text{Xe/CO}_2$  (85/15) vorgesehen.

Der Aufbau der Pad-Ebene des TRDs wurde so optimiert, dass eine minimale Anzahl von sechs Modultypen in zwei Geometrien vorliegen. Drei Typen von Front-End Boards (FEB, je nach Anzahl der darauf befindlichen ASICs) und drei Typen von Read-Out Boards (ROB) sind für den TRD am SIS100 geplant.

Der erste ASIC für den TRD (SPADIC v0.3) wurde im Jahr 2010 entwickelt und in Teststrahlzeiten am CERN während 2010 - 2013, zusammen mit einem Schnittstellen FPGA Auslese Kontrolleur SUSIBO genannt, genutzt. SPADIC v0.3 hat 8 Kanäle pro Chip und kann ein Signal unit einer Zeitkonstanten  $90 \text{ ns}$  modellieren. Der Nachfolger, SPADIC v1.0 hat 32 Kanäle pro Chip und die Möglichkeit der Eliminierung der Ionenausläufer, Korrektur der Grundlinie,

Veränderung der Polarisation und Starten der Auslese durch den benachbarten Kanal. Die (Signalmod-Zeit-konstanten ellierzeit) beträgt 80 ns im SPADIC v1.0, was schneller als beim Vorgängermodell ist. Für eine Skizze der Architektur des SPADIC v1.0 siehe Fig. 11.2. Der SPADIC v1.0 kann an einen universalen Read-

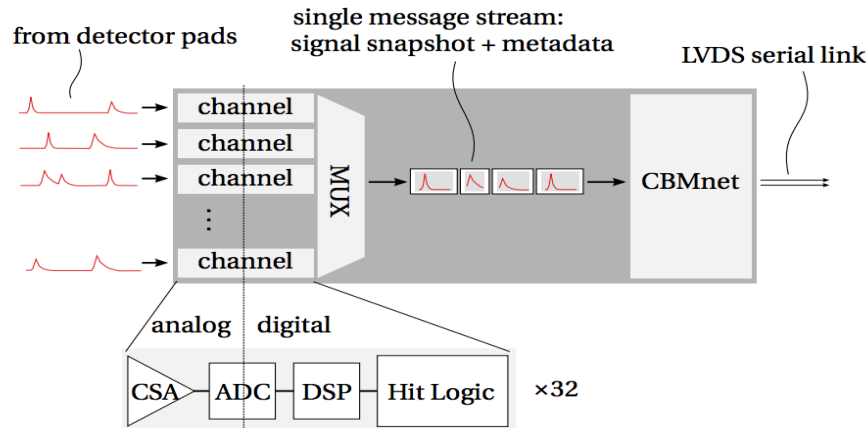


Figure 10.6: Architektur des SPADIC v1.0. Die Ladungssignale der Detektor-Pads werden vom Analogteil in jedem Kanal detektiert und vom ADC zu digitalen Pulsen konvertiert. Die digitalen Pulse werden synchronisiert und anhand ihrer Zeitstempel als Einzelnachricht mit Metadaten geordnet bevor sie über ein HDMI Kabel des CBMnets zur DAQ transferiert werden [93].

Out Controller (ROC) und ein Datenverarbeitungsboard, welches eine Schnittstellelektronik zwischen SPADIC v1.0 und der Datenerfassung (DAQ) darstellt, verbunden werden. Die Instabilität der Verstärkung, die Störung des Parallel-Serien-Wandlers, der Fehler beim Komparator, welcher zu Problemen geführt hat bei der Benutzung von negativen Schwellen und die Implementierung vom CBM-net wurden für eine neuere Version (SPADIC v1.1) modifiziert.

SPADIC v2.0 hat 32 Kanäle pro Chip und eine Aufnahmezeit von 16 MHz (im Vergleich zu der Aufnahmezeit von 25 MHz bei SPADIC v1.0 und v1.1) und eine Zeit-Konstante von 250 ns. Er kann zu Ausleseboards (GBTx) über das STS-XYTER Protokoll E-Link, statt über CBMnet, verbunden werden. Dies ist für die finale Ausleseketten für den TRD am SIS100 geplant. Die neuere Version SPADIC v2.1 wird voraussichtlich alle Anforderungen für den TRD am SIS100 erfüllen.

Verschiedene Detektorprototypen mit unterschiedlichen Ausleseketten wurden im Labor und in Teststrahlzeitkampagnen während 2013 - 2015 getestet und hierbei die Detektorcharakteristika und Eigenschaften der Elektronik und der Auslese evaluiert. Die Detektorprototypen wurden intensiv studiert und offene Fragen be-



treffend der Elektronik und Auslese genau überprüft. Desweiteren wurden die gesammelten Daten der Strahlzeiten analysiert und in dieser Arbeit zusammengefasst.

# Appendix A

## List of Acronyms

Alphabetically ordered:

**ADC** Analoge-to-Digital Converter.

**ALICE** Large Ion Collider Experiment.

**ASIC** Application Specific Integrated Circuit.

**CBM** Compressed Baryonic Matter.

**CERN** Conseil Européen pour la Recherche Nucléaire.

**CSA** Charge Sensitive Amplifier.

**DAQ** Data AcQuisition.

**DPB** Data Processing Board.

**FAIR** Facility of Antiproton and Ion Research.

**FASP** Fast Analog Signal Processor.

**FEB** Front-End Boards.

**FEE** Front-End Electronic.

**FLES** First Level Event Selector.

**FLIB** FLES Interface Board.

**FPGA** Field Programmable Gate Array.

**FWHM** Full Width Half Maximum.

**GBT** GigaBit Transceiver.

**GSI** (Gesellschaft) Helmholtzzentrum für Schwer-Ionenforschung.

**HIC for FAIR** Helmholtz International Center for FAIR.

**HGS-HIRe** Helmholtz Graduate School for Hadron and Ion Research.

**HV** High Voltage.

**LHC** Large Hadron Collider.

**LV** Low Voltage.

**MIP** Minimum Ionizing Particle.

**MUCH** MUon CHambers.

**MVD** Micro Vertex Detector.

**MWPC** Multi-Wire Proportional Chamber.

**NIST** National Institute of Standards and Technology.

**PCB** Printed Circuit Board.

**PE** PolyEthylene.

**PID** Particle IDentification.

**PP** PolyPropylene.

**PRF** Pad Response Function.

**PS** Proton Synchrotron.

**PSD** Participant Spectator Detector.

**QGP** Quark-Gluon Plasma.

**RHIC** Relativistic Heavy-Ion Collider.

**RPC** Resisitive Plate Chamber.

**RICH** Ring Imaging CHerenkov.

**ROB** Read-Out Board.

**ROC** Read-Out Chamber.

**SIS** Schwer-Ionen Synchrotron.

**SPADIC** Self-triggered Pulse Amplification and Digitization ASIC.

**SPS** Super Proton Synchrotron.

**STS** Silicon Tracking System.

**TOF** Time-Of-Flight.

**TR** Transition Radiation.

**TRD** Transition Radiation Detector.

---

# Appendix B

## Pictures and Drawings of the Prototype Construction

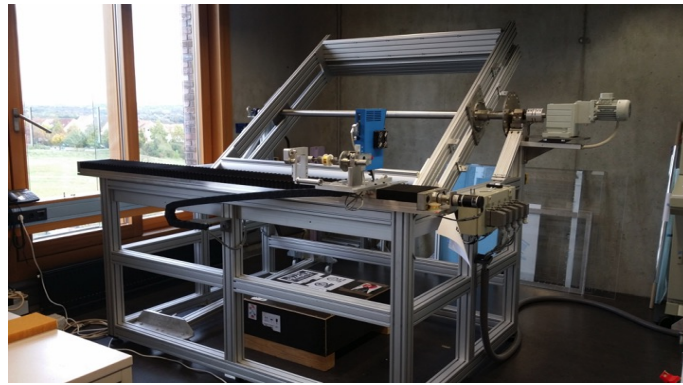


Figure 10.7: Wire winding machine with infrastructure at the IKF.

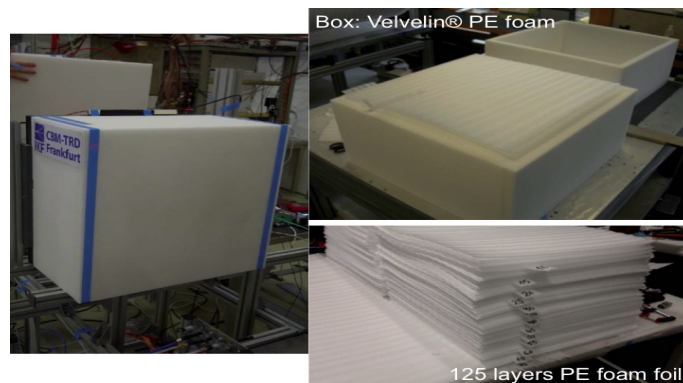


Figure 10.8: Radiators for the TRD.

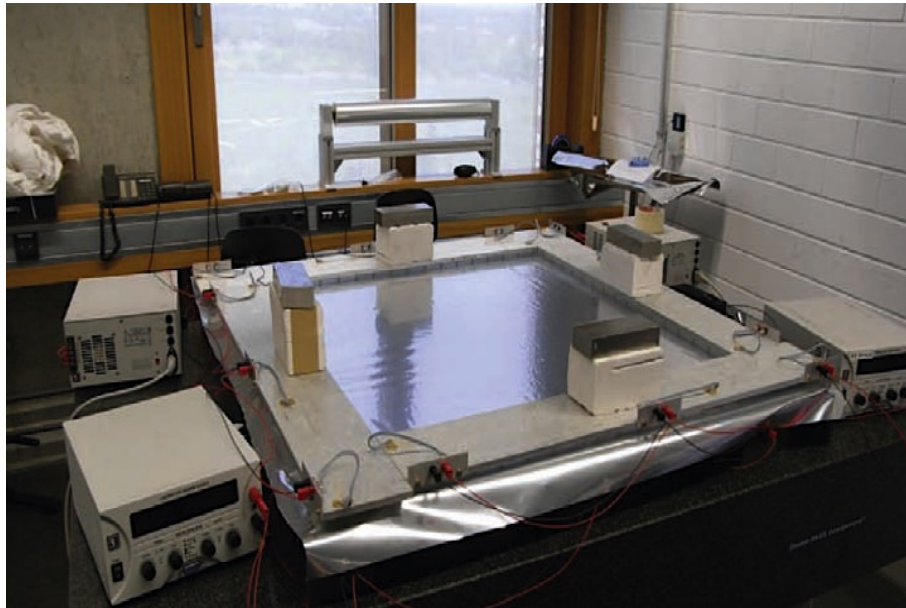


Figure 10.9: Foil stretching device at the IKF.

---

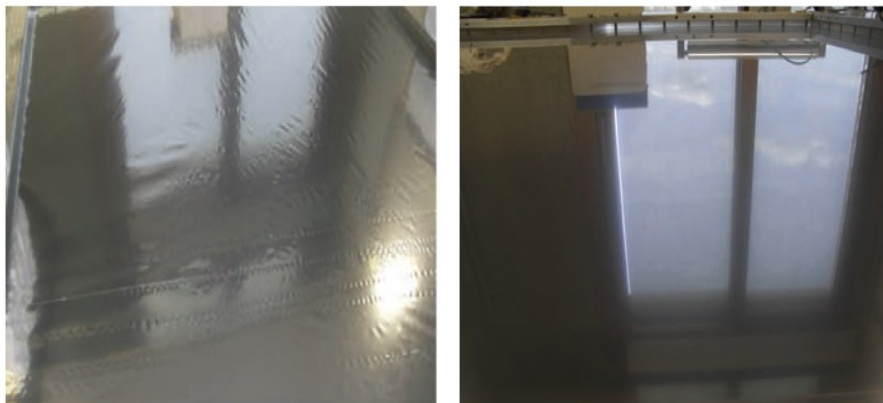


Figure 10.10: The stretch of the foil is assessed by light reflecting on it.

CBM-TRD Carbon Frame 586x580 mm

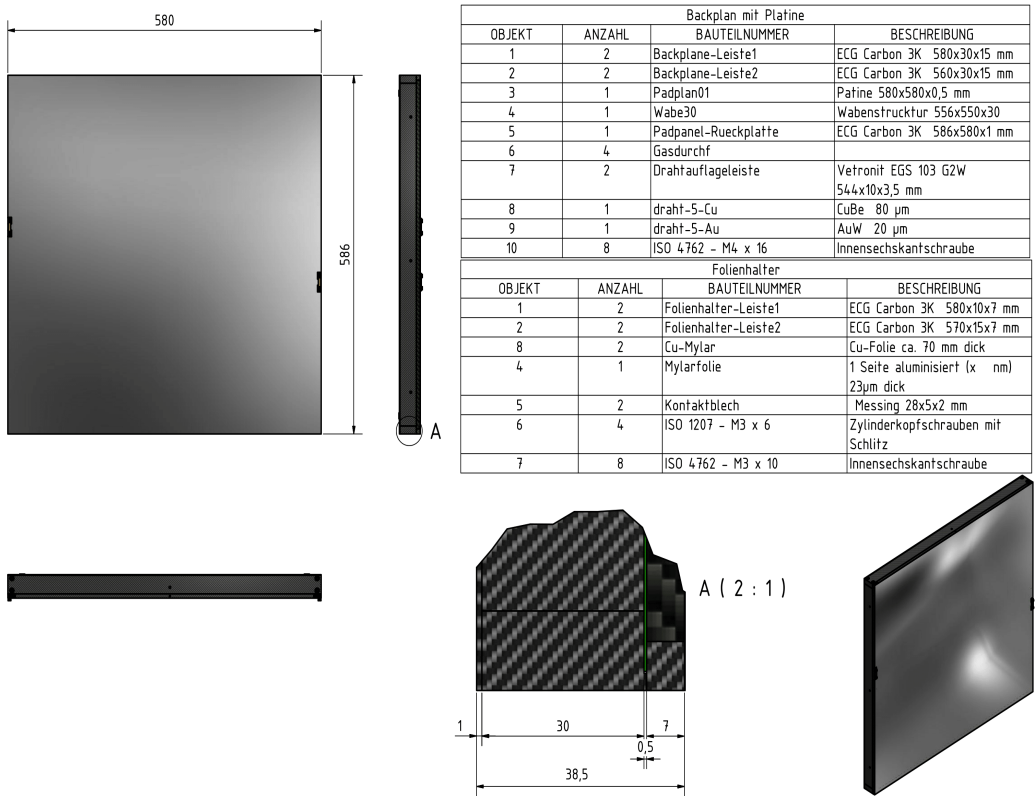


Figure 10.11: Drawing of the TRD prototype with carbon frame. The characteristics of the carbon are shown in the table.

## Cuts Through the Carbon Frame TRD

586x580x38,5 mm

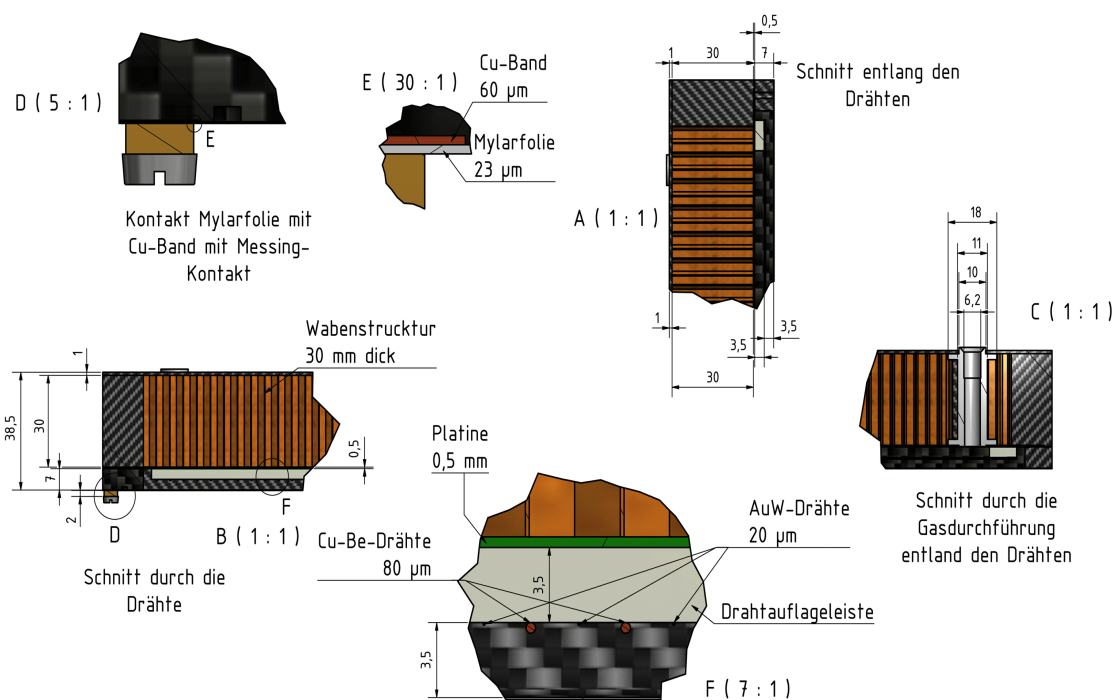


Figure 10.12: Cuts through the TRD prototype with carbon. The shown are contact of Mylar foil with Cu-band brass contact, honeycomb structure, cut alongwires and gas feed through.



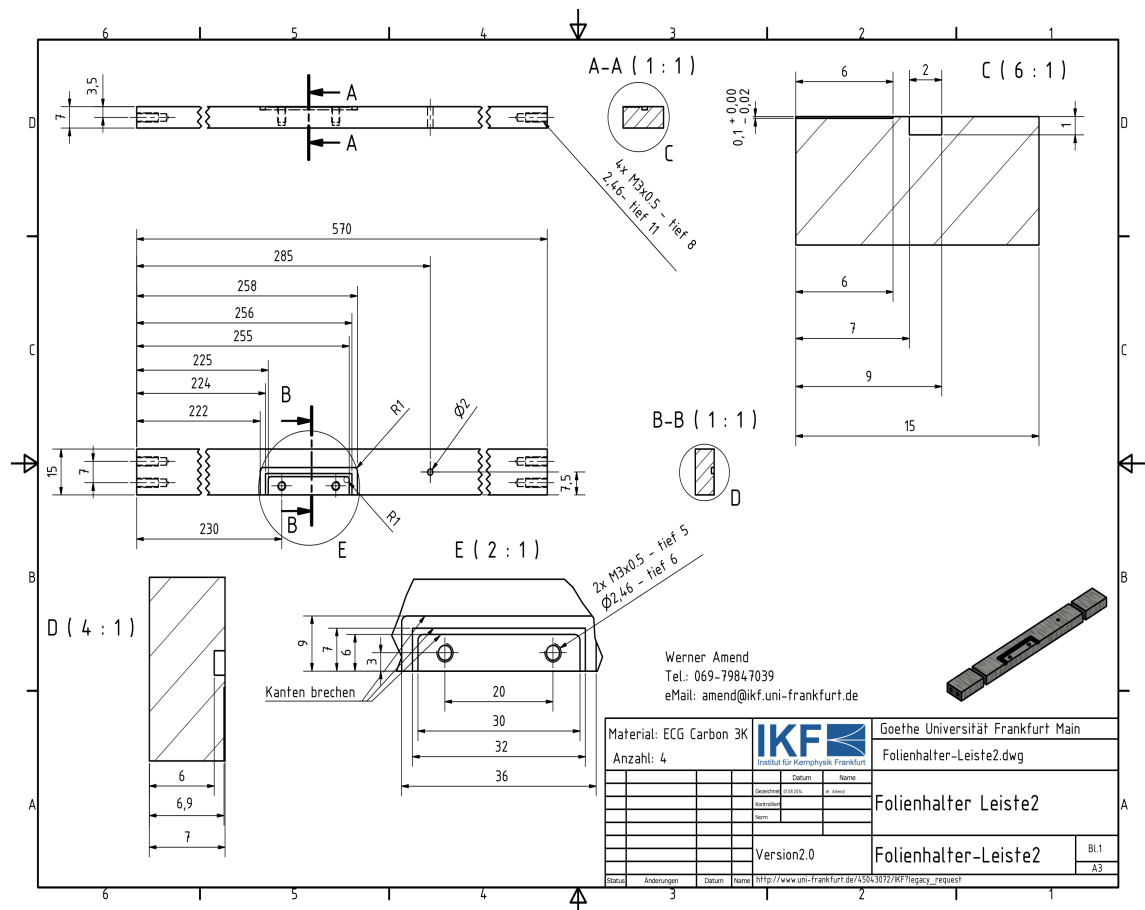


Figure 10.13: TDrawing of the foil holder of the TRD with carbon frame.

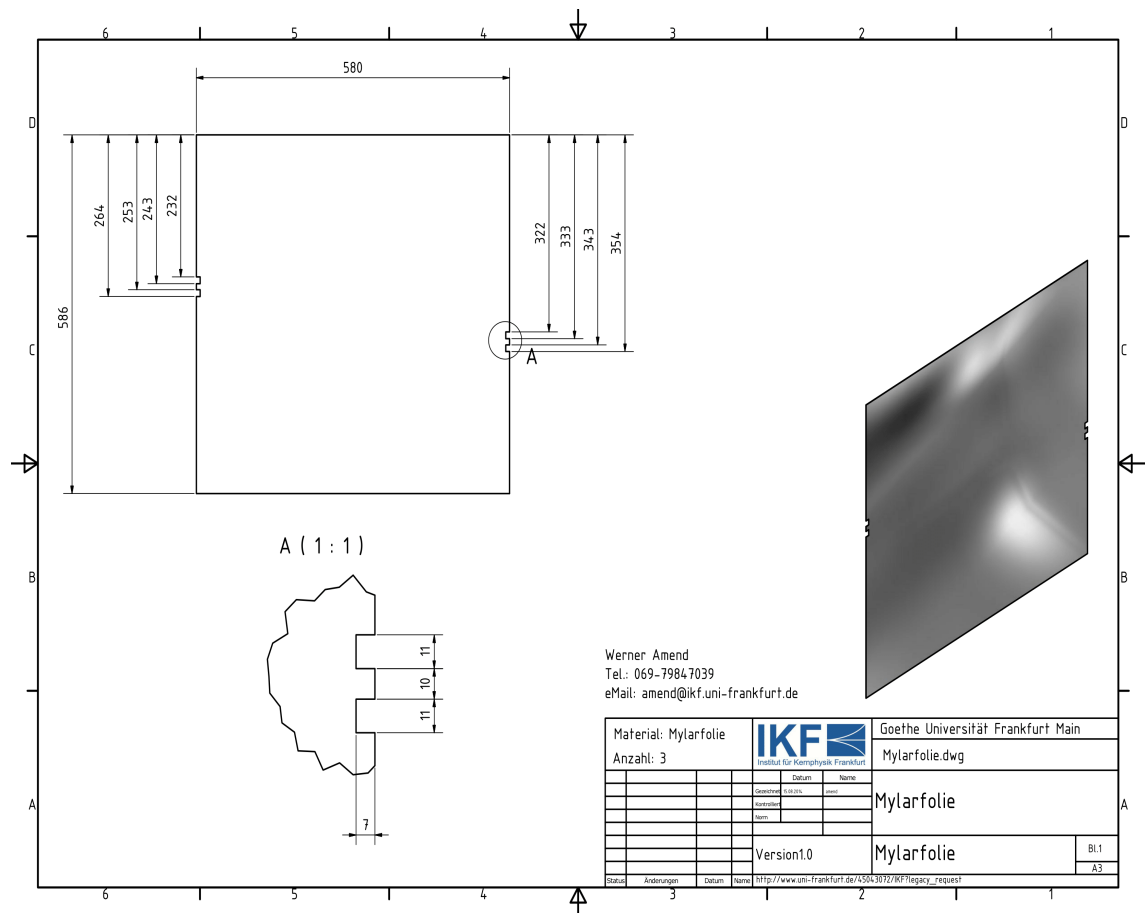


Figure 10.14: Mlar foil dimension and its connector at sides for the TRD with carbon fram.



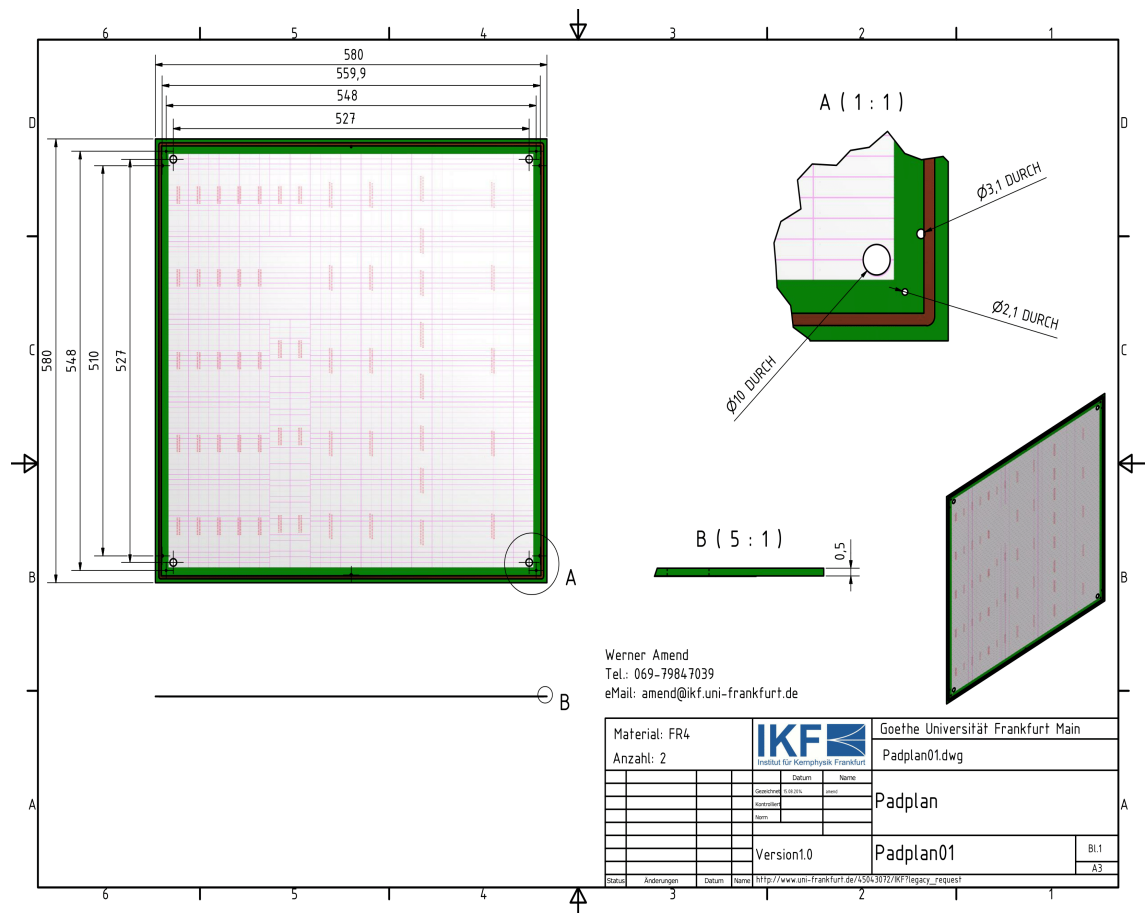


Figure 10.16: The pad plane for the TRD with carbon frame.

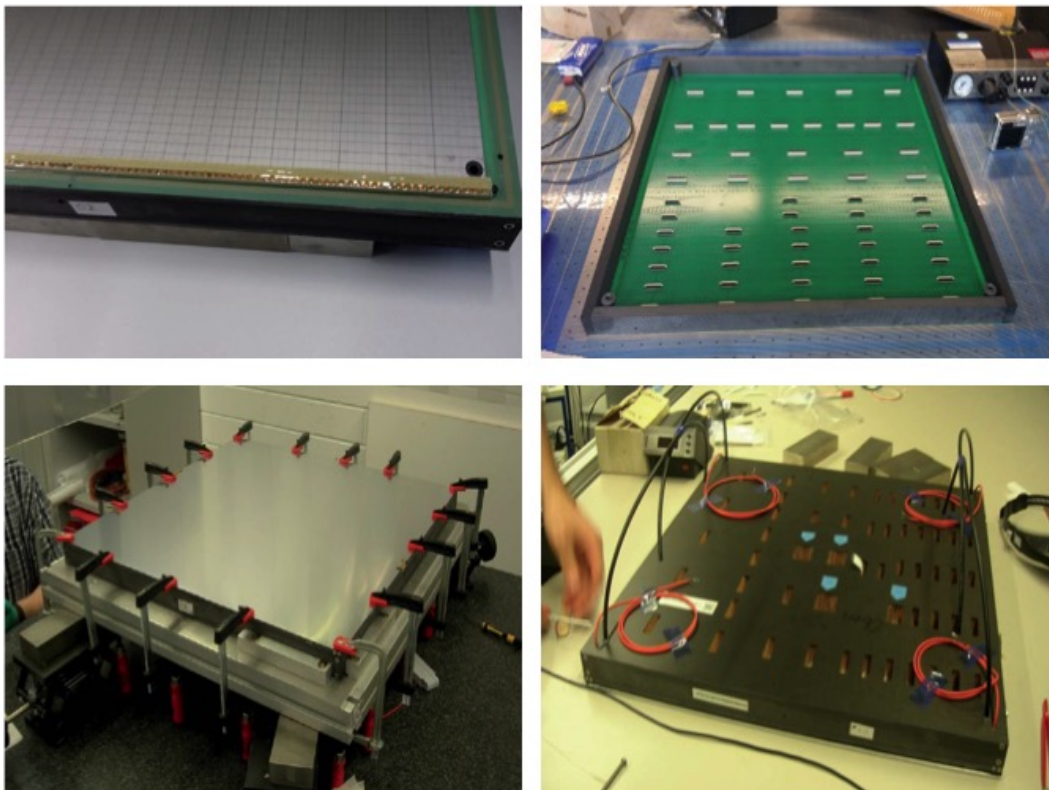


Figure 10.17: Construction of the carbon frame prototype.

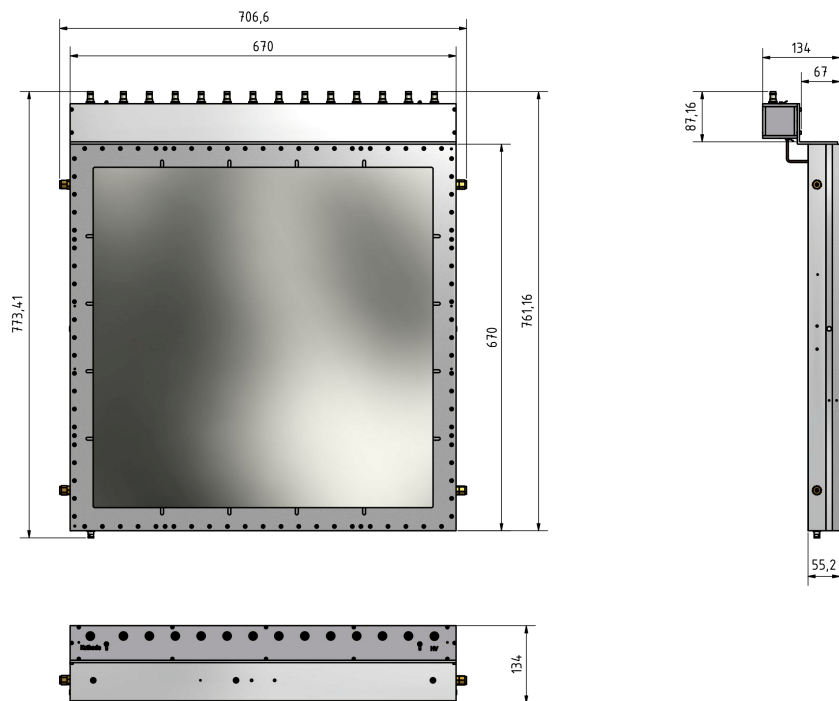


Figure 10.18: Drawing of the full size prototype with the 13 HV channels.

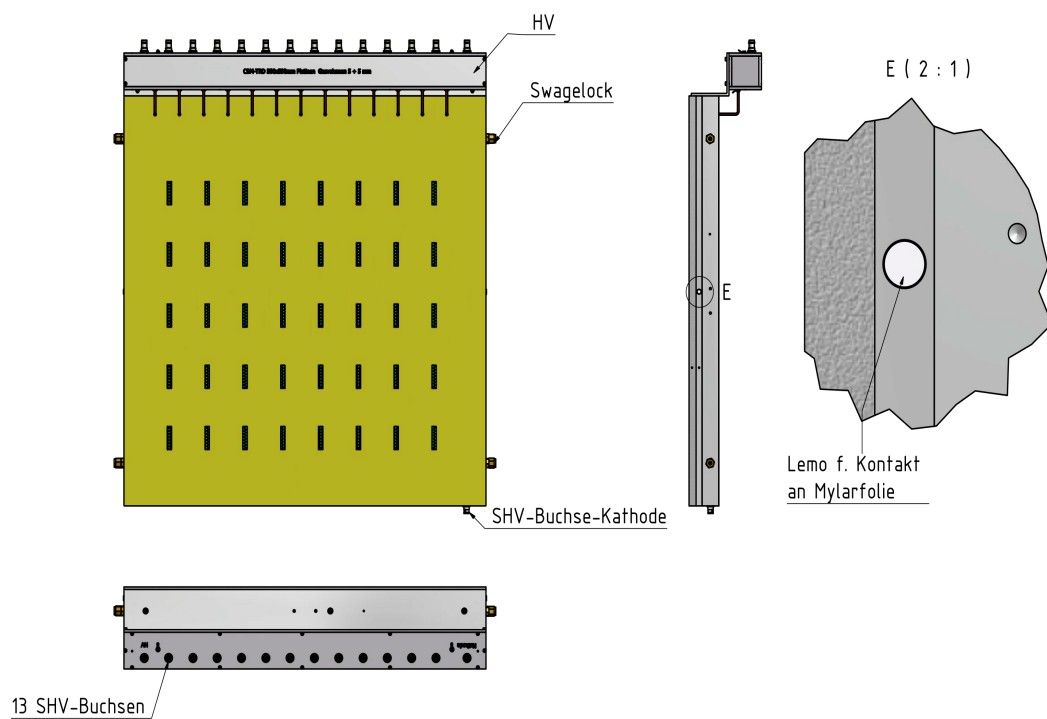


Figure 10.19: Rear, side and upper view of the full size prototype with the 13 HV channels.

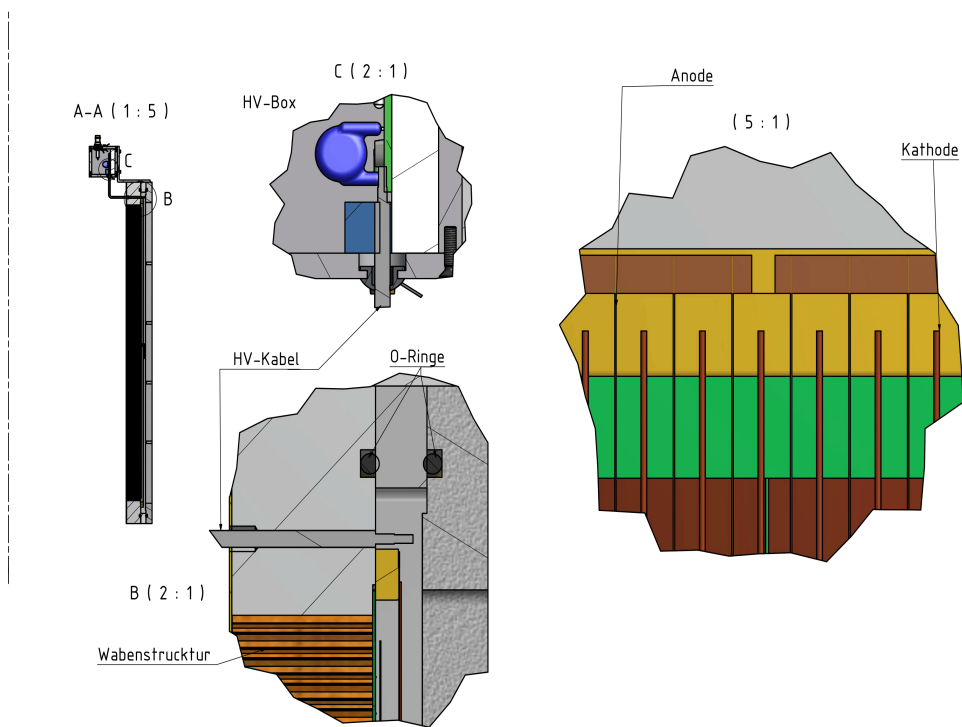


Figure 10.20: Cuts through the full size prototype with the 13 HV channels. The shown are honeycomb structure, HV box and anode-cathode wires.



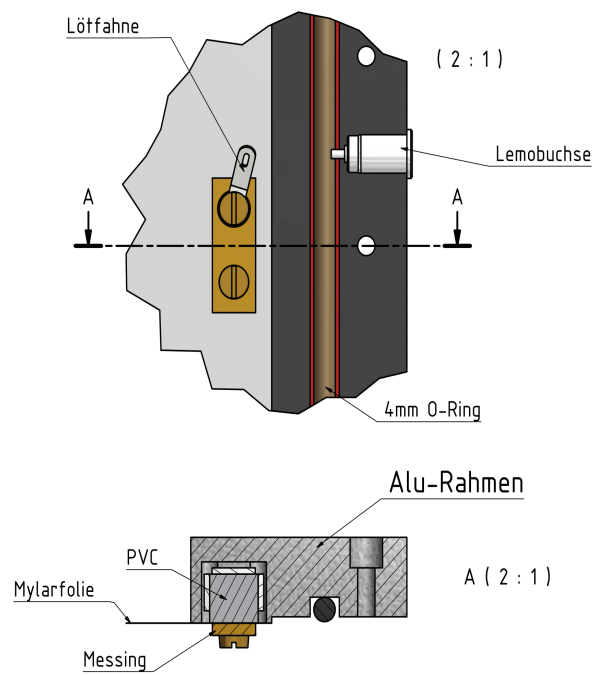


Figure 10.21: Aluminum foil (cathode plane) and its connector in the full size prototype with the 13 HV channels.

# Acknowledgement

This work could not have been done without the heartwarming helps, guidances and supervision of Prof. Dr. Christoph Blume. I really appreciate the Helmholtz Graduate School for Hadron and Ion Research (HGS-HIRE) and the Helmholtz International Center for FAIR (HIC for FAIR) for their financial and scientific supports. I am grateful to the CBM group leaders and coordinators for providing the opportunities to collaborate with experts and colleagues in different institutes. Many thanks to Prof. Dr. Markus Bleicher and Dr. Anton Andronic to be in my Ph.D committee. I acknowledge the supportive CBM-TRD groups during May 2013 to May 2017 in Frankfurt and Münster for their helps and collaborations.

# Erklärung

Ich versichere hiermit, dass ich die vorliegende Arbeit selbständig verfasst, keine anderen als die angegebenen Hilfsmittel verwendet und sämtliche Stellen, die den benutzten Werke im Wortlaut oder dem Sinne nach entnommen sind, mit Quellen- bzw. Herkunftsangaben Kenntlich gemacht habe.

Frankfurt am Main, d. 19.04.2017

Milad Tanha



# Bibliography

- [1] Johann M. Heuser, *The Compressed Baryonic Matter Experiment at FAIR: Progress with feasibility studies and detector developments*, arXiv :0907.2136 (nucl-ex).
- [2] Challenges in QCD matter physics – The Compressed Baryonic Matter at FAIR, CBM Report 2016
- [3] [https://en.wikipedia.org/wiki/Elementary\\_particle#/media/File:Standard\\_Model\\_of\\_Elementary\\_Particles.svg](https://en.wikipedia.org/wiki/Elementary_particle#/media/File:Standard_Model_of_Elementary_Particles.svg), 20.09.2016
- [4] <http://www.fair-center.eu/public/what-happens-at-fair/basic-science/physics-with-antiprotons.html>, 20.09.2016
- [5] <https://courses.lumenlearning.com/chemistryformajorsxmaster/chapter/phase-diagrams-2/>, 14.11.2016
- [6] K. Fukusihma and T. Hatsuda, Rept. Prog. Phys. 74 (2011) 014001
- [7] P. Costa, <http://compstar.uni-frankfurt.de/outreach/short-articles/the-qcd-phase-diagram-and-the-critical-end-point/>, 20.03.2017
- [8] M. Ferreira, *The QCD phase diagram in the presence of an external magnetic field: the role of the inverse magnetic catalysis*, arXiv:1509.01181 [hep-ph].
- [9] [http://www.fair-center.eu/fileadmin/fair/experiments/CBM/documents/CBM\\_flyer\\_2015.pdf](http://www.fair-center.eu/fileadmin/fair/experiments/CBM/documents/CBM_flyer_2015.pdf), 20.09.2016
- [10] The Frontiers of Nuclear Science, NSAC Long Range Plan 2007
- [11] Challenges in QCD matter physics – The Compressed Baryonic Matter at FAIR, *CBM Report 2016*.
- [12] C. Hoehne, *Development of a RICH detector for CBM: Simulations and experimental tests*, Nucl. Phys. A931 (2014) 735 - 739.

- [13] M. Bleicher, M. Nahrgang, J. Steinheimer, Pedro Bicudo, *Physics Prospects at FAIR*, arXiv:1112.5286v1 [hep-ph] 22 Dec 2011.
- [14] D. Torsten, *Dilepton spectra in  $p + p$  and  $Au + Au$  collisions at RHIC*, Stony Brook University, Diss., 2008
- [15] A. Arend, *Optimization of a Transition Radiation Detector for the Compressed Baryonic Matter Experiment*, PhD Dissertation, [https://www.uni-frankfurt.de/59344299/PhD-AArend\\_prefX3\\_Web.pdf](https://www.uni-frankfurt.de/59344299/PhD-AArend_prefX3_Web.pdf).
- [16] T. Matsui and H. Satz, *Dilepton Emission at Temperature Dependent Baryonic Quark-Gluon Plasma*, Physics Letter B, Vol. 178, 1986, doi:10.1016/0370-2693(86)91404-8.
- [17] P. Senger, *Strangeness and charm of compressed baryonic matter-the CBM experiment at FAIR*, J. Phys. G: Nucl. Part. Phys., Volume 31, No. 6
- [18] A. Prakash, P. P. Bhaduri, S. Chattopadhyay, A. Dubey, B. K. Singh, *Dimuon measurements in CBM experiment at FAIR*, arXiv:1102.0882v1 [nucl-ex] 4 Feb 2011
- [19] V. Friese, *Prospects for strangeness and charm measurements with the CBM experiment*, J. Phys. G: Nucl. Part. Phys. 37 (2010) 094025
- [20] W. Cassing, E. Bratkovskaya, A. Sibirtsev, *Strange particles and neutron stars-experiments at GSI*, Nucl. Phys. A 691 (2001) 745
- [21] <http://www.fair-center.eu/>, 09.11.2016
- [22] V. Friese, *The CBM Experiment at GSI/FAIR*, [http://www.kfki.hu/~qm2005/PROC05/Friese/Old/qm05\\_friese.pdf](http://www.kfki.hu/~qm2005/PROC05/Friese/Old/qm05_friese.pdf)
- [23] B. Friman, C. Hoehne, J. Knoll, S. Leupold, J. Randrup, R. Rapp, P. Senger, *CBM Physics Book*, Preface, Feb. 2014]
- [24] V. Friese, *The CBM Experiment – a Status Report*, DOI: 10.1134/S1063778812050079, [https://cbm-wiki.gsi.de/foswiki/pub/Homepages/VfPublication/2012\\_PhysAtomNucl75-585.pdf](https://cbm-wiki.gsi.de/foswiki/pub/Homepages/VfPublication/2012_PhysAtomNucl75-585.pdf), 05.10.2016
- [25] <http://www.fair-center.eu/for-users/experiments/cbm/introduction.html>, 05.10.2016
- [26] *Technical Design Report for the CBM-STS*, [http://www.fair-center.eu/fileadmin/fair/publications\\_exp/TDR-STS.pdf](http://www.fair-center.eu/fileadmin/fair/publications_exp/TDR-STS.pdf)

- [27] C. A. Dritsa, *Design of the Micro Vertex Detector of the CBM experiment: Development of a detector response model and feasibility studies of open charm measurement*, Doctorate Dissertation, 2011
- [28] V. Friese, *The CBM Experiment at GSI/FAIR*, [http://www.kfki.hu/~qm2005/PR0C05/Friese/Old/qm05\\_friese.pdf](http://www.kfki.hu/~qm2005/PR0C05/Friese/Old/qm05_friese.pdf)
- [29] T. Balog, *Overview of the CBM detector system*, 2014 J. Phys.: Conf. Ser. 503 012019
- [30] *Compressed Baryonic matter at FAIR: JINR participation*, Vol. 39 (2015) 1560098, P. 3, DOI: 10.1142/S2010194515600988, <http://www.worldscientific.com/doi/pdf/10.1142/S2010194515600988>
- [31] [https://indico.cern.ch/event/357738/contributions/848773/attachments/1160825/1671207/Wiebusch\\_ID137.pdf](https://indico.cern.ch/event/357738/contributions/848773/attachments/1160825/1671207/Wiebusch_ID137.pdf), 03.11.2016
- [32] <http://inspirehep.net/record/822425>, 03.11.2016
- [33] J. M. Heuser, *Status of the CBM experiment*, DOI: 10.1051/epj-conf/20159501006
- [34] P. Larionov, *Overview of the Silicon Tracking System for the CBM experiment*, 2015 J. Phys.: Conf. Ser. 599 012025
- [35] C. Dritsa, *The Ring Imaging Cherenkov detector for the CBM-Experiment*, 2013 J. Phys.: Conf. Ser. 426 012025
- [36] V. Friese, *The CBM Experiment at FAIR*, Critical Point and Onset of Deconfinement-4th International Workshop, POS (CPOD07)056
- [37] V. Friese, *The CBM Experiment at FAIR*, Critical Point and Onset of Deconfinement-4th International Workshop, POS (CPOD07)056
- [38] *The CBM time-of-flight wall*, doi:10.1016/j.nima.2010.09.165
- [39] C. S. H. Bergmann, *Development, Simulation and Test of Transition Radiation Detector Prototypes for the Compressed Baryonic Matter Experiment at the Facility for Antiproton and Ion Research*, PhD Thesis
- [40] *Online Selection of  $J/\psi \rightarrow \mu^+ \mu^-$  Decays in the CBM Experiment*, DOI:10.1051/epjconf/201610802001
- [41] B.M.K. Nefkens, J.W. Price, *The Neutral Decay Modes of the Eta-Meson*, arXiv:nucl-ex/0202008]

- [42] J. M. Heuser, *Status of the CBM experiment*, DOI: 10.1051/epj-conf/20159501006
- [43] J. D. Cuveland, V. Lindenstruth, *A First-level Event Selector for the CBM Experiment at FAIR*, 2011, J. Phys.: Conf. Ser. 331(2):022006
- [44] P. A. Loizeau, *Control Software for The CBM Readout Chain*, DPG Spring Meeting, Darmstadt, 03.2016
- [45] P. Senger, *CBM Status*, 28th CBM Collaboration Meeting, Tübingen, Germany
- [46] F. H. Attix, *Introduction to Radiological Physics and Radiation Dosimetry*, P. 124-159, ISBN-13: 978-0-471-01 146-0
- [47] <http://www.nuclear-power.net/nuclear-power/reactor-physics/interaction-radiation-matter/interaction-gamma-radiation-matter/>, 16.02.2017
- [48] <https://www.studyblue.com/notes/note/n/interactions-in-matter/deck/4770176>, 18.02.2017
- [49] F. H. Attix, *Introduction to Radiological Physics and Radiation Dosimetry*, P. 159-195, ISBN-13: 978-0-471-01 146-0
- [50] S. Braibant, et al., *Particle and Fundamental Interaction: An Introduction to Particle Physics*, P. 11–16, DOI 10.1007/978-94007-2464-8–2
- [51] B. Dolgoshein, *Transition radiation detectors*, Nuclear Instruments and Methods in Physics Research A326 (1993) P. 434-469
- [52] NIST database, <http://www.nist.gov/pml/data/xraycoef/index.cfm>.
- [53] A. Andronic, J. P. Wessels, *Transition Radiation Detector*, arXiv:1111.4188v1 [physics.ins-det] 17. Nov. 2011
- [54] R.D. Appuhn et al., Nucl. Instr. and Meth. in Phys. Res. A 270, 387 (1988).
- [55] R. Alfaro, *Construction and operation of a small multiwire proportional chamber*, 2005 J. Phys.: Conf. Ser. 18 362.
- [56] P. Dillenseger, *Charakterisierung und Signalanalyse von TRD Prototypen für das CBM Experiment*, Master Thesis, September 2013.
- [57] A. Deisting, *Readout and Analysis of the Induced Ion Signal of an InGrid Detector*, Master Thesis, Bonn Universität, 2014



- [58] [http://irfu.cea.fr/Spp/ILC-TPC/home/docs/CCAST2008/Diener\\_Ralf/06\\_PadResponse.pdf](http://irfu.cea.fr/Spp/ILC-TPC/home/docs/CCAST2008/Diener_Ralf/06_PadResponse.pdf), 07.02.2017
- [59] C. Bergmann, *Development and Test of a Transition Radiation Detector Prototype for CBM @ FAIR*, Master Thesis: [https://www.uni-muenster.de/imperia/md/content/physik\\_kp/agwessels/thesis\\_db/ag\\_wessels/bergmann\\_2009\\_diplom.pdf](https://www.uni-muenster.de/imperia/md/content/physik_kp/agwessels/thesis_db/ag_wessels/bergmann_2009_diplom.pdf).
- [60] C. Adler, et al, for the ALICE TRD collaboration, *Position Reconstruction in Drift Chambers operated with Xe, CO<sub>2</sub> (15%)*, arXiv:physics/0511233
- [61] M. G. Tarzila, *Towards a Real Size Transition Radiation Detector Prototype for the Planned Compressed Baryonic Matter experiment*, Master Thesis, 2013.
- [62] E. Mathieson, *Cathode Charge Distributions in Multiwire Chambers*, Nuclear Instruments and Methods in Physics Research A270, P. 602–603, 1988.
- [63] M. Klein-Bösing et al, *Position resolution of a high efficiency transition radiation detector for high counting rate environments*, N. In. Meth. Phys. Res. A 585 (2008) 83-87
- [64] Y. Pachmayer, *Particle Identification with the ALICE Transition Radiation Detector*, arXiv:1402.3508 [physics.ins-det].
- [65] J. Ritman, [http://www.ep1.rub.de/lehre/veranstaltungen/ws1011/dettech/skript\\_det/detector\\_ws1011\\_5.pdf](http://www.ep1.rub.de/lehre/veranstaltungen/ws1011/dettech/skript_det/detector_ws1011_5.pdf), 06.02.2017
- [66] C. Lippmann for the ALICE collaboration, *The ALICE Transition Radiation Detector*, SNIC Symposium, Stanford, California – 3 - 6 April 2006.
- [67] S. N. Ahmed, *Physics and Engineering of Radiation Detection* 2nd Edition, P. 199-201, ISBN: 978-0-12-801363-2
- [68] *Technical Design Report for the CBM, Transition Radiation Detector*, 20.Apr. 2016.
- [69] A. Bercuci et al., *Two-dimensional MWPC prototype for CBM-TRD*, CBM Progress Report 2014, P. 81
- [70] Garfield++ <http://garfieldpp.web.cern.ch/garfieldpp>.
- [71] M. Tanha, 24th CBM Collaboration week, Krakow, 08-12 Sep. 2014.
- [72] R. Veenhof. GARFIELD, recent developments. *Nucl. Instrum. Meth.*, A419:726-730, 1998.

- [73] E. Hellbär, *Elektrostatistische Simulationsstudien zum Übergangsstrahlungsdetektor des CBM-Experiments*. Bachelor's thesis, Goethe-Universität Frankfurt, 2013.
- [74] D. Emschermann, CBM-TRD TDR Review Meeting, GSI, Darmstadt, 15.03.2017
- [75] K. Reuß, *Studien zur Ausdehnung des Eingangsfensters des CBM-TRDs*, Bachelor's thesis, Goethe-Universität Frankfurt, 2013.
- [76] Dassault Systemes Deutschland GmbH. Abaqus edition 6.12, 2013.
- [77] D. Varga, G. Hamar, and G. Kiss. *Asymmetric multi-wire proportional chamber with reduced requirements to mechanical precision*. Nucl. Instrum. Meth., A648:163 - 167, 2011.
- [78] NIMA698, 11(2013).
- [79] S. Gläsel. *Studien zu MWPCs mit alternierender Drahtgeometrie*. Bachelor's thesis, Goethe-Universität Frankfurt, 2015.
- [80] M. Tanha, CBM Progress Report: *Construction and Test of a New CBM-TRD Prototype in Frankfurt*, 2014
- [81] M. Raabe, Bachelor Thesis
- [82] M. Tanha, CBM Progress Report: *CBM-TRD Prototype Tests in Frankfurt*, 2015.
- [83] T. Armbruster, PhD Thesis, *SPADIC - a Self-Triggered Detector Readout ASIC with Multi-Channel Amplification and Digitization*.
- [84] M. Krieger, *Status of SPADIC 1.0 commissioning*, 23rd CBM Collaboration Meeting, 2014.
- [85] M. Krieger, *SPADIC Status and Plans*, 25th CBM Collaboration Meeting, 2015.
- [86] M. Tanha, In the laboratory and beam test experiences, 2014-2015.
- [87] P. Fischer, M. Krieger, *Status of SPADIC developments*, 26th CBM Collaboration Meeting, 2016.
- [88] [http://www.wallpaperup.com/196369/computers\\_electronics\\_macro\\_chips\\_integrated\\_circuit\\_heatsinks\\_processor.html](http://www.wallpaperup.com/196369/computers_electronics_macro_chips_integrated_circuit_heatsinks_processor.html), 23.01.2017.

- [89] J. Gebelein, *CBM Progress Report 2013*, P. 83.
- [90] <http://cbm.uni-muenster.de/daq/>, 12.12.2016.
- [91] D. Hutter, *CBM Progress Report 2014*, P. 99.
- [92] D. Emscherman, 26th CBM Collaboration week, 17.09.2015.
- [93] M. Krieger, *SPADIC v. 1.0 Status*, CBM TRD Strategy Meeting, GSI, Nov. 2013.
- [94] P. Fischer, *Multi-Channel Charge Pulse Amplification, Digitization and Processing ASIC for Detector Applications*, Nuclear Science Symposium (IEEE), Anaheim, USA, October 2012.
- [95] T. Armbruster, PhD Thesis, *SPADIC - a Self-Triggered Detector Readout ASIC with Multi-Channel Amplification and Digitization*.
- [96] [http://home.web.cern.ch/sites/home.web.cern.ch/files/file/spotlight\\_students/information\\_about\\_the\\_t9\\_beam\\_line\\_and\\_experimental\\_facilities.pdf](http://home.web.cern.ch/sites/home.web.cern.ch/files/file/spotlight_students/information_about_the_t9_beam_line_and_experimental_facilities.pdf)
- [97] M. Al-Turany, D. Bertini, F. Uhlig, and I. König, CBM (Fair) Simulation and Analysis Framework. ALICE Workshop, 08. 2008
- [98] E. Bechtel, *Analyse von Daten der Teststrahlzeit am CERN-PS des CBM-TRDs*, Bachelor Thesis, 2015
- [99] C. Bergmann, *SPADIC v1.0 Analysis Meeting, 02-09.06.2015*, Indico page of CBM-TRD Meeting
- [100] P Schneider, Bachelor Thesis.
- [101] D. Spicker, 29th CBM Collaboration.
- [102] F. Roether, *Chamber Construction and Production*, CBM-TRD Technical Design Report Review, GSI, 14.Mar.2017
- [103] M. Krieger, P. Fischer, *Readout ASIC SPADIC*, CBM-TRD Technical Design Report Review, GSI, 15.Mar.2017
- [104] D. Emschermann, *Summary of TRD pad plane, front-end boards and readout chain* CBM-TRD Technical Design Report Review, GSI, 15.Mar.2017

## Curriculum Vitae

# Milad Tanha

### Address:

Im Taunusgarten 12  
61440 Oberursel (Taunus)  
Deutschland

### Contact:

mtanha@ikf.uni-frankfurt.de  
milad.tanha@cern.ch  
+49 152 2365 6724

### Interest

Nuclear Physics, High Energy Physics, Radiation Sciences, Medical Physics.

### Education

- 05.2013 - Present Ph.D. Student, (Major: Nuclear Physics), J. W. Goethe University, Frankfurt, Germany.
- 09.2010 - 03.2013 M.Sc. in Physics, (Major: Radiation Sciences), Umeå University, Umeå, Sweden.
- 09.2001 - 04.2006 B.Sc. in Applied Physics, (Major: Nuclear Physics), Azad University, Shiraz, Iran.
- 09.2000 - 06.2004 High School Diploma, (Major: Mathematics and Natural Sciences), Shiraz, Iran.

### Researches

- Prototype Developments and Performance Studies for CBM-TRD (Ph.D. Thesis).
- Eddy Current Sensor for Tissue Conductivity Measurement (Master Thesis).
- Fukushima Power Plant Calamity and Environmental Radiology.
- Radiation Therapy (Dose planning in external therapy).
- Dosimetry of Ionizing Interaction.

### Experience

- Beam-time Project at CERN-SPS<sup>4</sup>, 2015, Geneva, Switzerland.
- Beam-time Project at CERN-PS<sup>5</sup>, 2014, Geneva, Switzerland.
- 4<sup>th</sup> International FAIR<sup>6</sup> School, Grosseto, Italy.

---

<sup>4</sup>CERN-Super Proton Synchrotron.

<sup>5</sup>CERN-Proton Synchrotron.

<sup>6</sup>Facility for Anti-proton and Ion Research (in Darmstadt, Germany).

- International Workshop in Vibrational Spectroscopy, Umeå, Sweden.
- Advanced School of Ionizing Radiation and Protection of Man, Bad Honnef, Germany.
- International Workshop in Interdisciplinary Researches, Umeå, Sweden.
- Determination of Gamma Camera Quality Parameters, Umeå, Sweden.
- Quality Measurement of a Computed Tomography Scanner, Umeå, Sweden.
- Quality Control of an Image Intensifier, Umeå, Sweden.
- Dosimetry of Alpha, Beta and Gamma Absorption, Umeå, Sweden.
- Teaching Physics and Mathematics as a Tutor, Shiraz, Iran, 2006-2010.
- Group Manager and Scientific Journalist at *Physics Society of Iran (PSI)*, Shiraz, Iran, 2001-2006.

## Membership

- Helmholtz Graduate School for Hadron and Ion Research (HGS-HIRE) for FAIR.
- Helmholtz International Center for FAIR (HIC for FAIR).
- Deutsche Physikalische Gesellschaft (DPG).
- Goethe Graduate Academy (GRADE).
- GRADE Center CompuMath.

## Certified Qualifications

- Leadership and Career development; (by HGS-HIRE).
- Leading Teams in a Research Environment; (by HGS-HIRE).
- Leadership for Young Scientists; (by GRADE).
- Making an Impact as an Effective Researcher; (by HGS-HIRE).
- Detector Development; (by HGS-HIRE).
- Scientific Paper Writing: A Theoretical and Practical Introduction; (by GRADE).
- Scientific Presentation for Natural- and Life Sciences; (by GRADE).
- Refresh Your English Skills; (by GRADE).